Optical Spectroscopy at the Nanoscale

By

Xiaoping Hong

A dissertation submitted in partial satisfaction of the
requirements for the degree of
Doctor of Philosophy
in
Physics
in the
Graduate Division
of the
University of California, Berkeley

Committee in charge:
Professor Feng Wang, Chair
Professor Michael F. Crommie
Professor Naomi S. Ginsberg

Spring 2014

Abstract

Optical Spectroscopy at the Nanoscale

by

Xiaoping Hong

Doctor of Philosophy in Physics

University of California, Berkeley

Professor Feng Wang, Chair

Recent advances in material science and fabrication techniques enabled development of nanoscale applications and devices with superior performances and high degree of integration. Exotic physics also emerges at nanoscale where confinement of electrons and phonons leads to drastically different behavior from those in the bulk materials. It is therefore rewarding and interesting to investigate and understand material properties at the nanoscale. Optical spectroscopy, one of the most versatile techniques for studying material properties and light-matter interactions, can provide new insights into the nanomaterials. In this thesis, I explore advanced laser spectroscopic techniques to probe a variety of different nanoscale phenomena.

A powerful tool in nanoscience and engineering is scanning tunneling microscopy (STM). Its capability in atomic resolution imaging and spectroscopy unveiled the mystical quantum world of atoms and molecules. However identification of molecular species under investigation is one of the limiting functionalities of the STM. To address this need, we take advantage of the molecular 'fingerprints' - vibrational spectroscopy, by combining an infrared light sources with scanning tunneling microscopy. In order to map out sharp molecular resonances, an infrared continuous wave broadly tunable optical parametric oscillator was developed with mode-hop free fine tuning capabilities. We then combine this laser with STM by shooting the beam onto the STM substrate with sub-monolayer diamondoids deposition. Thermal expansion of the substrate is detected by the ultrasensitive tunneling current when infrared frequency is tuned across the molecular vibrational range. Molecular vibrational spectroscopy could be obtained by recording the thermal expansion as a function of the excitation wavelength.

Another interesting field of the nanoscience is carbon nanotube, an ideal model of one dimensional physics and applications. Due to the small light absorption with nanometer size, individual carbon nanotube is not visible under any conventional microscopy and characterization of individual nanotube becomes a focused research interest. Although electron microscopies and optical spectroscopies are developed previously to study carbon nanotubes, none of them permitted versatile imaging and spectroscopy of individual nanotube in a non-invasive, high throughput and ambient way. In this thesis a new

polarization-based optical microscopy and spectroscopy is developed with exceedingly better contrast for one dimensional nano-materials and capability of individual carbon nanotube imaging and spectroscopy. This development provides a reliable way to measure the absolute absorption cross-section of individual chirality-defined carbon nanotubes. It also enables fast profiling for growth optimization and *in situ* characterization for functioning carbon nanotube devices.

Two dimensional systems constitute another important family of nanomaterials, ranging from semi-metal (graphene), semiconductors (transition metal dichalcogenides) to insulators (h-BN). Despite of their scientific significance, they present a complete set of 2D building blocks for two dimensional electronics and optoelectronics. Heterostructures purely made of 2D thin films hold great promises due to functionality, scalability and ultrathin nature. Understanding the properties of the coupled heterolayers will be important and intriguing for these applications. With the advanced ultrafast laser spectroscopy, we study the dynamics of charge transfer process in two dimensional atomically thin semiconductors heterostructures. An extremely efficient charge transfer process is identified in atomically thin MoS_2/WS_2 system, which is expected to form a type-II heterojunction. Our discovery would greatly facilitate further studies of 2D materials as a photovoltaic device.

To My Wife Wenwen,

and My Parents Zhiying Huang & Jiasong Hong

Contents

List of Figures

Acknowledgements

I am grateful to my advisor, Prof. Feng Wang, for his continuous guidance and support over the past five years. He shaped my way of doing research with his scientific enthusiasm and rigor, and my taste of good science with his broad knowledge and insightful understanding. Especially, I enjoyed my research with his "simple" and enlightening physics pictures even for the most abstruse problems. I also appreciate his thoughtful plans for students, and in the case of me, developing physical thinking and mastering experimental techniques in the junior years and exploring interesting projects in the senior years.

I would also express my gratitude to Prof. Y. R. Shen, who is always available and glad to offer all levels of guidance from scientific understandings to career developments.

I am greatly indebted to my undergraduate advisor, Prof. Michael Loy, who patiently guided me, led me into this fascinating optics world and continuously supported me throughout my years in Ph.D. program.

I consider myself fortunate to be among the many bright and fine colleagues in the Wang group and Shen group. Dr. Kaihui Liu, a fellow postdoctoral researcher, introduced me the field of carbon nanotubes and established long-term and fruitful collaborations on that subject. I learned from him also the ways to identify interesting problems and how to finish a project with clear presentation and writing. Jonghwan Kim, a fellow graduate student whom I worked with in my senior years, is a bright and organized person. I always found myself appreciating his critical thinking, his enthusiasm and his willingness to help other people. During the days I work with him, I was constantly influenced by his "positive energy" and it made the long hours in the basement much more enjoyable. Dr. Sufei Shi, who was like a big brother to me, kept encouraging me and helped me in all possible ways. His stepwise approach to instrumentations also greatly influenced me. I would also like to thank Chenhao Jin for sharing with me his in-depth understanding of van der Waals coupled systems, Dr. David Cho for his kindness and patience to find me optical components and teach me optical techniques in my first year, Dr. Chuanshan Tian and Dr. Weitao Liu for their introduction to me the nonlinear optics, Dr. Steve Byrnes for his introduction of photovoltaics. And lastly I want to thank all the other fellow students and postdocs in Wang group and Shen group for their support; they are Dr. Tomer Drori, Dr. Yisheng Yang, Dr. Baisong Geng, Dr. Liang Sun, Dr. Jaeho Sung, Dr. Chi-Fan Chen, Jason Horng, Long Ju, Bo Zeng, Dr. Yu-Chieh Wen, Dr. Fajun Xiao, Dr. Hui Ling Han, Dr. Zhiwen Shi, Dr Yinghui Sun, Xinglai Shen and Dr. Jong Shan.

I had the pleasure to work collaboratively with different groups in Berkeley. I appreciate the timely help from Prof. Mike Crommie and his kindness to serve my committee. I also want to thank fellow graduate students in Crommie group, Ivan Pechenezhskiy and Giang Nguyen, who taught me from scratch about STM and collaborated with me fruitfully on combining infrared laser with STM. I also want to thank Prof. Ginsberg Naomi for advices and serving my committee.

In the department, I want to acknowledge all the supporting staff, especially Anne Takizawa, Donna Sakima and Anthony Vitan, for taking care of real life affairs and ensuring us a great atmosphere for study and research.

Finally I want to express my gratitude towards all the brothers and sisters in the Church for their support in the Spirit and in daily life. Their love and care had made my life in Berkeley full of peace and joy. I am deeply grateful to my wife Wenwen and my parents for their everlasting love and encouragements.

Chapter 1 – Introduction

1.1 Background and Motivation

Among all things bestowed to mankind, color is a beautiful and essential phenomenon. Although color is long perceived and used throughout human history, it is not until recent centuries people discovered color as a combination of different wavelengths. The study of color, spectroscopy, then becomes one of the greatest modern endeavors in human society to understand nature, with systematic and quantitative studies of light spectrum and its interaction with materials. From the color of the sky, the formation of rainbow to atomic transitions and molecular vibrations, spectroscopy is constantly deepening our understanding of natural phenomenon and plays a crucial role in establishing the most fundamental modern physics, including quantum mechanics, relativity and quantum electrodynamics. In recent decades the invention of laser accelerates the development of spectroscopy and broadens the spectroscopic studies with completely new capabilities such as extremely high power, narrow linewidth, strong coherence and temporal dynamics. Being so versatile, laser spectroscopy is virtually applied to all the technical fields in modern society. Material science, for example, benefited significantly from laser spectroscopic techniques ranging from electronic band structure determination to chemical gas identification (*1*).

As an emerging field in material science, nanoscience and engineering attracts focused research attention in recent years as a unique system for a unique perspective of science and brighter promise of future applications. Many techniques are developed specifically for these types of materials, including scanning tunneling microscopy (STM), nanoscale lithograph and transport and various scattering microscopy with electrons and neutrons. Although there are obvious advantages with laser spectroscopy, such as versatility, non-invasiveness and temporal capabilities, laser spectroscopy at nanoscale is limited in certain ways, such as limited resolution and weak interaction with nanomaterials. In this thesis, I present three ways of utilizing laser spectroscopy in nanoscale science.

1. Adding new capabilities to existing characterization tools, e.g. STM.

2. Enhance optical detection sensitivity by manipulation of light

3. Obtain temporal responses of nano-materials from ultrafast lasers.

1.2 Outline of Thesis

In Chapter 2-3 we focus on a development of infrared (IR) spectroscopy with an STM. An IR continuous wave (cw) optical parametric oscillator (OPO) is developed in Chapter 2 with the capability of high power single wavelength output. A large mode-hope free continuous tuning of wavelength is demonstrated for accurate measurements of ultra-sharp

molecular vibrations. We combined this laser with a STM in Chapter 3. By shooting the laser at a monolayer of molecules, the absorption of the molecule will be translated to the thermal expansion of the substrate, allowing new *in situ* vibrational spectroscopy capabilities in STM. A comparison with the existing inelastic electron tunneling spectroscopy (IETS) is made to demonstrate the resolution of this technique.

In Chapter 4, we demonstrate an ultra-sensitive optical measurement of carbon nanotubes (CNT), a typical one dimensional material. A big obstacle in the development of carbon nanotube field is lack of a high throughput imaging and characterization tool of this material. The tube growth mechanism could not be efficiently optimized due to characterization difficulties and the functioning of nanotube devices could not be improved due to lack of *in situ* evaluations. However this situation could be addressed by a novel application of the optical homodyne process, where one makes use of the coherent nature of absorption and controls the interfering beams with simply two polarizers. The once difficult-to-measure absolute absorption measurements are also becoming easily accessible. Absolute absorption cross-sections of more than 50 different chirality nanotubes are measured. With this vast information, we studied the exciton behavior as a function of chirality and established an empirical formula of absorption cross-section for any chirality.

Finally in Chapter 5, we employ the ultrafast laser spectroscopy to study the atomically thin transition-metal dichalcogenides and their heterostructures. With femtosecond laser systems, we could obtain the temporal responses from these nano-materials. Transition-metal dichalcogenides, as 2D semiconductors, are recently emerging as an indispensable member of 2D materials family. They have demonstrated strong light-matter interaction and high on-off ratio, properties promising for next generation electronics and optoelectronics. Heterostructures from these atomically thin film will combine various advantages of these materials and open up new application possibilities. Understanding the properties of the coupled heterolayers will then be important and intriguing for these applications. With femtosecond lasers, we probed the ultrafast charge transfer process in atomically thin MoS2/WS2 heterostructure, and the rate can be as fast as 50 fs. This is comparable to the best performance in organic photovoltaic devices and we hope our findings could open up new direction of using 2D semiconductors as photovoltaic materials.

Chapter 2 – Broadly Tunable Mod Hop Free Mid-Infrared Light Source for Vibrational Spectroscopy

2.1 Introduction

Infrared laser development has been an active field since the invention of laser. The most common type of mid-infrared laser (2 μm to 15 μm) is through frequency down-conversion from a visible beam. This process is a non-linear process that relys on very high optical field, a pulsed laser is usually required as the pump. In certain cases, however, low-repetition pulsed lasers are to be avoided due to thermal fluctuations, such as in the case when the laser is combined with a scanning tunneling microscope (STM). It is therefore desirable to have continuous wave (cw) or quasi-cw infrared lasers.

There are not many solutions for IR lasers with cw output. Lasing has been demonstrated with certain lead salt materials such as PbSSe and PbSnTe, with bandgap at mid-infrared (*2*). But the drawbacks of these bandgap materials are that stable lasing condition only satisfies at cryogenic temperature and it is difficult to achieve continuous tuning over a broad range. Quantum cascade laser (*3*), as being actively developed in recent years, exploits the inter sub-band transition from quantum wells and archives stable lasing at room temperature. Still its tunability is usually limited for each chip. A third type of cw infrared source is the parametric down-conversion with cw pumping. The shortcoming with this type of light generation is that the conversion efficiency is extremely low. Unlike the pulsed laser, where energy is concentrated within an extremely short period of time (easily 1 ps) with exceedingly high instantaneous electric field, cw laser has the intensity averaged out in time and orders of magnitude smaller electric field. However one could utilize a high quality resonant cavity to drastically enhance one of the generated electric field (signal or idler) and this resonating field will interact with the pump field at elevated conversion efficiency. Effectively this will reach a lasing threshold when the gain of the resonating field is larger than the loss. Optical parametric oscillator (OPO) is such an oscillator that permits cw lasing of infrared light.

There are some other constrains about the laser in terms of vibrational spectroscopy measurements with STM, as we will discuss in the next chapter. To be able to scan through the narrow resonances of the molecular vibrations (it is typically smaller than 1 cm^{-1} for gas phase)(*4*), the laser linewidth has to be much smaller than the molecular vibrations and the laser center wavelength should be tuned continuously without hopping. The power has to be reasonably large and stable that it can create enough signal to be detected by the STM. A periodically poled Lithium Niobate (PPLN) based cw OPO is an ideal candidate for all the above constraints. In my experiment, such a laser was built for STM spectroscopy measurements.

2.2 Working Principles of PPLN-based cw OPO: Quasi-Phase Matching

For an efficient difference frequency generation (DFG) from two input photons, two important conditions have to be met simultaneously. The obvious one is the energy conservation, which means the generated photon energy will be the difference between the two input photons. The second is the phase matching condition, meaning the previously generated beam needs to be in phase with newly generated beam for coherent add-up through the length of the crystal. This effectively requires the wavevector (momentum) to be conserved. Both of these conditions are summarized in Eq.2-1 and 2-2, where the two input beams are pump and signal and the generated beam is called idler.

$$\boldsymbol{\omega}_{\text{pump}} - \boldsymbol{\omega}_{\text{signal}} = \boldsymbol{\omega}_{\text{idler}} \qquad \text{Eq. 2-1}$$

$$\boldsymbol{k}_{\text{pump}} - \boldsymbol{k}_{\text{signal}} = \boldsymbol{k}_{\text{idler}} \qquad \text{Eq. 2-2}$$

Eq. 2-2 can be written as

$$\boldsymbol{n}_{\text{pump}}\boldsymbol{\omega}_{\text{pump}} - \boldsymbol{n}_{\text{signal}}\boldsymbol{\omega}_{\text{signal}} = \boldsymbol{n}_{\text{idler}}\boldsymbol{\omega}_{\text{idler}} \qquad \text{Eq. 2-3}$$

Combining Eq.2-1 and Eq. 2-3, we see that refractive index for different light frequency (dispersion curve) does play an important role in phase matching condition. For a typical dispersion curve in a transparent crystal, the refractive index increases when the light frequency increases due to strong absorptions typically present at ultraviolet range (*5*). This phenomenon imposed a great difficulty on Eq. 2-3 because $n_{\text{pump}} > n_{\text{signal}} > n_{\text{idler}}$ and $\omega_{\text{pump}} > \omega_{\text{signal}} > \omega_{\text{idler}}$. This will lead to gradual build-up of the phase difference between the previously generated beam and the newly generated beam, and once the phase reaches π, they are going to destructively interfere with each other and produce a smaller output. To circumvent this situation, optical birefringence of anisotropic materials is typically used and make one or two beams polarized at the extraordinary axis to use the extraordinary refractive index, usually larger than the ordinary refractive index (*6*). However due to the sensitivity of the refractive index with respect to polarization direction and temperature, the phase matching condition is only met at critical angles and complicates the alignment and tuning procedure. As a compromise, a short crystal is usually used to ease the phase matching, while the length of the crystal becomes the limiting factor of the conversion efficiency. Additionally, the highest nonlinearity of the crystal might not be exploited because the angle might not favor phase matching.

Quasi-phase matching provides a clever solution without crystal rotation (*7*). The main concept is to provide an additional wavevector by “poling” the crystal in a periodic way. Lithium Niobate, as a typical ferroelectric non-linear crystal, can be electrically poled along the maximum nonlinear coefficient direction (*8*).

As shown in Figure 2-1a, there exist a bistability of the ferroelectric Lithium Niobate crystal. The relative displacement between the negative ions and positive ions could possess two stable configurations and allows coexisting of stable opposite permanent electric dipole (arrow in Figure 2-1a). As a result, the polarity of Lithium Niobate can be switched when an electric field of 21kV/mm or higher is applied for more than 50ms. This polarity change effectively reverses the polarizability. (Shown in Figure 2-1b)

Periodically Poled Lithium Niobate (PPLN) provides an ideal way for quasi-phase matching. The period of the PPLN, from the wave point of view, provides an additional wavevector for phase matching with poling period $\Lambda = \frac{2\pi}{\Delta k}$, where

$$\Delta \boldsymbol{k} = \boldsymbol{k}_{\text{pump}} - \boldsymbol{k}_{\text{signal}} - \boldsymbol{k}_{\text{idler}} \qquad \text{Eq. 2-4}$$

This additional momentum from crystal could be tuned to exactly make up the momentum difference. One can intuitively think this procedure as effectively reversing the phase difference by π when the accumulated phase mismatch reaches π, and thereby convert destructive interference into constructive interference. The conversion efficiency is therefore no longer limited by crystal length. The maximum nonlinear coefficient for this crystal (d_{33} = 27 pm/V) is used in PPLN and the three beams will have the same polarization along the extraordinary direction (*8*).

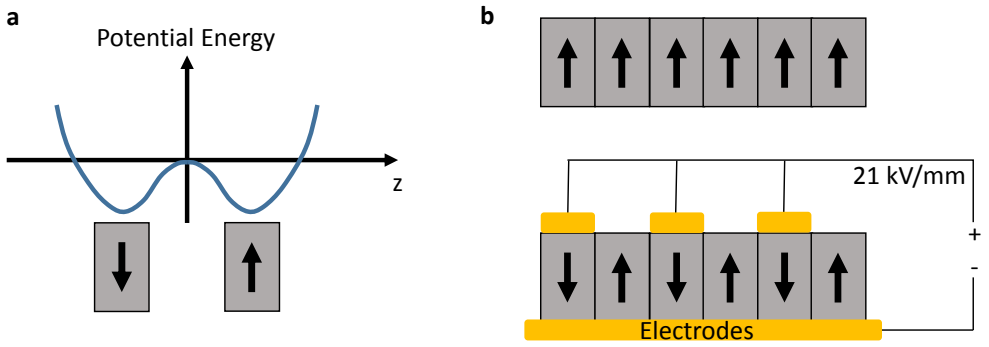

Figure 2-1 Fabrication of periodically poled Lithium Niobate. a. bistability of Lithium Niobate ferroelectric configuration. The permanent electric dipole (arrow) could possess two stable configurations. Vertical axis z is the relative distance between the negative and positive ions. **b.** Illustration of permanent dipole flipping by applying high voltage across the crystal. Periodic poling of Lithium Niobate is achieve with periodic array of electrodes.

This quasi phase matching condition can be satisfied for a broad range of wavelengths. The poling period could be varied systematically to allow quasi-phase matching at significantly different wavelength ranges. Temperature change could also lead to finite refractive index change for all three interacting wavelengths and a precise control

of temperate could produce a desired detune of wavelength. The final output of the wavelength could in principle cover the infrared transmission band of the crystal.

In practice, Lithium Niobate crystals for OPO applications are usually doped with MgO (<5%) because it has significantly higher damage threshold and the change in extraordinary refractive index is minimal due to doping (*9*).

2.3 OPO Construction

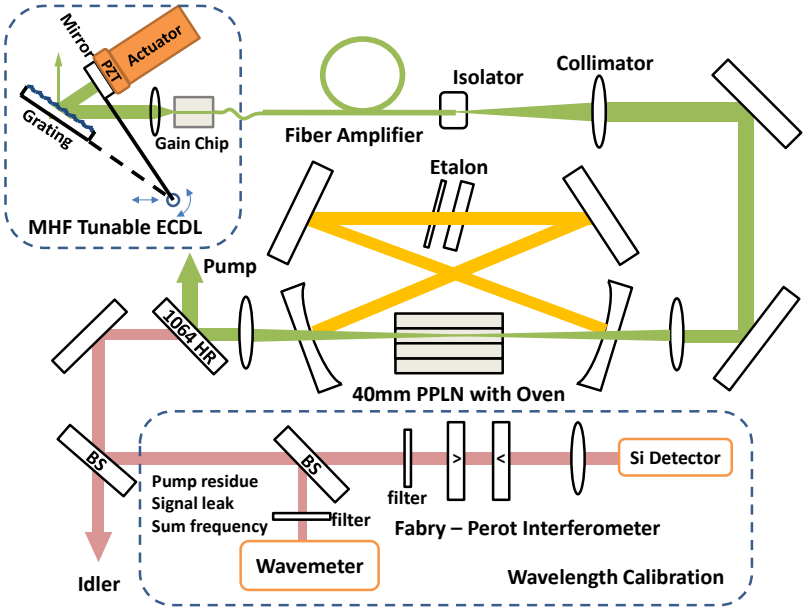

Figure 2-2 Experimental alignment of the PPLN-based OPO. The upper-left box is a 1064 nm external laser diode. It can be mode-hop-free tuned by carefully aligning the pivot position of the external mirror. This output is amplified by a fiber amplifier to up to 10 W and deliver into the cavity. The cavity features high reflection and low loss for the signal beam (orange) and allows it to oscillate with extremely high power (on the order of kW). Idler is converted from nonlinear interaction from pump and signal with high efficiency. The lower-right box is a wavelength characterization setup. BS stands for beam sampler.

With this 5% MgO-doped PPLN crystal, we attempt to construct an optical parametric oscillator that could efficiently convert an input pump wavelength (~1064 nm) into infrared wavelengths. In principle the output at arbitrary wavelength can be designed, as long as the final output is in the transmission range of the crystal. We choose to target the C-H stretching bonds around 3.3 μm (idler) with the signal beam oscillating at around 1500 nm. Figure 2-2 shows the setup of the laser. A commercial diode laser centered on 1064nm is used as a seed laser. It can be tuned mode-hop-freely by choosing carefully the pivot position of the external mirror, as we will explain in the next session. The single frequency light from the seed laser couples into to a commercial polarization-maintaining fiber amplifier, which outputs up to 10 W amplified light to pump the OPO. A ring cavity is configured with two planer mirror and two curved mirror and the optimal oscillator

geometry is calculated with SNLO software(*10*). The radii of curvature of the curved mirrors are 20 cm. The curved mirrors are separated by 28 cm and the flat mirrors by 26.2 cm. The incident angle of the flat mirrors is about 7 degree. A 4 cm 5% MgO-doped PPLN (MgO:PPLN) is placed at the focal position between the two curved mirrors. Along the transverse direction of the crystal, there are nine gratings with periods from 27.91 to 31.59 μm in the PPLN for different quasi phase matching conditions. The transmission of the specially-coated cavity mirrors for pump (1060 nm - 1070 nm) and idler (2300 nm - 4300 nm) will be more than 90% to optimize conversion efficiency and ensure single resonance operation. The inner-side surfaces of the mirrors has highly reflective coatings (more than 99.9%) for signal wavelength (1400nm- 1900nm) so that the signal loss can be smaller for a lower lasing threshold. The oscillating signal constantly gains energy from the pump, and hence the idler wavelength is generated continuously from pump during lasing. Two etalons was later inserted into the cavity in the tuning calibration to make sure of the single frequency operation of the signal.

Lasing requires the signal gain to be larger or equal than the signal loss. The loss in the OPO comes from imperfect reflection at all four mirrors, crystal surfaces and imperfect etalons. We estimated that our cavity has roughly ~2% loss without etalon. Therefore gain in the system should be equal or larger than 2%. In fact, gain in an ideal OPO system has been well modelled with nonlinear optics. A simple plane-wave approximation gives signal gain approximately (*6*)

$$\boldsymbol{G}_{\mathrm{s}} = \frac{\boldsymbol{8\pi^2 d_{\mathrm{eff}}^2 P_{\mathrm{p}} L^2}}{\boldsymbol{n_{\mathrm{s}} n_{\mathrm{i}} n_{\mathrm{p}} \epsilon_0 \lambda_i \lambda_s \mathrm{c}}} \boldsymbol{sinc^2}\left(\frac{\mathbf{1}}{\mathbf{2}}\boldsymbol{\Delta kL}\right) \qquad \text{Eq. 2-5}$$

where λ_i, λ_s, n_{s}, n_{i}, n_{p} and c are idler wavelength, signal wavelength, signal refractive index, idler refractive index, pump refractive index and vacuum speed of light respectively, d_{eff} is the effective nonlinear coefficient (the first Fourier component of the crystal nonlinear coefficient with respect to poling period), P_{p} is pump power and L is the crystal length. The phase factor $sinc^2(\frac{1}{2}\Delta kL) = \sin^2(\frac{1}{2}\Delta kL)/(\frac{1}{2}\Delta kL)^2$ accounts for phase mismatch ($\Delta k = k_{\mathrm{pump}} - k_{\mathrm{signal}} - k_{\mathrm{idler}} - k_{\mathrm{period}}$) and in the perfect quasi-phase matching case this term is unity.

This equation provides an intuitive guide to the optimization of the gain. As a second order nonlinear process, the parametric down conversion has signal gain proportional to the pump power. More important factors are the crystal length and the nonlinear coefficient, and they increase the power gain quadratically. This is due to the fact that electric field increases linearly along the crystal length and this electric field gain will be squared to obtain the power gain, as we defined in Eq. 2-5. The phase matching is also an important factor to consider because the gain efficiency falls down with sinc-square behavior.

This plane wave model turns out to overestimate the gain. We need a more realistic theory to accurately model a focused beam. A generalized gain is obtained for a focused Gaussian beam (*11*),

$$G_s = \frac{64\pi^2 d_{eff}^2 P_p L}{n_s n_i \epsilon_0 \lambda_i \lambda_s \lambda_p c} \frac{h_{sm}(K, \xi_s, \xi_p)}{1+K} sinc^2\left(\frac{1}{2}\Delta kL\right) \quad \text{Eq. 2-6}$$

where $K = k_p/k_s$, the ratio between pump wavevector and signal wavevector. $h_{sm}(K, \xi_s, \xi_p)$ is a function of K, ξ_s, ξ_p as derived in Ref. (*11*), where ξ is the focusing parameter defined as the ratio between the crystal length and the confocal parameter. With a 2% loss and calculated h_{sm} ~ 0.283, defined by input beam divergence and cavity configuration, the theoretical threshold is estimated to be ~ 2.5 W.

We achieved a threshold of about 3.5 W with this experimental configuration without etalons. The threshold increases to ~ 6.2W when additional losses are present, as in the case when we put two etalons in the oscillator to tightly lock the signal frequency. With 10 W pump and two etalons, the pump depletion could reach about 30% with the idler output power at ~0.9 W, as shown in Figure 2-3.

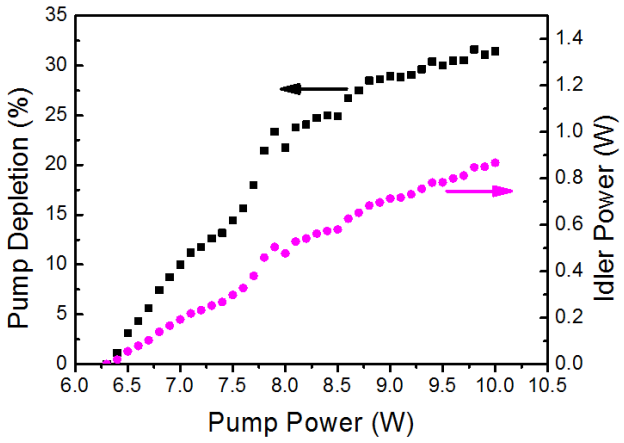

Figure 2-3 Pump depletion and idler power as a function of the pump power.

2.4 OPO Tuning

One of the most attractive attributes of an OPO is convenient tunability of the output wavelength. The tuning in PPLN OPO can be classified in two types: broad tuning (from 1.5 μm to 4.5 μm) and fine continuous tuning without mode hops (within a few nanometer).

2.4.1 Broad Tuning

The OPO becomes very versatile with a broad tunability in the mid-infrared range. For molecular spectroscopy, it enables mapping of all possible vibrational peaks from different functional groups and helps identify a large composition of molecules. From Eq. 2-3 and 2-4, we see that the wavelength combination is defined by the crystal period and the refractive indices of all three beams. Therefore we have two ways to tune the wavelength of the output: change the crystal period and change the refractive indices by temperature control.

1. Grating tuning. As shown in Figure 2-4 our PPLN crystal has a set of gratings with different periods associated with different quasi-phase matching conditions. By moving each period to the laser beam alignment, distinct difference frequency combinations are generated by a fixed pump wavelength.

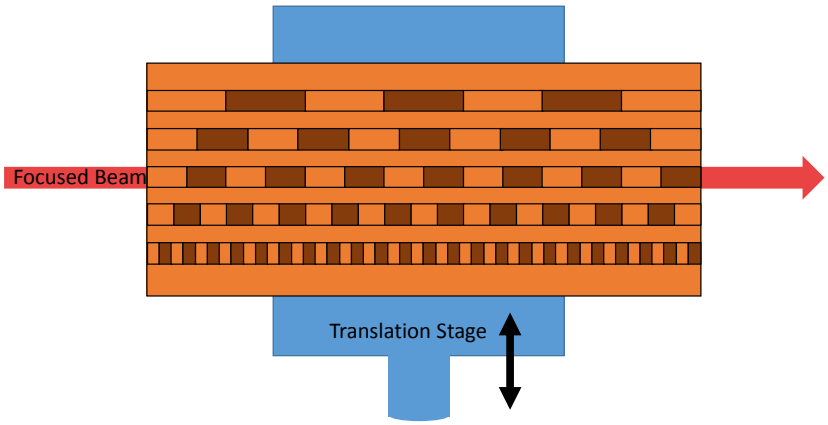

Figure 2-4 Illustration of grating tuning. The translation stage could shift different poling period to laser path way and contribute different quasi-phase matching conditions for various sets of difference frequency generation.

2. Temperature tuning. The crystal refractive indices for pump, signal and idler are all depending on temperature. Therefore when temperature changes, the refractive indices change leads to different wavelength combination to satisfy Eq. 2-4. To quantify how much wavelength tuning temperature change would introduce at fixed pump wavelength, we have to know the exact relation between refractive indices and temperature. This relation is described by Sellmeier equations, previously established for 5% MgO doped Lithium Niobate as used in our OPO (*12*).

The detailed tuning of wavelength as a function of grating period and temperature can be obtained from calculations with all known parameters. The two tuning mechanism combined predict a continuous range of spectrum from 1400 nm to 4500 nm.

2.4.2 Mode-hop free (MHF) Operations

Except for broad tunability, continuous fine tuning is indispensable in many sensing and communication applications. However mode hopping during tuning is always present

if the cavity and tuning mechanism is not carefully designed. MHF tuning, therefore, is been actively pursued in the development of laser technologies.

Pump tuning is the most convenient way to achieve mode-hop free tuning in a singly resonant OPO. The signal is always oscillating at the cavity mode with the highest gain. By additional etalons and temperature optimization, we can force the signal oscillating at one particular cavity mode when the pump is tuned. The change of the pump wavelength will be strictly translated to the idler wavelength. Therefore a well-designed MHF tuning pump will deliver a MHF tuned idler output.

A large MHF range pump laser would produce a larger MHF idler tuning range. For this purpose, we use a MHF tunable external cavity diode laser seeded into a fiber amplifier. The MHF tuning range of the diode laser should be optimized. To achieve MHF tuning in an external cavity diode laser, a Littman configuration was used (top dashed box in Figure 2-2). Wavelength is tuned by rotating the mirror around the pivot point using a piezoelectric actuator and a DC servo motor combined in series. There is a critical position of the pivot that permits the single cavity mode operation. Basically this optimized pivot position ensures that the cavity length increases accordingly with the wavelength increase to accommodate the additional distance from the existing mode, and the total number of modes are exactly the same (*13*). By fine tuning of this pivot position, we were able to obtain roughly 3 nm MHF regions from pump tuning.

Although the pump could perform MHF tuning relatively easy, achieving long range MHF tuning in OPO output is not straightforward. There are unavoidable mode hops in the oscillating signal due to mismatched phases during wavelength tuning. To tackle the phase mismatch problem, a quasi-noncritical phase matching condition was previously explored (*14*). Mathematically this condition writes as $\left.\frac{\partial \Delta k}{\partial \lambda_p}\right|_{\Delta k=0,\lambda_s} \simeq 0$, and intuitively it means the quasi-phase matching condition does not change significantly in a finite pump wavelength range with a fixed signal mode. This region was identified around pump wavelength 1066 nm with a width of about 5 nm for a fixed signal wavelength. With this configuration, a MHF range of 17 cm^{-1} was demonstrated previously (*14*). The drawback of this technique, however, is that for a fixed signal wavelength there will be only one finite range for MHF tuning and does not work at arbitrary wavelength. In order to position the MHF tuning range at any spectral position, as required by most infrared spectroscopy applications, a general tuning mechanism needs to be developed to deliver a broader MHF tuning range at arbitrary wavelength.

We realize that the quasi-phase matching condition can be continuously met if we tune the crystal temperature synchronously with the pump wavelength (*15*). An experimental quasi-phase matching temperature and pump wavelength relation was established at fixed signal at 1535.44 nm as shown in Figure 2-5. Theoretically this relation can also be calculated with known grating period and refractive indices. The best agreement between theoretical calculation and experimental measurements is found with PPLN period of 30.05 μm instead of the room temperature period 29.98 μm. This slight discrepancy could arise from thermal expansion of the PPLN crystal and inaccuracy of temperature measurements. With this calculated curve (Figure 2-5), we can optimize the

crystal temperature alongside with the pump wavelength tuning to achieve a constant quasi-phase matching.

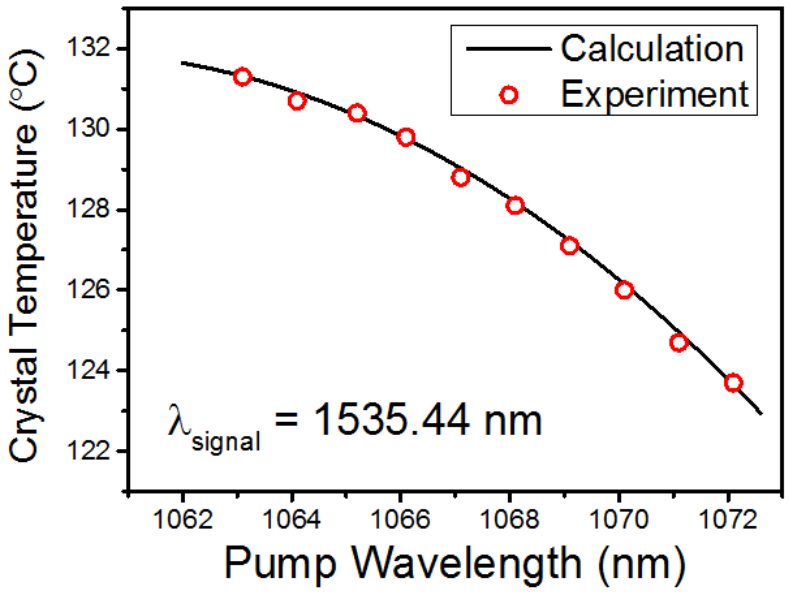

Figure 2-5 Experimental and calculated optimized crystal temperatures for continuous phase matching condition during pump tuning with fixed signal wavelength 1535.44 nm.

2.5 Characterization of the Home-built OPO

Because the oscillating signal is intense, it interacts strongly with the pump beam and produces observable sum frequency. The tuning of idler beam can be characterized by monitoring this sum frequency. This is due to the fact that whenever there is a hop in either the pump or the signal, a hop will show up in their difference frequency (i.e., idler beam) as well as their sum frequency. This greatly facilitates the measurement because it is much easier to characterize the visible sum frequency beam instead of mid-infrared idler beam.

The characterization of sum-frequency MHF tuning is achieved with a Fabry-Perot interferometer (lower-right dashed box in Figure 2). The solid red curve in Figure 2-6 is the sum-frequency Fabry–Perot spectrum at one pump wavelength. We observed a series of transmission peaks separated by etalon free spectral ranges (FSR = 10 GHz). When the tuning is MHF, the transmission peaks of the sum frequency is shifting exactly the same amount of frequency as the pump wavelength, no matter how small/large that change is. An example is shown in Figure 2-6. When the pump frequency is increased by a step 1.5 GHz, the transmission peak positions of sum frequency is shifted by 1.5 GHz, proving there is no mode hop during this tuning event. (Dashed-dotted blue line in Figure 2-6) Consequently, one could identify the mode hops when the transmission peaks do not appear

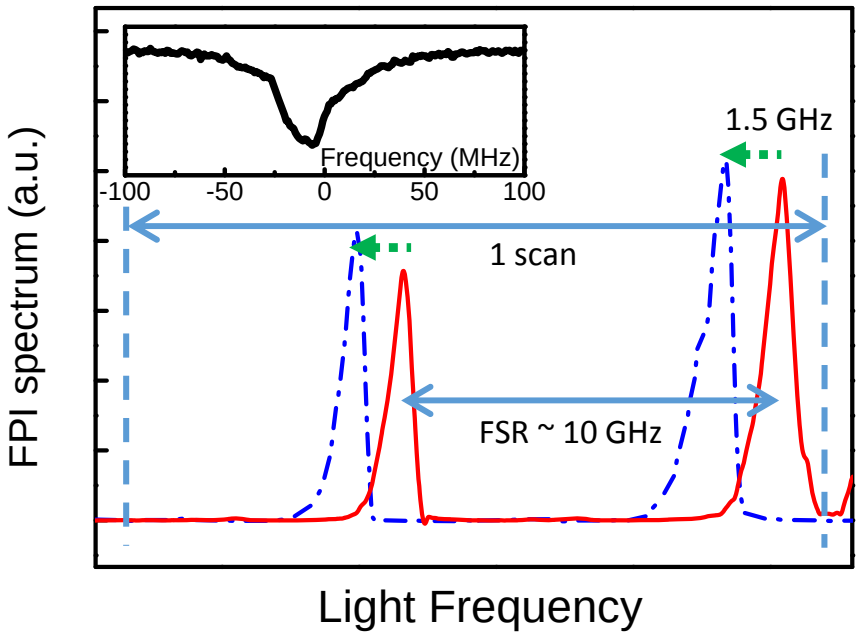

Figure 2-6 Calibration of MHF tuning of sum frequency. The solid line shows sum-frequency Fabry–Perot spectrum [free spectral range (FSR) 10 GHz)] at pump frequency; the dashed-dotted line shows the shift of the transmission peaks of the sum frequency. A smooth, continuous shift of the sum frequency as the pump wavelength is tuned confirms that there is no mode hop. Inset shows the spectrum of the sum frequency measured by a finer resolution FPI. It yields an upper limit of idler linewidth at 50 MHz.

at expected positions in each step as the pump wavelength is scanned over the entire spectral range. Scans were repeated with Fabry–Perot interferometer with different FSRs and varied pump frequency increment steps to rule out the possibility of mode hops over a multiple of FSRs. Based on the technique described above, we characterized our idler tuning with a signal fixed at 1535.44 nm and temperature optimized according to Figure 2-5. Mode hops of the sum frequency were repeatedly observed around pump wavelength 1061.0, 1064.4, and 1068.6 nm when the pump is tuned from 1061 to 1072 nm. They are indicated by red arrows in Figure 2-7a. These three mode hops are attributed to the mode hops in the pump, which are explicitly characterized with another FPI. There is also occasionally one or two more mode hops observed in sum frequency at random pump frequencies and are not repeatable in different scans. Those mode hops are likely to arise from acoustical perturbations of either the pump or the SRO cavity. However, the largest MHF tuning range for the idler exceeds 30 cm^{-1} (900 GHz), which is the largest MHF tuning range at the date we reported it. This range is likely to be extended with pump of larger MHF tunable range.

Besides this large mode-hop free tuning range, we also calibrated the spectral linewidth of the sum frequency output (Figure 2-6). This linewidth provides an upper limit

to the idler linewidth. We measured an upper limit of the linewidth of 50 MHz, which is set by the FPI spectral resolution.

With this capability, we tested our cw OPO with methane absorption within our first MHF tuning range (pump wavelength from 1061 nm to 1064 nm). As shown in Figure 2-7, our laser mapped out the sidebands of the C-H bond stretching mode due to rotational-vibrational coupling. This measurement (Gray trace in Figure 2-7b) matches accurately with the HITRAN database simulation (Red trace in Figure 2-7b) and demonstrates the MHF tuning capability of our laser.

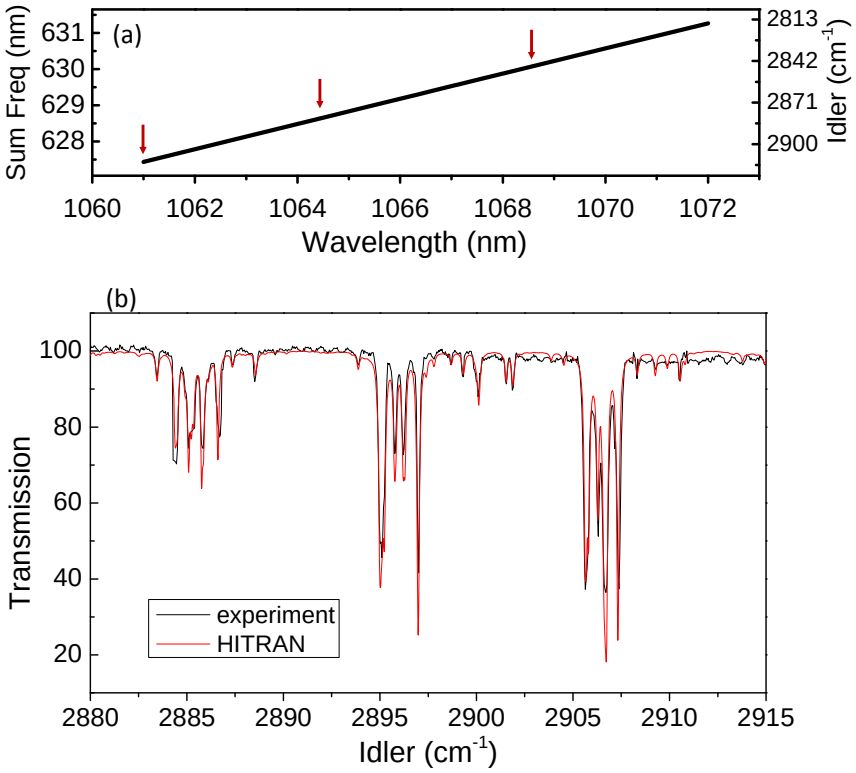

Figure 2-7 MHF tuning range of OPO idler output (a) Idler's MHF tunable range as pump tuning; the arrows show where hops happen repeatedly, (b) experimental and HITRAN-simulated methane absorption within our first MHF tuning range. The methane gas was injected into a gas cell of 0.5 cm length in atomospherical pressure.

Other important figures of merit of the laser are the power output and beam shape M^2 factor. Figure 2-3 shows the pump depletion and idler power output at 2900 cm^{-1}. The maximum idler power of 0.9 W can be delivered at the pump power of 10 W, which has a depletion of about 30%. This idler output power does not vary significantly (<20%) during our MHF tuning process. The output beam is also nearly diffraction limited (M^2 ~ 1.1 in both x and y directions) and is suitable for high precision measurements and waveguide coupling.

2.6 Summary

To sum up, we have demonstrated an MHF tunable mid-infrared OPO by synchronously varying the pump frequency and the crystal temperature while keeping the signal light at fixed frequency. The largest MHF tuning range of 30 cm^{-1} was achieved, which was limited by the mode hopping of the pump laser. The tuning range could be improved further by eliminating mode hops from the pump and by adoption of frequency stabilization mechanisms (*14*). This OPO presents an ideal tool for infrared spectroscopy of molecules and is ready to be combined with STM for *in situ* vibrational spectroscopy, which we will describe in the next chapter.

Chapter 3 – Infrared Laser Spectroscopy in Scanning Tunneling Microscope

3.1 Introduction

3.1.1 Infrared Spectroscopy

Infrared spectroscopy provides a versatile tool to qualitatively and quantitatively understand the chemical properties (*4*). Due to strong light-mater interaction with vibrational modes in molecules and phonon bands in crystals, prominent vibrational resonances could be identified through infrared spectroscopy. Infrared spectroscopy for molecular bonds, in particular, has been known as a key identification tool. First, vibrational resonances for molecular bonds are usually very sharp (less than 1 cm^{-1}, see Figure 2-7) because these vibrations usually lack efficient relaxation channels and thus have a long lifetime. Second, vibrational peaks for certain chemical bonds are well-documented and they differ substantially with even a slight modification of the constituent elements. These two properties combined make the infrared spectra the fingerprints of the chemical bonds and the molecular species.

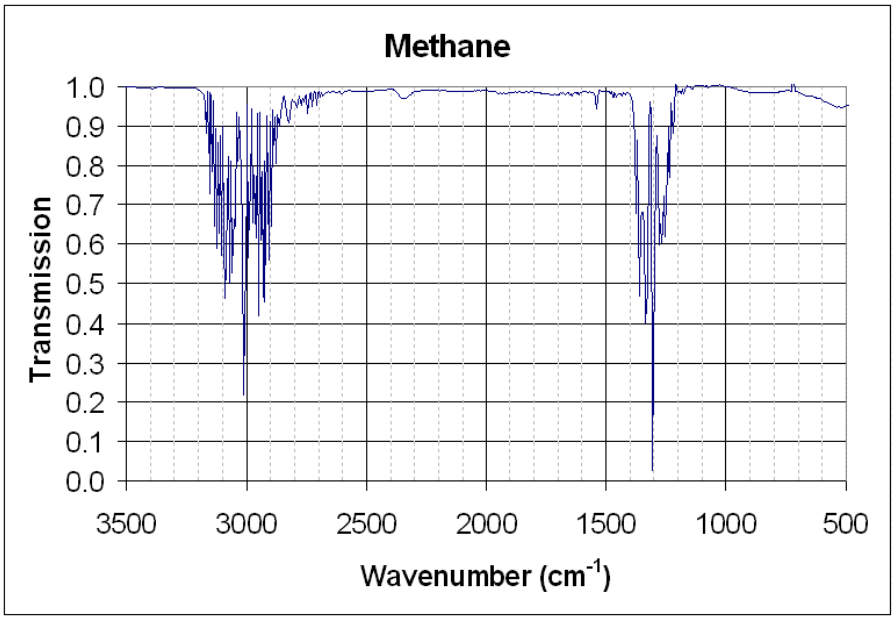

Figure 3-1 Infrared Spectroscopy of Methane Gas

Practically, vibrations located within the mid-infrared range (2.5 μm - 20 μm) are measured because this is the spectral range most of the vibrational peaks would be located at and with which commercial detectors are available. The vibrational peaks are usually

displayed in units of wavenumber. The wavenumber is the inverse of wavelength in the unit of cm^{-1} (2.5μm - 20 μm corresponds to 4000 cm^{-1} – 500 cm^{-1}) and it is convenient to use because it is proportional to energy of photons. Shown in Figure 3-1 is an infrared spectrum of methane in gas phase. The 3000 cm-1 and 1300 cm-1 bands are the CH stretching modes and bending modes respectively. The wings are fine-structures mainly from vibrational-rotational coupling. A zoomed-in spectrum around 2900 cm^{-1} stretching mode rotational sideband was shown in Figure 2-7 and they are composed of even sharper resonances with width less than 1 cm^{-1}.

3.1.2 Scanning Tunneling Microscope (STM)

Scanning tunneling microscopy is an instrumentation developed since 1980s for ultrahigh resolution surface imaging and spectroscopy at atomic scale (*16*). It enables visualization of single atoms and molecules on surfaces in real space and direct exploration of exotic quantum phenomenon such as quantum corrals (*17*).

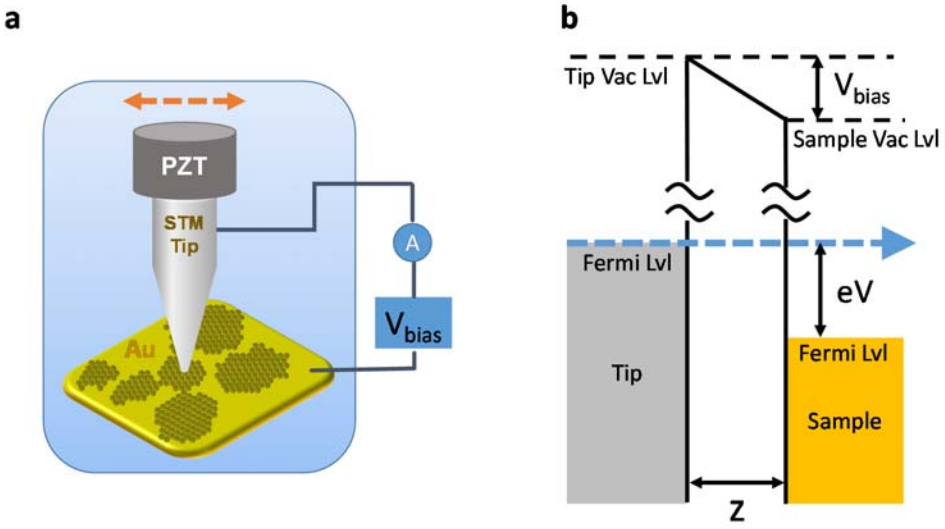

Figure 3-2 Working Principle of Scanning Tunneling Microscope. a. Schematic illustration of the physical setup with tunneling circuit. **b.** Illustration of tunneling under a bias.

The enabling physics underneath this powerful tool is the quantum tunneling effects. As shown in Figure 3-2a, when a metallic tip is brought to close proximity of the conducting sample substrate (~ 1 nm separation) but not yet touching the sample, a current develops between the tip and the sample i.e. electrons move from tip to the substrate or vice versa. Classically an electron from the tip would not be able to go through the vacuum space between the tip and the sample. However in the quantum description, there is a certain probability that an electron would penetrate this vacuum barrier and "tunnel" to the other side of the vacuum, as shown in Figure 3-2b.

The tunneling probability is related to the electron wavefunction overlap between the tip and the sample. The electron wavefunction in one-dimensional case can be approximated as

$$\boldsymbol{\varphi(z) = \varphi(0)e^{-kz}} \qquad \text{Eq. 3-1}$$

Where

$$\boldsymbol{k = \frac{\sqrt{2m(V-E)}}{\hbar}} \qquad \text{Eq. 3-2}$$

z is the tip-sample distance and $(V - E)$ is the potential barrier for the tunneling electrons. The tunneling probability and thus the tunneling current can be described by

$$\boldsymbol{I(z) \sim |\varphi(z)|^2 \sim e^{-2kz}} \qquad \text{Eq. 3-3}$$

Because the current depends on the tip-sample separation in an exponential way, the current acquires a very high sensitivity on the distance and is extremely localized. This behavior enabled the high resolution detection in the vertical direction and lateral direction, which allowed atomic-scale topography and local density of states measurements.

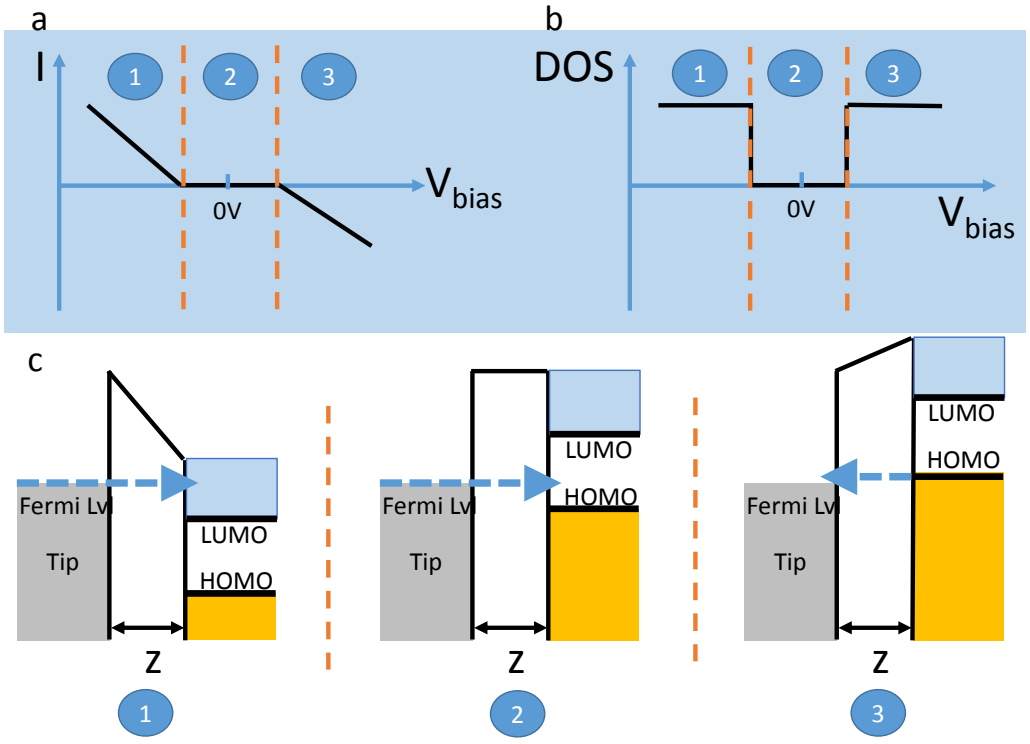

Figure 3-3 Illustration of probing local density of states by STM tunneling current. (Assuming the DOS is constant both above the LUMO and below HOMO.) DOS is proportional to dI/dV. Region 1 has the tip Fermi level aligned with empty states in the substrate, and the probability of tunneling into that state is proportional to all the available states below that energy. Region 2 has the tip Fermi level inside the gap of the energy states of the substrate. Density of states is zero and yields zero dI/dV. When bias is further increased and we reach Region 3, and all the filled states in the sample will tunnel to the tip. LDOS can also be derived from the dI/dV curve.

On the other hand, electrons only tunnel into empty states. By varying the bias voltage between the tip and sample, one can in principle vary the relative energy states between the tip and the sample. With well-defined tip electron states, by observing the current change as a function of bias voltage, one would be able to map out the local density of states of the sample (*18*). As shown in Figure 3-3, with forward bias the electrons could tunnel to states above the lowest unoccupied molecular orbits (LUMO) and the tunneling probability (and current) is proportional to how many empty states are available below the electron energy and above the LUMO. (Region 1) Similar case happens with reverse bias when the electrons from the highest occupied molecular orbitals in the sample could tunnel to the tip. (Region 3) When the Fermi level in the tip happens to align to the gap regions of the sample, no tunneling current would be observed. (Region 2) The current will behave as in Figure 3-3a. A direct differentiation of the current as a function of bias voltage would be able to tell us the density of states at that electron energy level. As shown in Figure 3b, the density of states could be mapped out with varied bias. Note in Figure 3, we assumed a simplified picture where the density of states is a constant below HOMO and above LUMO.

3.2 Chemical Sensitivity and the Need for Infrared

Despite the great achievements of scanning tunneling microscope, it still has certain drawbacks. One of the major drawbacks is the limited chemical sensitivity.

To date, the most common way to probe the molecular vibrations in STM is through the inelastic electron tunneling spectroscopy (IETS) (*19*), which is developed after 17 years of invention of STM. As shown in Figure 3-4a, a higher energy electron could relax the excessive energy through a vibrational mode of the molecular bond during the tunneling process, which effectively created a new tunneling channel. The DOS (dI/dV) will be increased by a constant when the excess energy between the initial and final states has more energy than the vibrational energy. A peak or dip will emerge in the second derivative (d^2I/dV^2) that shows the exactly the vibrational spectroscopy (Figure 3-4b).

Although IETS presents a very useful technique to access the molecular vibration, it only contributes about 1% of the total tunneling current, which requires extremely good electrical and mechanical stabilities of the STM system. (*19*) This stringent requirement limits this technique to very few strong molecular bonds, and can only be detected by the most stable STMs working in cryogenic temperature. Furthermore, IETS has a limit in terms of spectral resolution due to thermal broadening, which is about 27 cm^{-1} at 4 K temperature, as compared to sub-10cm^{-1} molecular vibrational features.

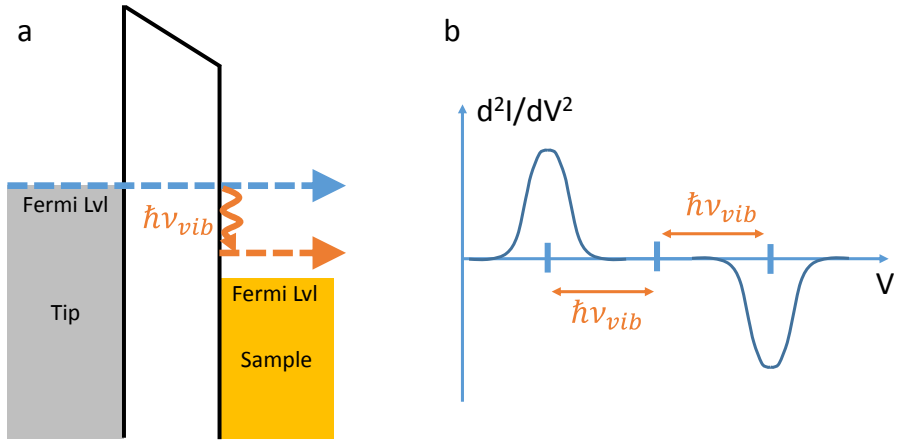

Figure 3-4 Illustration of IETS. a. an additional tunneling channel is opened when the electrons has excess energy larger than the vibrational energy quanta. **b.** As a result of opening up or close down an additional channel, the conductance measurement (d^2I/dV^2) shows peak and dip at the vibrational energy quanta.

3.3 Combining Infrared Laser with STM

A natural way to detect molecular species is through infrared spectroscopy, which really provides fingerprints of the molecules. This will enable the combination of the advantages of STM and laser spectroscopy.

With a STM, one could map out the morphology of the molecular self-assembly, and probe the electronic band-structure at single molecule level through STS. At the same time, an IR spectroscopy could be used *in situ* to identify the molecule under investigation and obtain the vibrational properties.

There are different ways to combine IR spectroscopy with STM. One interesting way to combine them is to excite the molecules with laser and detect the light-induced change with the STM. Our home-build cw OPO (described in Chapter 2) is suitable for exciting the molecules on metal due to its stable output, high power, mode-hop free tunability and narrow linewidth.

3.4 Principle of Detection

The most conceptually appealing way to combine STM and infrared lasers would be exciting the tip-sample junction by the laser, and the STM tip would probe locally the structural/electronic property change of the molecule induced by light. Unfortunately, there will be relatively large thermal expansion due to the absorption of the infrared laser by the junction, especially with the strong local field enhanced by the junction itself. Therefore this technique requires extremely stable laser because the tip-substrate distance will be

modulated by the laser power fluctuations and pointing fluctuation and results in a large noise due to the ultrasensitive distance dependence in the detection.

Since the thermal expansion is so easily detectable in the STM, we could make use of this sensitivity to study the molecule adsorbates. The simplest idea would be shine light at a molecule monolayer somewhere near the tip and detect the thermal expansion of the substrate with the ultrahigh vertical sensitivity of STM. When the infrared laser is off-resonant with the molecule, the absorption mainly happens at the metal substrate, which has a flat spectral response, i.e. the absorption does not depend on wavelength. There will be an initial thermal expansion when the laser is turned on, and it reaches thermal equilibrium in a short period of time. Once the laser wavelength is tuned to resonant with the molecules, the additional absorption channel is opened and more energy will be absorbed by the molecules. The vibration of the molecule relaxes quickly in 10 ps due to the interaction with the substrate and the energy is transfer to the substrate, causing the substrate to expand further. Therefore the varied amount of thermal expansion when the laser is scanned across the vibrational modes of the molecules yields the adsorbates vibrational spectra. This technique couples infrared light into STM and enabled new chemical capabilities of STM. We call it IRSTM.

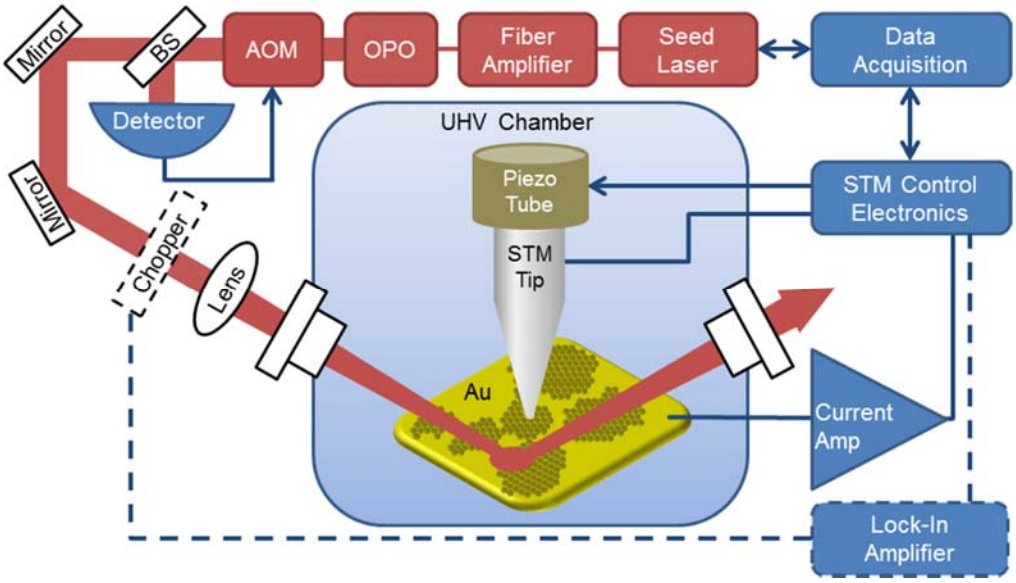

Figure 3-5 Schematic illustration of the IRSTM.

3.5 Measurement with Monolayer of Tetramantane

IRSTM was used to measure IR absorption spectra of tetramantane molecules on a Au(111) surface (*20*). Tetramantane ($C_{22}H_{28}$) belongs to the family of diamondoids, the nanoscale form of diamond. They contain three adamantine cages and can be formed in two isomers, [121]tetramantane [inset of Figure 3-6a] and [123]tetramantane [inset of Figure 3-6b]. They were chosen to demonstrate our IRSTM technique because

[121]tetramantane on Au(111) exhibits a pronounced CH stretch mode that has been previously observed using STM IETS (*21*) and the two isomers shows similar STM typologies but distinct IR spectra. The molecules were extracted from petroleum and purified into powder form (*22*). The powders were sublimated in vacuum at temperatures in the range of 30 ºC – 34 ºC onto a clean Au(111) surface held at room temperature, resulting in coverages ranging from 0.5 to 1.0 monolayer (ML). STM measurements were performed using a homemade ultrahigh vacuum (UHV) variable temperature STM operating at T = 13–15 K. Figures 14a and 14b show typical STM images of [121]tetramantane/Au(111) and [123]tetramantane/Au(111), respectively. The two molecules look similar in their topography, although the [121]tetramantane packaging is slightly elongated in the direction of the molecular lattice vector labeled a [Figure 3-6a].

IR excitation of the tetramantane/Au(111) surface was performed using a homemade tunable mode-hop free OPO (Chapter 2). The setup is shown in Figure 3-5. We used a feedback loop to stabilize the IR light intensity entering into the STM chamber and we achieved less than 0.5% fluctuation. The laser beam (total power ~30 mW) was guided into the UHV STM chamber from a CaF_2 viewport. The beam was focused with an external lens to a typical final spot size of 1.2 mm diameter on the sample. The beam center was intentionally guided to deviate from the tip substrate junction with a typical distance 0.8 ~ 1.5 mm. This was done to avoid direct light excitation of the tip-sample tunnel junction, thus eliminating the effects of tip thermal expansion, rectification, and thermoelectric current generation (*23*). Under these conditions, we found no significant difference apart from overall amplitude variation among IRSTM spectra taken at different lateral distances from the laser spot to the tunnel junction or with different laser spot sizes. IRSTM spectra were measured in two different modes: 1. with optical chopping of the laser light and detect the change of tunneling current with a lock-in amplifier (ac mode) and 2. without optical chopping and detect the tunneling current directly (dc mode).

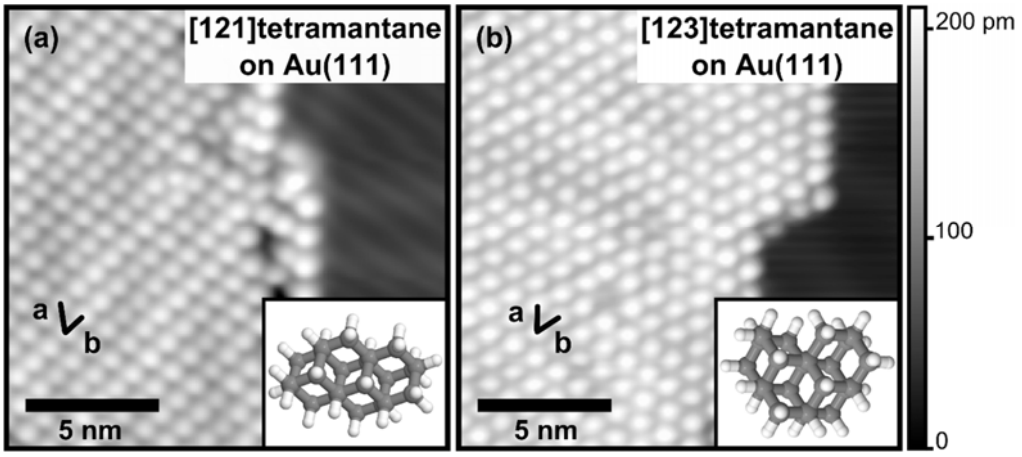

Figure 3-6 STM topography of [121]tetramantane and [123]tetramantane molecules on Au(111). a. (V_{sample} = 1.0 V, I = 50 pA, T = 13 K). The molecular lattice has an oblique structure with lattice constants |a| = 11.1 ± 0.1 Å, |b| = 8.3 ± 0.1 Å, and an interior angle of 59º ± 1º. The inset shows a model of [121]tetramantane (gray and white balls represent carbon and hydrogen atoms). **b.** (V_{sample} = 1.0 V, I = 50 pA, T = 13 K). Within experimental resolution, [123]tetramantane molecules form a hexagonal structure with |a| = |b| = 9.8 ±

0.1 Å, The inset shows a model of P [123]tetramantane [our [123]tetramantane/Au(111) samples were prepared from a racemic mixture containing P and M enantiomers].

3.5.1 DC Mode and AC Mode Operation of the IRSTM

Figure 3-7a shows the IRSTM spectrum of a monolayer of [121]tetramantane measured using the ac mode. Here, the modulation of STM Z signal was measured with a lock-in amplifier at the laser chopping frequency under constant-current feedback conditions. The IR laser frequency was scanned from 2830 to 2940 cm^{-1}. A control experiment is done with the same measurement on bare Au(111) for reference. Six IR absorption peaks can be identified at 2850 cm^{-1}, 2855 cm^{-1}, 2881 cm^{-1}, 2897 cm^{-1}, 2909 cm^{-1}, and 2920 cm^{-1} for [121]tetramantane/Au(111). The appearance of these peaks demonstrates more absorption and hence larger thermal expansion at the corresponding IR frequencies and, therefore, can be attributed to [121]tetramantane vibrational modes at these frequencies. We could estimate the absorption of [121]tetramantane monolayer from the molecules by checking the ratio of the peak heights ($\sim 7 \times 10^{-4}$ Å shown in Figure 3-7a) to the background level ($\sim 1 \times 10^{-2}$ Å in Figure 3-7a), which corresponds to the absorption of the [121]tetramantane monolayer and the bare gold absorption respectively. Assuming that polished gold at low temperatures absorbs ~1% of IR light (*24*, *25*), we could estimate ~0.07% for one monolayer of [121]tetramantane. This corresponds to an absorption cross section of 6×10^{-18} cm^2 per molecule.

We also performed IRSTM measurements of [121]tetramantane in the dc mode by direct measuring the Z position in a constant current mode. This is a faster measurement than the ac mode, since the ac mode requires low optical chopping frequencies and long lock-in time constants. Figure 3-7b shows the dc IRSTM spectrum of 0.7 ML of [121]tetramantane on Au(111), as well as a bare Au(111) reference spectrum. The [121]tetramantane/Au(111) spectrum shows peaks relative to the bare Au(111) spectrum at the same energy positions as in Figure 3-7a. These peaks are therefore attributed to extra light absorption by [121]tetramantane molecules. The dc IRSTM spectra reflect the same information as ac spectra, but the peak amplitude is harder to quantitatively interpret due to the lack of a well-defined overall absorption reference point (i.e., such as the bare gold absorption). Because it is a dc measurement, the spectra are also more strongly affected by unavoidable drifts in the experimental setup. These drifts are caused by redistribution of the thermal fluxes inside the STM due to the fact that the tip-sample temperature equilibrium depends very sensitively on parameters such as sample orientation, beam path, and laser power stability. However, after a baseline subtraction [i.e., subtraction of a third

order polynomial fit to the estimated bare Au(111) contribution to the spectrum], the vibrational spectra look very similar for both ac and dc measurement modes.

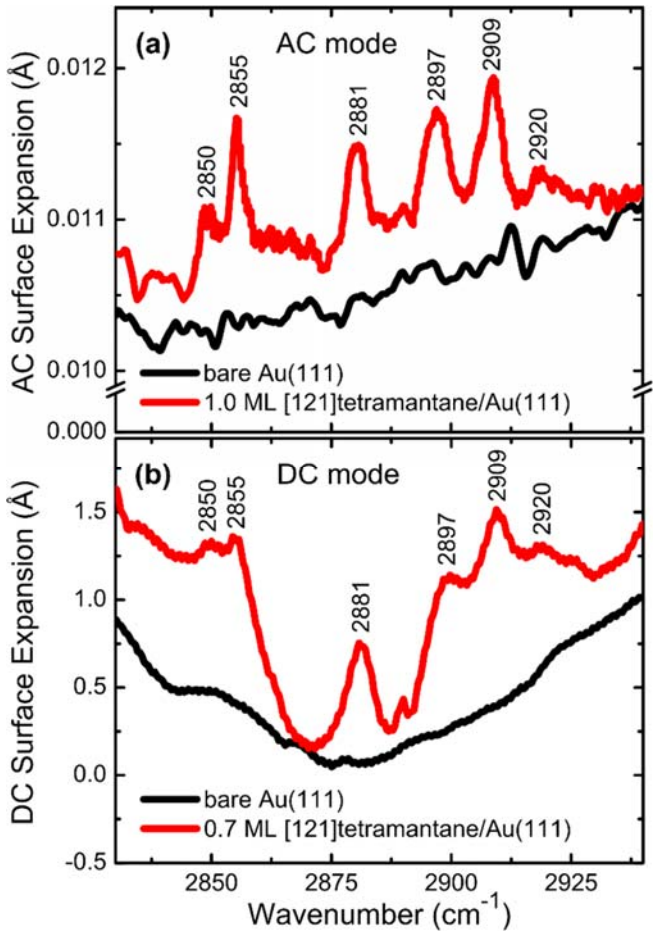

Figure 3-7 Vibrational spectra of [121]tetramantane submonolayer measured by IRSTM. (a) Differential ac surface expansion due to absorption of modulated IR light, measured via lock-in amplifier for constant-current STM Z signal (chopper modulation frequency ~13 Hz, lock-in amplifier time constant 3 s). The black (lower) and red (upper) lines show ac surface expansion of bare gold and [121]tetramantane-decorated gold, respectively. (b) dc surface expansion of bare gold (black lower line) and [121]tetramantane-decorated gold (red upper line) as a function of incident IR frequency, measured via constant-current STM Z signal.

In order to demonstrate the potential of IRSTM for chemical characterization, IRSTM spectroscopy was additionally performed on samples of [123]tetramantane. As seen in Figure 3-6, both molecular species form similar self-assembled overlayer structures on Au(111). Figure 3-8 shows DC IRSTM spectra of 1 ML of [121]tetramantane on Au(111) versus 0.9 ML of [123]tetramantane on Au(111), (after baseline subtraction). The two spectra are clearly distinct from each other, and both exhibit several well-resolved peaks. Peak energies were extracted by fitting Lorentzian lines to the spectra (fits can be seen in Figure 3-8). [123]tetramantane/Au(111) vibrational peaks are found at 2852±1, 2866±1, 2876±1, 2908±1 cm^{-1}, and 2915±1 cm^{-1}, while the [121]tetramantane/Au(111) peaks are

seen at 2850±1, 2855±1, 2881±1, 2897±1, 2909±1, and 2920±1 cm^{-1}. This illustrates the power of IRSTM to distinguish submonolayer amounts of even closely related chemical compounds.

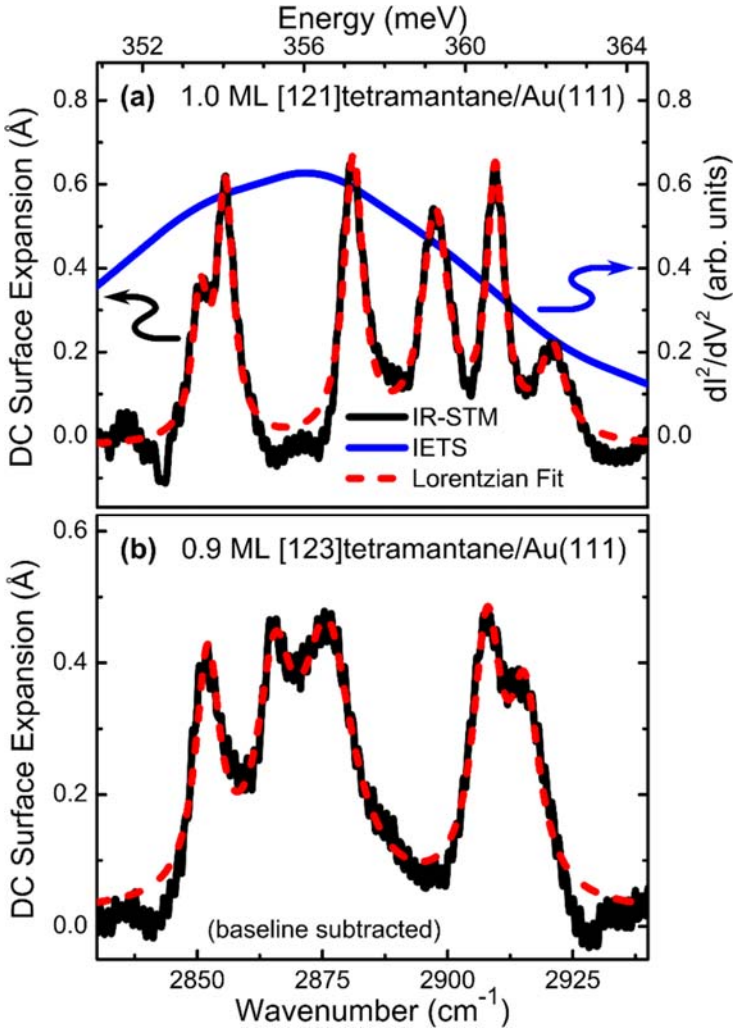

Figure 3-8 dc surface expansion due to molecular IR absorption as a function of incident IR frequency. (a) The black solid line shows the average dc surface expansion of [121] tetramantane/Au(111) (five sweeps) with gold baseline signal subtracted. The blue line (with a single broad peak) shows an STM d^2I/dV^2 spectrum of [121]tetramantane/Au(111) from Ref. (*21*). (b) The black solid line shows the average dc surface expansion of [123]tetramantane/Au(111) (twelve sweeps) with gold baseline signal subtracted. The red dashed lines are (a) six-peak and (b) five-peak Lorentzian fits to the experimental data.

3.5.2 Comparison with IETS

It is instructive to discuss some differences between IRSTM spectroscopy and STM-IETS. Figure 3-8a shows a d^2I/dV^2 spectrum of [121]tetramantane/Au(111) from Ref. (*21*) (the blue line). The IETS peak (obtained at the lower temperature of T = 7 K with bias

modulation voltage amplitude V_m = 1-10 mV) is much broader in energy and cannot resolve any of the multiple CH stretch modes that exist in this energy range. Since IETS energy resolution depends on temperature and bias modulation voltage amplitude (*26*), the IETS spectral resolution in Ref. (*21*) is estimated to be 30 cm^{-1} at best. In contrast, the energy resolution for IRSTM is determined by the spectral accuracy of the laser. For tunable IR lasers the spectral uncertainty mainly arises from mode hops which cause sudden changes in the frequency of emitted light. The laser used here was found to be nearly free of mode hopping over the scanned frequency range from 2830 to 2940 cm^{-1} (an average of three hops occur per scan, each of magnitude < 1 cm^{-1}) (Chapter 2). We therefore conservatively estimate the spectral resolution of IRSTM to be no worse than 1 cm^{-1} across the frequency range explored here. It should be noted that IRSTM also differs from STM-IETS in that IRSTM probes IR-active vibrational modes with the dipole moment perpendicular to the metal surface, while STMIETS active modes do not obey rigorous selection rules (*27*, *28*).

3.5.3 Discussion of Linewidth and Molecular Interactions

The linewidths observed using IRSTM carry information regarding molecular interactions. Our tetramantane/Au(111) linewidths were found to be in the range of 4-12 cm^{-1} (full width at half maximum), corresponding to vibrational lifetimes in the range of 0.4-1.3 ps. Our experimental energy resolution ($\leq$ 1 cm^{-1}) and the homogeneity of our samples imply that this broadening is not instrumental, but is rather due to molecule-molecule and molecule-substrate interactions (as well as possibly overlapping modes). We observed notably less broadening of tetramantane CH stretch modes for molecules on Au(111) compared to previously measured powder samples (typical widths for the powder measurements (*29*) are on the order of 10-20 cm^{-1}). Two main factors likely account for this difference: measurement temperature (13-15 K for the surface measurements versus room temperature for the powder measurements) and structural differences between surface and bulk systems. Other aspects of the local environment, such as the number of nearest neighbors and the relative coupling strengths between them, can also affect peak broadening. Molecules arranged in two-dimensional lattices (as measured here) are surrounded by a smaller number of nearest neighbors and so can be expected to exhibit less broadening compared to the three-dimensional environment experienced by molecules in a powder. Interaction of molecules with a metal substrate, on the other hand, is expected to broaden peaks due to the efficient energy relaxation channels. Since we see an overall narrowing of vibrational peak widths compared to bulk measurements, we conclude that the narrowing effects of lower temperature and reduction in coordination dominate over the broadening effects of the molecule-surface interaction.

Further information regarding molecule-molecule interactions can be inferred by comparing IRSTM measurements to bulk measurements performed on powder samples. Peaks at notably different energies are observed in bulk powders of different tetramantane isomers, specifically, at 2840, 2863, 2884, and 2901 cm^{-1} for [121]tetramantane and at 2847, 2871, and 2903 cm^{-1} for [123]tetramantane (*29*). There is not a perfect one-to-one correspondence between these bulk vibrational modes and the adsorbate modes reported here, but the peaks for the surface measurements do appear overall to be shifted to higher frequencies. We assume this is not due to mechanical renormalization (*30*) since the

molecules are not covalently bonded to the metal surface (*21*). Furthermore, doping effects are expected to be insignificant since tetramantane molecules have a large gap between the highest occupied and lowest unoccupied molecular levels, and therefore very little charge transfer between molecules and the gold surface is expected to occur (*21*). Two mechanisms that might be at work here are the coupling of dynamic molecular dipole moments to substrate image charges (a redshifting effect) and dynamic dipole-dipole coupling between molecules (a blueshifting effect) (*30*, *31*). The fact that the vibrational peaks for surface-adsorbed molecules tend to be blueshifted relative to the peaks for powder samples implies that intermolecular dipole-dipole coupling for the surface samples plays a more important role than coupling of the dynamic dipole moments to their images in the substrate. This is consistent with recent observations of appreciable attractive van der Waals interactions in diamondoid dimer structures (*32*, *33*).

3.6 Outlook and Concluding Remarks

In conclusion, we have demonstrated the feasibility of IRSTM for performing IR spectroscopic studies of molecular submonolayers on metallic surfaces by combing a tunable IR laser and an STM. We have shown that the excellent spectral resolution of IRSTM can be used for chemical characterization of molecular adlayers, as well as for measurements of single-molecule optical absorption cross sections. IRSTM measurement of tetramantane molecules on gold reveal that adsorbed tetramantane vibrational peaks are narrowed and blueshifted relative to bulk measurements, implying that intermolecular interactions for adsorbed tetramantane have a stronger influence on molecular vibrational resonances than interaction between tetramantane molecules and the gold surface. Regarding the ultimate sensitivity of this new technique, we believe that lasers with better intensity stabilization and substrates with increased thermal expansion coefficient (such as based on a bimetallic strip principle) could significantly improve the IRSTM sensitivity compared to the sensitivity achieved in this work.

Chapter 4 – Optical Imaging and Spectroscopy of Individual Carbon Nanotubes

4.1 Introduction

Carbon nanotube is a one-dimensional tube consisting only carbon atoms that can be visualized intuitively as a rolled up graphene sheet. The C-C bond in nanotube is among the strongest covalent bond that is responsible for the nanotube's remarkable mechanical strength (*34*) and chemical inertness (*35*). Nanotube also demonstrate ballistic electronic transport(*36*, *37*), efficient electrical tunability (*38–40*) and extraordinary current carry capacity(*41*, *42*). With these properties, nanotube hold great promise in next generation nano-electronics. In addition to the technological significance, the nanoscale diameters helps forming a model system for studying physics in one dimension, featuring many fascinating theoretical predictions.

Although carbon nanotubes presents outstanding application potentials and interesting physics, there is a significant hindrance to the development of this field: there is few convenient table-top single-tube characterization tool. In this chapter, I will first introduce the electronic and optical properties of carbon nanotubes and then I will present a new technique we developed for convenient optical imaging and characterization of individual nanotubes. Finally I will discuss the applications of this technique.

4.1.1 Electronic Structure

This system is so appealing to physicists that most of the electronic properties could be exactly calculated by a simple tight binding theory. Carbon atom has 4 outer shell electrons, with 2 electrons in both 2s and 2p states. When one carbon atom connects with the nearby three carbon atoms in graphene with a honeycomb structure, it forms three σ bonds with sp^2 hybridization orbitals. The remaining electron will be in the $2p_z$ orbitals and it forms the covalent π bonds. (Figure 4-1a) The Fermi level is typically around the π band. Since the energy range we are interested in is around the Fermi level, we will be focusing on the effect of the π orbitals in graphene. A tight bonding theory considering only the π orbitals obtains the energy dispersion relation of graphene (*43*)

$$E(\vec{k}) = \varepsilon_{2p} \pm t[1 + 4\cos\left(\frac{\sqrt{3}k_x a}{2}\right)\cos\left(\frac{k_y a}{2}\right) + 4\cos^2(\frac{k_y a}{2})]^{1/2} \quad \text{Eq. 4-1}$$

where ε_{2p} is the energy $2p$ orbital, t is the nearest neighbor overlap potential, a=2.46Å is the lattice constant and k_x, k_y are momentum in x and y respectively. This relation could be simplified in the vicinity of k=0 as (*43*)

$$\boldsymbol{E(\vec{k}) = \varepsilon_{2p} \pm \hbar v_F |k|} \qquad \text{Eq. 4-2}$$

with $v_F = 1 \times 10^6 m/s$ describing the Fermi velocity in the graphene. This means in the vicinity of k=0, the dispersion relation is linear and produces a cone-like structure. This means the electrons behave exactly the same as massless photons with reduced speed.

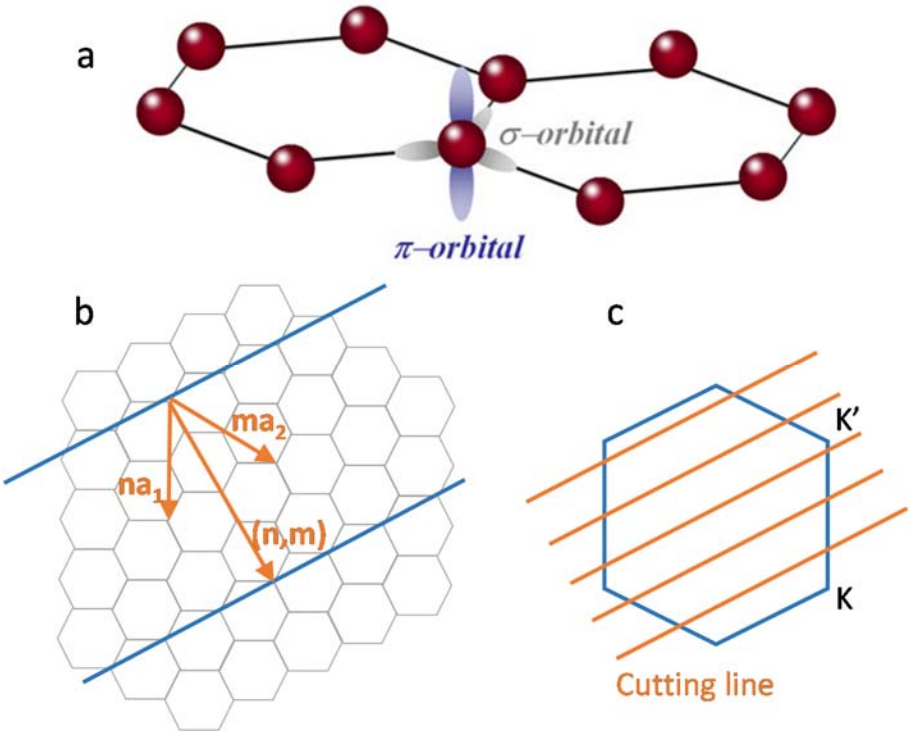

Figure 4-1 Formation of hexagonal structure from sp^2 bonding. a. p_z orbital forms the π bonds. σ bonds are in plane and forms the hexagonal structure. **b.** The chiral vector of carbon nanotubes. The blue line connects together to form a nanotube. **c.** In the reciprocal lattice, the only available states are on the cutting lines because they represent the periodic boundary condition. The behavior around K or K' points are mostly relevant to electrical and optical properties.

The corresponding wavefunctions are determined as (*43*)

$$|\boldsymbol{k}\rangle = \frac{\mathbf{1}}{\sqrt{\mathbf{2}}} \boldsymbol{e^{i\vec{k}\cdot\vec{r}}} \begin{pmatrix} \boldsymbol{-ibe^{-i\theta_{\vec{k}}/2}} \\ \boldsymbol{e^{i\theta_{\vec{k}}/2}} \end{pmatrix} \qquad \text{Eq. 4-3}$$

here θ_k is the angle $\vec{k}$ makes with y-axis, and b is 1 for electrons and -1 for holes. This equation states that there is another degree of freedom: "pseudospin", which can be think of as pointing parallel or anti-parallel to the momentum. Many electronic, optical and thermal properties of graphene and carbon nanotube are determined by this cone-like dispersion structure and the pseudospin of electrons states.

Carbon nanotube electronic structure can be understood from graphene with zone folding in momentum space. (*44*) As depicted in Figure 4-1b, for each nanotube structure we could define a unique chiral vector (n,m) corresponding to the rolling vector perpendicular to the nanotube axis. This defines the boundary condition around the nanotube. Intuitively this means only states along specific lines (cutting lines) in the graphene Brillouin zone are available to a given nanotube. (Figure 4-1c) The final energy eigenstates in the zone-folding description is (*44*)

$$\boldsymbol{E_{\mu}(k) = E_{\mathrm{GR}}\left(\vec{k}_{\parallel} + \mu k_0 \vec{\kappa}_{\perp}\right)},$$
$$\boldsymbol{(\mu = 1}, \ldots, \mathrm{N\ and\ } -\frac{\boldsymbol{\pi}}{\boldsymbol{T}} < \vec{\boldsymbol{k}}_{\parallel} \leqq \frac{\boldsymbol{\pi}}{\boldsymbol{T}}) \qquad \text{Eq. 4-4}$$

where $E_{\mathrm{GR}}(\vec{k})$ is the graphene energy dispersion in vector space, $\vec{k}_{\parallel}$ is the wavevector along the nanotube direction and $\vec{\kappa}_{\perp}$ is the unit vector perpendicular to the nanotube where quantization happens. The subband number is indexed by μ and it defines the cutting line respect to the graphene dispersion. The quantization around the nanotube circumference is denoted by $k_0 = \frac{2}{d}$ for a nanotube with diameter d. N is the number of hexagons of the graphite honeycomb lattice within the nanotube unit cell and T is the magnitude of the unit cell vector along the nanotube axis.

4.1.2 Chirality and Relation to Semiconducting and Metallic Nanotubes

Each chiral vector (n,m) gives a unique specie of nanotubes with distinct band structures. The thermal, electrical and optical properties of the nanotube depends on the band structure around the Fermi level (K points) and therefore the chirality of each nanotube. It provides a systematic way to vary all these properties of nanotube by varying the chiral vector.

It will be therefore essential to look at where cutting lines are near the K point as a function of chirality (n,m) (*44*). The cutting line spacing is $\frac{2}{d} = \frac{2\pi}{a} 2\sin\theta \frac{1}{n-m}$ where θ is the chiral angle ($\theta = 0$ for m=n). On the other hand, the distance between the μ=0 line and the K point is $\frac{2\pi}{a} 2\sin\theta \frac{1}{3}$. Therefore one special case arises when n-m is a multiple of 3, where one of the cutting line go through the K point and density of states is non-zero in the entire energy range around K point, i.e. zero bandgap. Therefore, for this special case, the nanotube is expected to be in the metallic state. All the other chirality nanotubes will not have cutting lines go through the K point and as a result they possess a finite bandgap and

exhibit semiconducting properties. Depending on how far away the nearest cutting line towards the K point, the bandgap changes systematically from zero (metallic) to a few electron volts at small diameters. This is a desirable feature for nanoelectronics where a device is integrated with a single material but exhibits various functionalities.

4.1.3 Optical Transition in Carbon Nanotubes

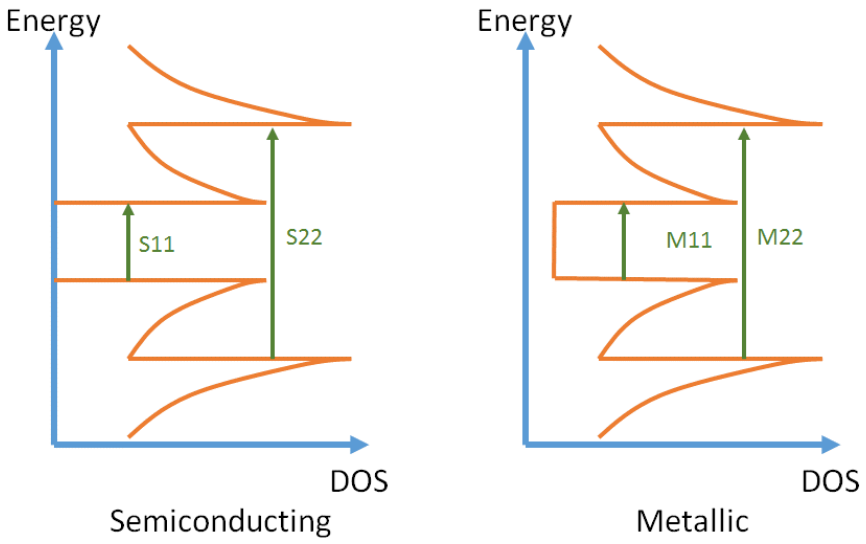

Figure 4-2 Carbon nanotube band structure, van Hove singularity and optical transitions. a. Semiconducting b. Metallic

For each subband corresponding to cutting lines with different μ (besides the cutting line going through K), the energy dispersion of carbon nanotubes (Figure 4-2) has parabolic form $E(k) = E_0 + \frac{\hbar^2 k^2}{2m_{\text{eff}}}$ with m_{eff} depending on μ. In one dimension, this dispersion gives a density of states as $\frac{1}{\sqrt{E-E_0}}$, and divergence happens when E approaches E_0 at the band edge, known as van Hove singularity. As the optical transition is proportional to density of states, the transitions between the band edges dominates the optical response. (Figure 4-2) As we mentioned earlier, the chiral structure of the nanotube determines the electronic band structure, and the band structure would never be the same for different chiralities. Therefore there is a one to one correspondence between a nanotube chirality and the optical transition energies. This enables the nanotube chirality identification with optical transitions energies.

Optical transitions require strict selection rules. For light polarized parallel to nanotube, the optical transition are allowed only when the transition connects the same subband due to the conservation of angular momentum. However transitions connecting adjacent subband are permitted when the light is polarized perpendicular to the nanotube. However because the transition has to satisfy pseudospin conservation. This has to be

limited to the E12 and E21 bands only in semiconductors, as we will discuss in details later in this chapter.

Although many of the optical properties could be understood satisfactorily with the nanotube electronic band structure, the optical transition is really dominated by the excitonic effects due to the enhanced Coulomb interaction in one dimension. With reduced dimensionality, the electrons and holes are confined in a line and effectively reducing their separation and increase their binding energy. Furthermore, the dielectric screening from the material itself is much weaker compared to three dimensional materials. Both of these effects predicts a strong excitonic binding energy in carbon nanotubes. The exciton binding energy has been theoretically predicted by *ab initio* calculation and experimentally verified by two photon photoluminescence spectroscopy to be as large as ~ 0.5 eV. (*45*, *46*)

4.1.4 Single Tube Optical Measurements

The large variety of the nanotube family with more than 200 species, each having distinct structure and properties, poses a significant challenge in characterization of the nanotubes from growth optimization to device performance. Scanning electron microscope (SEM) could visualize the nanotubes but could not differentiate the structure of the nanotube. Transmission electron microscope (TEM), although capable of identifying the chirality of the nanotube, requires the sample to be on a slit. Furthermore, the electrons requires high vacuum and tend to damage the nanotube. Optical measurements with carbon nanotubes, on the other hand, is appealing because it is non-invasive and can provide rich information. However conventional optical measurements are usually done in a water solution of sonicated nanotubes, usually mixtures of different chiralities, in order to have sufficient signal to noise ratio compared to single tube measurements. Beside the mixed information on different nanotube species, interactions between the nanotubes and with the solution environment also perturb the measured properties. A single tube level measurement is necessary for clarified information on intrinsic physics and device performance. However this is extremely difficult due to the weak individual nanotube signal (10^{-4} ~10^{-5} with a micron size focus) compared to laser fluctuations, detector noises and unavoidable environment scattering. Only a handful of single tube spectroscopic techniques are developed so far and they are listed below with their advantages and drawbacks.

1. **Raman spectroscopy** characterizes the vibrational properties of carbon nanotubes. Vibrational spectra of nanotubes can be resonantly enhanced when the excitation energy matches the nanotube transition (*47–51*). In this way, optical resonances can be mapped out by scanning the excitation wavelength. However the requirement for a tunable excitation and the relatively small Raman cross-section pose challenge in probing electronic band structure in this way.

2. Fluorescence measurement on individual semiconducting nanotube is a sensitive measurement that directly probes the E11 transition. Combined with the excitation spectroscopy, higher transitions could also be mapped out by this technique. The disadvantage of this method is it is only applicable to small-diameter semiconducting

nanotubes which has E11 transition in the Silicon or InGaAs detection spectrum range. (*52–54*)

3. Absorption of carbon nanotubes with spatial modulation is used to measure the direct absorption spectrum of a given nanotube on a slit. A nanotube is moved in and out of a laser spot and the transmitted light is been collected by a lock-in amplifier with reference to the modulation frequency. An accurate absorption spectrum could be measured and quantitative cross-section can be obtained. (*55*, *56*) Still, this method requires the sample to be on a slit or index matched transparent substrate, and requires a slow scanning of a large range of wavelengths.

4. Photothermal measurements provides a clever way to detect extremely small signals. (*57*) An intensity-modulated tunable pump beam is focused on to the nanotube and depending on the nanotube absorption, the local temperature and hence the refractive index of the surrounding medium is modulated as well. A probe beam goes through this medium will experience modulated refractive index and develop an additional frequency, which then interferes with the original beam at the detector. A beatnote is detected and is proportional to the absorption coefficient of the nanotube at the pump beam wavelength. Like the drawbacks of most other techniques, this technique suffers from slow laser tuning.

5. Rayleigh scattering spectroscopy is the first demonstration of a broadband method used to identify the electronic transitions of a given nanotube suspended across a slit (*58–61*). It allows probing of the nanotube optical transition through resonant scattering with a dark field geometry. Since broadband illumination is used, this technique simultaneously probe all transitions within the energy range in a single shot. The main drawback is the sample needs to be on a slit in order to avoid the much stronger scattering from unavoidable uneven substrate surfaces. Recently this technique has also been applied to measure samples on a transparent glass, where a refractive index matching oil is filled between the objective and the sample for reduced substrate scattering (*62*, *63*). However this contaminates the sample and will not be suitable for *in situ* device characterization. The Rayleigh scattering technique has been utilized to measure hundreds of different nanotubes and identification of chirality from optical transition has been established with the help of Rayleigh scattering (*61*).

4.1.5 Need for High Throughput Single Tube Microscopy and Spectroscopy

Currently the carbon nanotube device researches face two outstanding challenges, achieving chirality-controlled growth and understanding chirality-dependent device physics. Addressing these challenges requires, respectively, high-throughput determination of the nanotube chirality distribution on growth substrates and *in situ* characterization of the nanotube electronic structure in operating devices.

Although the single tube techniques described above can directly or indirectly obtain nanotube optical properties, but they all lack certain merits as a versatile, high-throughput and non-destructive microscopy and spectroscopy method. This greatly hampers the development of nanotube device applications.

4.1.6 Optical Theorem, Absorption and Homodyne Process

The optical theorem is a general law of wave scattering theory, which states that the total cross-section of the scatter is related to the forward scattering wave. (*5*)

$$\boldsymbol{\sigma_{tot}} = \frac{\boldsymbol{4\pi}}{\boldsymbol{k}} \mathrm{Im}\boldsymbol{f(0)} \qquad \text{Eq. 4-5}$$

where f(0) is the scattered wave at incident angle. From the interferometric point of view, this means the forward scattered electric field destructively interfere with the unperturbed incident field and results in an intensity reduction.

In the case of single nanotube transmission measurement, the absorption cross-section is much larger than the scattering cross-section and dominate the total cross-section. Therefore in a transmission measurement, the transmitted intensity reduction is directly proportional to the absorption of a nanotube.

$$\boldsymbol{\alpha} \simeq \frac{\boldsymbol{\Delta I}}{\boldsymbol{I}} = \frac{|\boldsymbol{E_0} + \boldsymbol{E_s}|^2 - |\boldsymbol{E_0}|^2}{|\boldsymbol{E_0}|^2} = \frac{|\boldsymbol{E_s}|^2 + \boldsymbol{2}\mathrm{Re}(\boldsymbol{E_0 E_s^*})}{|\boldsymbol{E_0}|^2} \sim 2\mathrm{Im}(\boldsymbol{\chi}) \qquad \text{Eq. 4-6}$$
$$\boldsymbol{E_0 = E_i e^{-\frac{i\pi}{2}}}, \qquad \boldsymbol{E_s \sim \chi E_i}$$

where E_i, E_0, E_s are the incident field at sample, incident field at detector and nanotube forward scattered field at detector. The additional phase -π/2 develops when the incident field propagates from the focus (sample) to infinity (detector), known as Gouy's phase. The $|E_s|^2$ term is one order higher and much smaller than the cross term and can be neglected here. As we expected from the optical theorem, the absorption from a nanotube is proportional to the imaginary part of the susceptibility χ.

In the single nanotube reflection measurement, as typical for a microscopy setup, optical contrast of a nanotube can be analyzed in similar way but now the interfering fields are reflected field at the detector E_r and nanotube back-scattered field E_{NT}. This yields an optical contrast

$$\frac{\boldsymbol{\Delta I}}{\boldsymbol{I}} = \frac{|\boldsymbol{E_r} + \boldsymbol{E_{NT}}|^2 - |\boldsymbol{E_{NT}}|^2}{|\boldsymbol{E_r}|^2} = \frac{\boldsymbol{2}|\boldsymbol{E_{NT}}|}{|\boldsymbol{E_r}|}\boldsymbol{\cos\phi} \qquad \text{Eq. 4-7}$$

The phase ϕ denotes the phase difference between E_{NT} and E_r at the detector. In the transmission case $\phi = \pi$ and in the case of a transparent substrate $\phi = 0$. For commonly

used SiO2/Si samples, depending on the oxide thickness ϕ could vary between 0 and π as a result of multilayer reflection.

With this interference in mind, one can intuitively picture the absorption process of nanotubes as a homodyne detection, which has been extensively used in microwave detections by mixing a signal with a reference electric field, referred as local oscillator. In principle, this homodyne detection could greatly enhance the nanotube contrast by reducing the interfering local oscillator electrical field while maintaining the nanotube scattering electrical field. We successfully achieved this contrast enhancement with polarization manipulation.

4.2 Polarization-based Contrast Reflection Microscopy

4.2.1 *Setup*

Light polarization is extremely sensitive to minute optical anisotropy in a system, and has long been exploited to study materials ranging from molecules to crystals. Manipulation of polarization is especially suitable for the study of carbon nanotubes because of the strong depolarization effect of these one-dimensional structures. Figure. 19a illustrates the polarization manipulation in a reflection geometry (*64*). Horizontally polarized incident light (after polarizer P_1) illuminates a nanotube oriented at 45 degrees. (Figure 4-3b) The nanotube scattered electrical field (E^0_{NT}) is polarized along the nanotube direction (due to a strong depolarization effect on light perpendicularly polarized to nanotube), while the substrate reflection (E^0_r) retains the horizontal polarization, with $E^0_{NT} / E^0_r \sim 10^{-4}$ (Figure 4-3c). The second polarizer (P_2) is oriented close to vertical direction (with a small angle deviation of δ), which strongly reduces the reflection field to $E_r = E^0_r \sin\delta$, but largely keeps the nanotube field $E_{NT} = E^0_{NT} / \sqrt{2}$. Therefore the nanotube contrast is enhanced by $1/(\sqrt{2}\sin\delta)$, which can reach over 100 with a reasonably small δ and produces $E_{NT}/E_r > \sim 10^{-2}$ (Figure 4-3d).

Although the concept of polarization enhancement is appealingly simple, its experimental implementation to achieve wide-field imaging and spectroscopy of single nanotubes on substrates has been challenging due to constraints of polarization control in optical microscopy. Indeed, no individual carbon nanotubes on substrates have ever been observed in a regular polarization microscopes with high numerical aperture (NA) objectives, because their polarization extinction is typically several hundred (*65*), too low to achieve sufficient contrast enhancement. Recently a specialized polarization-based transmission microscopy was employed to probe single-nanotube optical absorption (*66*), but the technique is limited to suspended carbon nanotubes with no background from the substrate (as in previous Rayleigh scattering measurements (*58–63*)). In addition, it requires slow frequency scanning of a Ti:sapphire laser. Our technique simultaneously achieves a polarization extinction ration of 10^5 (more than one order of magnitude higher than a conventional microscope) and a sub-micron spatial resolution in a reflection

microscope using novel polarization control and broadband supercontinuum illumination. It allows us to demonstrate wide-field imaging and high-throughput spectroscopy of individual nanotubes in devices.

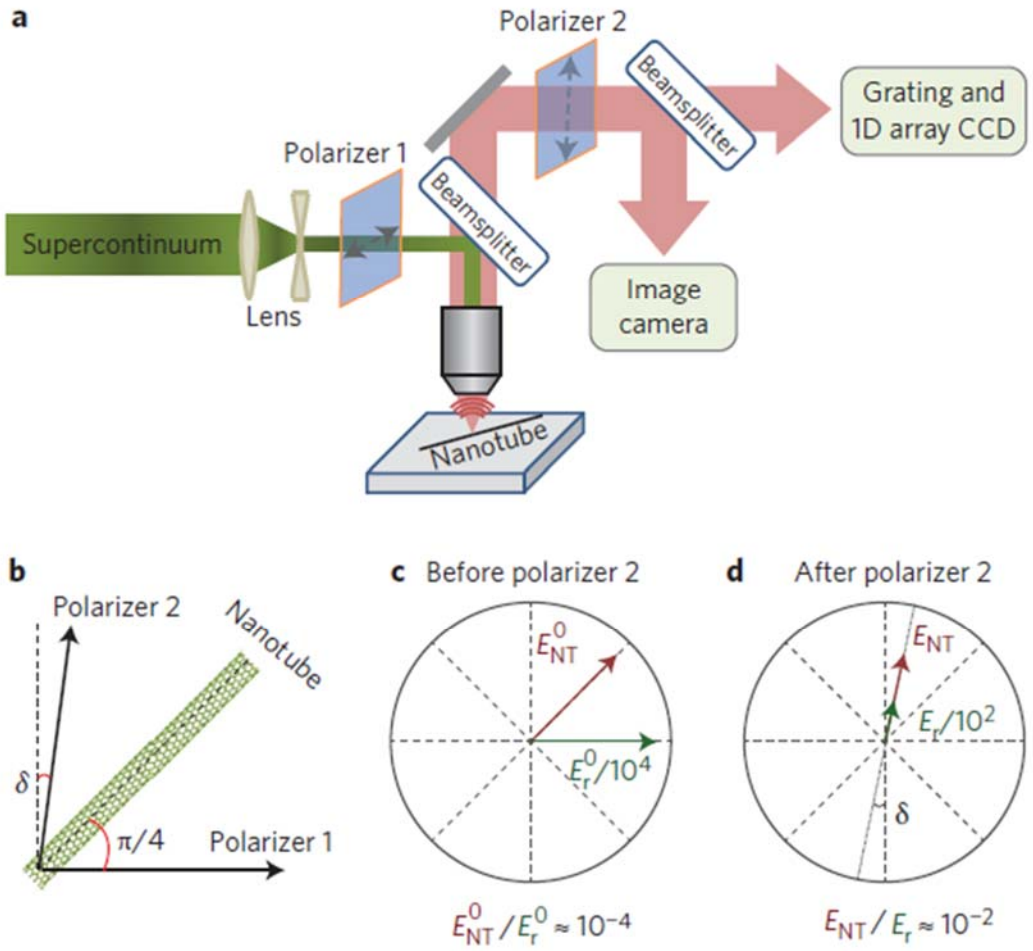

Figure 4-3 Scheme of polarization-based optical microscopy for single-nanotube imaging and spectroscopy. (a) Combination of supercontinuum laser illumination and high-contrast polarization microscopy for high-throughput individual nanotube imaging and chirality identification. P1 and P2: polarizers; BS: beamsplitter. (b) Configuration of the incident polarizer P1, outgoing polarizer P2, and the carbon nanotube. (c-d) Illustration of electrical field polarization before (c) and after (d) polarizer P2. Dramatic reduction of the reflection electrical field leads to an enhancement of nanotube optical contrast by ~ 1/(sinδ), where is the deviation angle of P2 from perpendicular direction.

The most important development in this setup is separate optimization of effective NA for nanotube illumination and imaging. A major challenge in polarization microscopy is that light going through a large NA objective gets strongly depolarized due to polarization-dependent reflection at oblique incidence (*67*). On the other hand, large NA objective is crucial for high spatial-resolution imaging of nanotubes. Therefore high polarization purity

and high spatial resolution seem to be two contradictory requirements. In our experiment we realize that high polarization extinction is only required for reflected light, while spatial resolution can be maintained by collecting nanotube scattered light with large NA. This allows us to satisfy the two requirements simultaneously. Specifically, we use an objective with a large NA (=0.8), which collects nanotube scattered light with full NA to obtain a high spatial resolution. On the other hand, we control the illumination light to have a much smaller "effective NA" by using incident beam with diameter much smaller than the objective back aperture, as illustrated in Figure 4-3a. Here the incident and reflected light only go through the center of the objective and suffer little from polarization degradation due to oblique incidence. This special illumination scheme exploits the highly collimated beam of a supercontinuum light source, and it is critical for achieving high polarization purity and spatial resolution simultaneously in single-tube imaging and spectroscopy. It is also critical to maintain the high polarization purity and a flat spectral response by careful selection of broadband and birefringence-free optical components. This includes using minimal number of components between the two polarizers, and minimizing strain for the necessary beamsplitter and objective.

In addition, we exploit several other unique aspects of the supercontinuum laser for the high throughput imaging and spectroscopy of single nanotubes: The low coherence of the supercontinuum eliminates interferences and speckles typical for single-wavelength laser illumination; the high brightness of supercontinuum ensures a large optical signal even after high extinction from polarization control; and the broadband light source enables a single-shot measurement of the whole spectrum.

4.2.2 Result

Our technique enables direct imaging of single nanotubes in diverse configurations, as schematically illustrated in Figure 4-4a-c. Figure 2d-f show corresponding scanning electron micrographs, with a nanotube on a fused silica substrate (20d), a nanotube in a back-gated field-effect transistor with source-drain electrodes (20e), and a nanotube partly covered by an Al_2O_3 dielectric layer (20f). Now we are able to image such individual nanotubes directly using optical microscopy (Figure 4-4g-i) rather than electron microscopy. A single-walled nanotube typically has a contrast larger than 5% in our optical microscopic images. More importantly, we can not only "see" individual nanotubes, but also obtain their optical spectra and uniquely identify their chiralities. Figure 4-4j-l display the spectra of nanotubes shown in Figure 4-4g-i. Each spectrum is obtained within 2 seconds using the broadband supercontinuum illumination and a spectrometer equipped with a linear array charge coupled device (CCD). From the prominent optical resonances in the spectra, we can assign the chirality (20,6), (22,16), and (26,22) to these three single-

walled nanotubes (*61*). They are semiconducting, metallic and semiconducting nanotubes with diameters of 1.8, 2.6 and 3.3 nm, respectively.

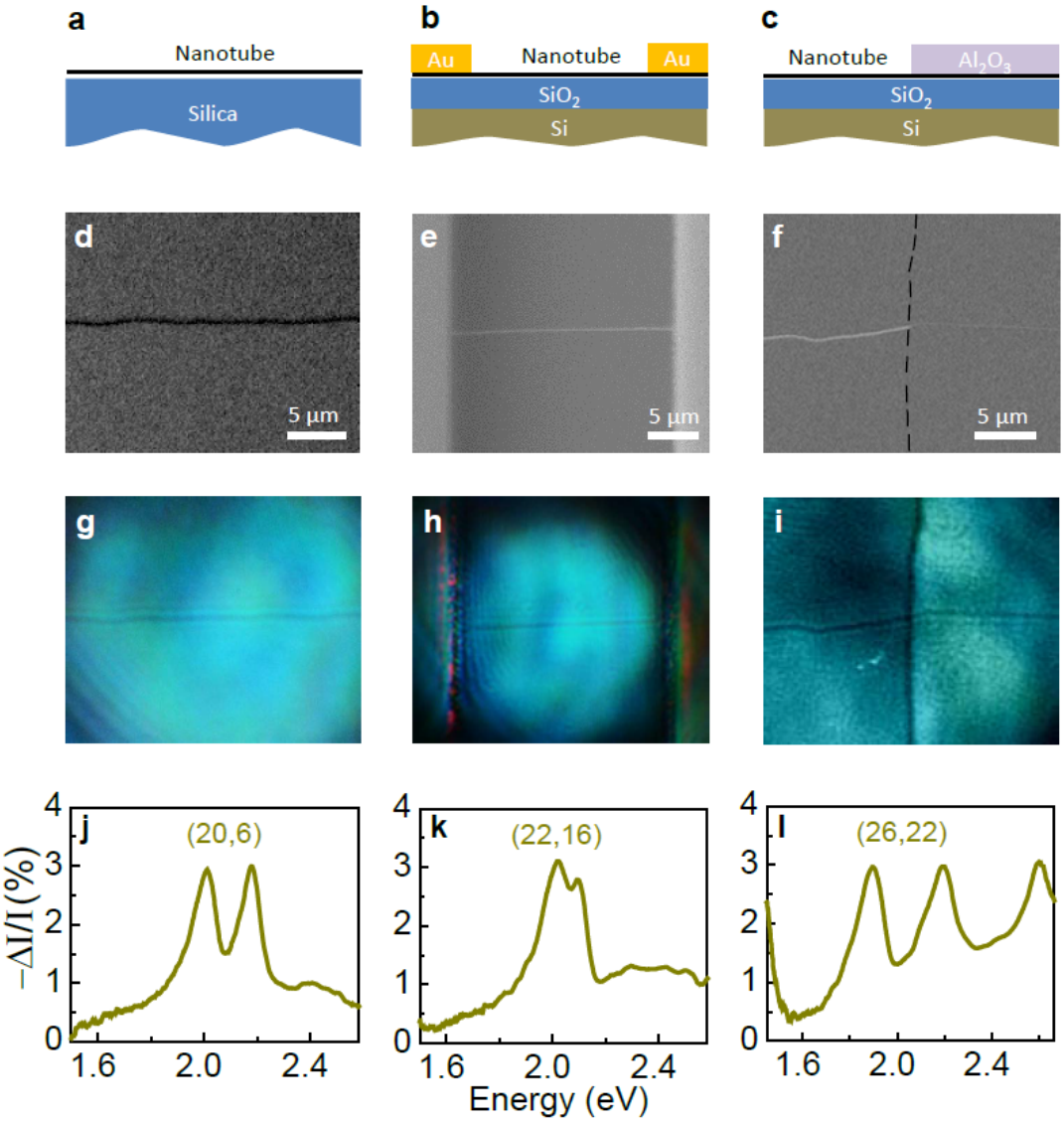

Figure 4-4 Optical imaging and spectroscopy of individual nanotube on substrates and in devices. (a-c) Schematic drawing of a nanotube on fused silica substrate, a nanotube in a back-gated field-effect transistor device (with two gold electrodes), and a nanotube partly under Al_2O_3 dielectric layer. (**d-f**) Scanning electron microscopic (SEM) images of the nanotubes corresponding to a-c. The dashed line in f traces the invisible Al_2O_3 edge. (**g-i**) Direct optical images of individual nanotubes in d-f using a colour camera with an integration time of ~ 20 ms. Optical images show high contrast for all individual nanotubes. (**j-l**) Optical spectra of the nanotubes in g-i, from which we identify the three nanotubes with chirality of (20,6), (22,16), and (26,22). They are semiconducting, metallic and semiconducting nanotubes with diameters of 1.8, 2.6 and 3.3 nm, respectively.

4.2.3 Application I - Chirality Profiling of As-grown Samples

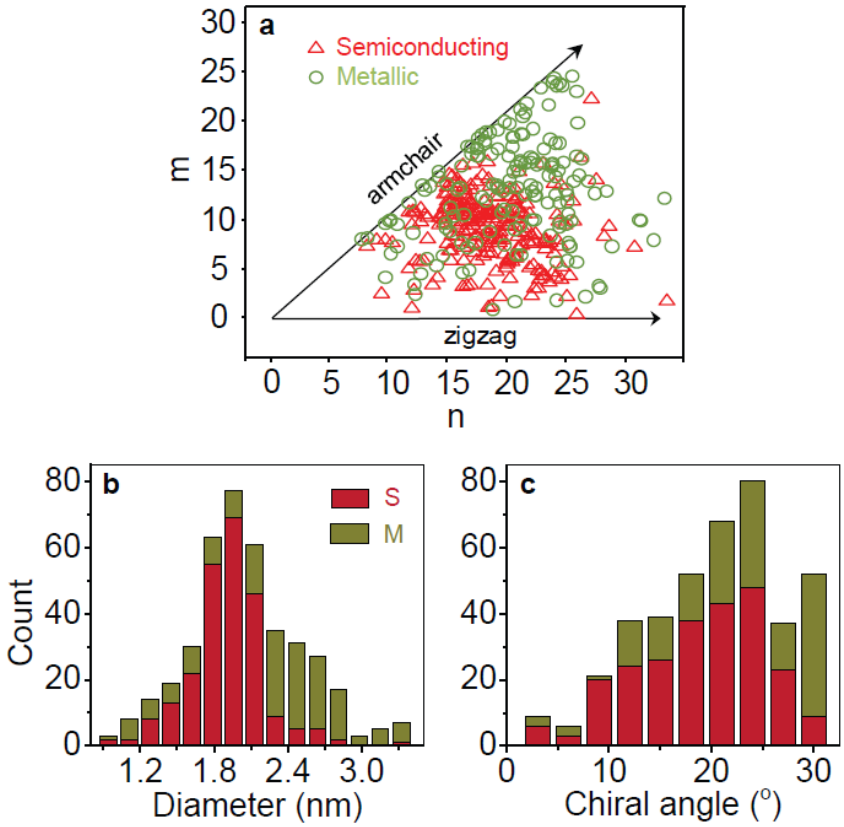

Figure 4-5 High-throughput chirality profiling of 402 single-walled carbon nanotubes from one growth condition. (a) Chiral index distribution of semiconducting (red triangles) and metallic nanotubes (dark green circles) which show enrichment in different n-m region. **(b)** Diameter distribution of semiconducting (S: red bars) and metallic nanotubes (M: dark yellow bars). They reveal a surprising correlation: semiconducting species are highly enriched for nanotube diameter between 1.7-2.1 nm, while metallic species dominate for tube diameter larger than 2.3 nm. (**c**) Chiral angle distribution of semiconducting and metallic nanotubes.

Such high-throughput imaging and chirality identification of nanotubes on substrates could be an indispensable tool for improving carbon nanotube growth, because it enables a systematic optimization of nanotube growth conditions. This component has been so far missing because there has been no simple and reliable way to accurately determine nanotube chirality and abundance at the same time (except for a rough diameter distribution using resonant Raman measurement (*68*)). In Figure 4-5 we plot the chirality of over 400 single-walled nanotubes from one growth condition, which includes 240 semiconducting nanotubes (S) and 162 metallic nanotubes (M). Now the detailed chirality distribution of hundreds of nanotubes on as-grown substrates (transparent or opaque) can be accurately determined. The chirality distribution in Figure 4-5a shows that in the specific sample semiconducting and metallic nanotubes are enriched in different region with characteristic chiral angle and diameter dependence. The chiral angle distribution (Figure 4-5c) shows

that large chiral angles (close to the armchair direction) are more favorable, consistent with previous findings (*69*). The diameter distribution (Figure 4-5b), however, is quite surprising. It reveals a strong correlation between the diameter and a nanotube being semiconducting or metallic. With random distribution of chirality, one expects a ratio of 2:1 for semiconducting and metallic nanotubes. However, we observe that for nanotube diameter between 1.7-2.1 nm, semiconducting species are highly enriched, while metallic ones completely dominate for nanotube diameter larger than 2.3 nm. This unusual correlation behavior can only be revealed with our capability to map all individual nanotube chirality on substrates. In comparison, previous Raman characterization and electrical measurements only shows an overall enrichment of semiconducting nanotubes in this growth condition without observing any diameter-metallicity correlation (*70*), because Raman scattering selectively probes only nanotube species in resonance with the excitation laser and can miss the full picture. The accurate and complete characterization of as-grown nanotube species enabled by our technique will be crucial for better understanding of the growth mechanisms and systematic growth optimization.

4.2.4 Application II - Characterization of Functioning Devices

In-situ imaging and spectroscopy of individual nanotubes also offer new opportunities to probe nanotube physics in operating devices. Here we examine gate-variable nanotube optical transitions in field-effect devices (Figure 4-4b) to investigate electron-electron interaction effects on excited states in nanotubes.

Figure 4-6a and 22b display gate-dependent optical spectra for an (18, 18) metallic nanotube and a (26, 10) semiconducting nanotube, respectively. The resonance peak in metallic (18, 18) nanotube arise from M_{22} transitions, and the peaks in semiconducting (26, 10) are from S_{44} and S_{55} transitions. All these optical resonances show significant broadening with gate voltage varying from close to 0V to -30V, which corresponds to a nanotube doping from the charge neutral point to a hole density of ~ 0.45 e/nm (based on calibration using G-mode Raman resonance in metallic nanotubes (*71*)). At such doping levels, free holes partially fill the linear band of metallic nanotubes or the first subband of semiconducting nanotubes. Therefore the broadening of higher-band optical transition cannot be accounted by Pauli blocking that dominates semiconducting nanotube fluorescence or graphene absorption (*72*, *73*). Instead, it originates from many-body interactions between doped carriers and excitons in carbon nanotubes.

Electron-electron interactions can be greatly enhanced in one dimension. Two types of interactions between doped carriers and excitons were well known to affect excitonic resonances in nanotubes: dielectric screening (*58*, *74*) and formation of trion states (*75*). Trions will lead to a new optical resonance (*75*), which we do not observe in the higher subband transitions. Dielectric screening of the nanotube exciton is expected to shift the exciton transitions with little increase in the optical linewidth (*58*) and previous Raman studies suggest that this dielectric screening dominates gate-induced redshift on excitonic transitions (*74*). In our experiment, we do observe a small redshift in most exciton transitions, presumably due to the screening effect. However, the more obvious gate-induced effect is a broadening of exciton resonance linewidth. The linewidth broadening

from the dielectric screening is expected to be less than 15 meV. Experimentally we observed a gate-induced broadening of more than 50 meV. This large broadening beyond the dielectric screening effect cannot be accounted for by established mechanisms. Because inhomogeneous broadening in single-tube spectra is small, the resonance width can be directly related to the ultrafast dynamics of an excited state. The observed gate-induced broadening cannot be from a change in dephasing due to exciton-phonon coupling, because electrical gating mainly introduces free carrier doping with little effect on exicton-phonon interactions. It indicates that a new type of electron-exciton interaction is critically important.

Here we propose that inter-subband scattering between the exciton and gate-induced free carriers (Fig. 22c-f) could be responsible for the ultrafast dephasing of exciton through population decay. This electron-electron scattering is an Auger-type process, and it is strongly constrained in one-dimensional carbon nanotube by the conservation of energy, momentum, and angular momentum (described by the quantum number E, k, and band index μ, respectively). Figure 4-6d (22f) shows one representative scattering channel that satisfies the stringent conservation requirements in hole doped metallic (semiconducting) nanotubes. Such scattering between optically excited electron and free holes (in another valley) is absent in pristine undoped carbon nanotube (Figure 4-6c and 22e), and emerges with hole doping (Figure 4-6d and 22f). (Excitonic correlation between the excited electron and hole, not shown in the illustration for simplicity, should not change the picture qualitatively.) This inter-subband electron-electron scattering rate increases with the free carrier concentration, and can dominate ultrafast relaxation of the exciton state at high doping.

It is interesting to note that carbon nanotube provides a unique opportunity to probe different ultrafast processes in graphitic materials, which share similar electronic structures and dynamic responses. Unlike graphene, the well-defined exciton resonances in nanotubes allow one to estimate the ultrafast excited state dynamics from resonance widths using Heisenberg uncertainty principle. In addition, the stringent constraint from energy, momentum, and angular momentum conservation means that excitons can relax only through electron-phonon interactions in undoped nanotubes, and allows us to isolate its contribution to ultrafast dynamics. On the other hand, gate dependence probes selectively the exciton relaxation through electron-electron interactions. Take the M_{22} transition in (18, 18) nanotube for an example. We can isolate a dephasing rate of ~ $(5\ \text{fs})^{-1}$ from exciton-phonon coupling and a decay rate of ~ $(10\ \text{fs})^{-1}$ from exciton-electron coupling at doping level of ~0.45 e/nm. Such knowledge on ultrafast relaxation will be important for optoelectronic applications employing hot electrons in carbon nanotube and graphene(*76*).

4.2.5 Phase Considerations in Reflection Measurements on SiO_2/Si

SiO_2/Si substrate is the most common substrate in device applications and carbon nanotubes on top of this substrate is readily made field effect transistors. It is therefore crucial that we understand the optical properties of carbon nanotube on this substrate, especially the pure absorption spectrum (imaginary part of dielectric constant), which is to be compared to theory. However the multilayer reflection poses a challenge to this goal.

The nanotube scattered field would experience a complex local field and the substrate reflected field acquires additional wavelength-dependent phase. As a result the optical spectrum becomes a combination of real part and imaginary part of susceptibility. We would like to restore the pure absorption spectrum from measured reflection contrast spectrum.

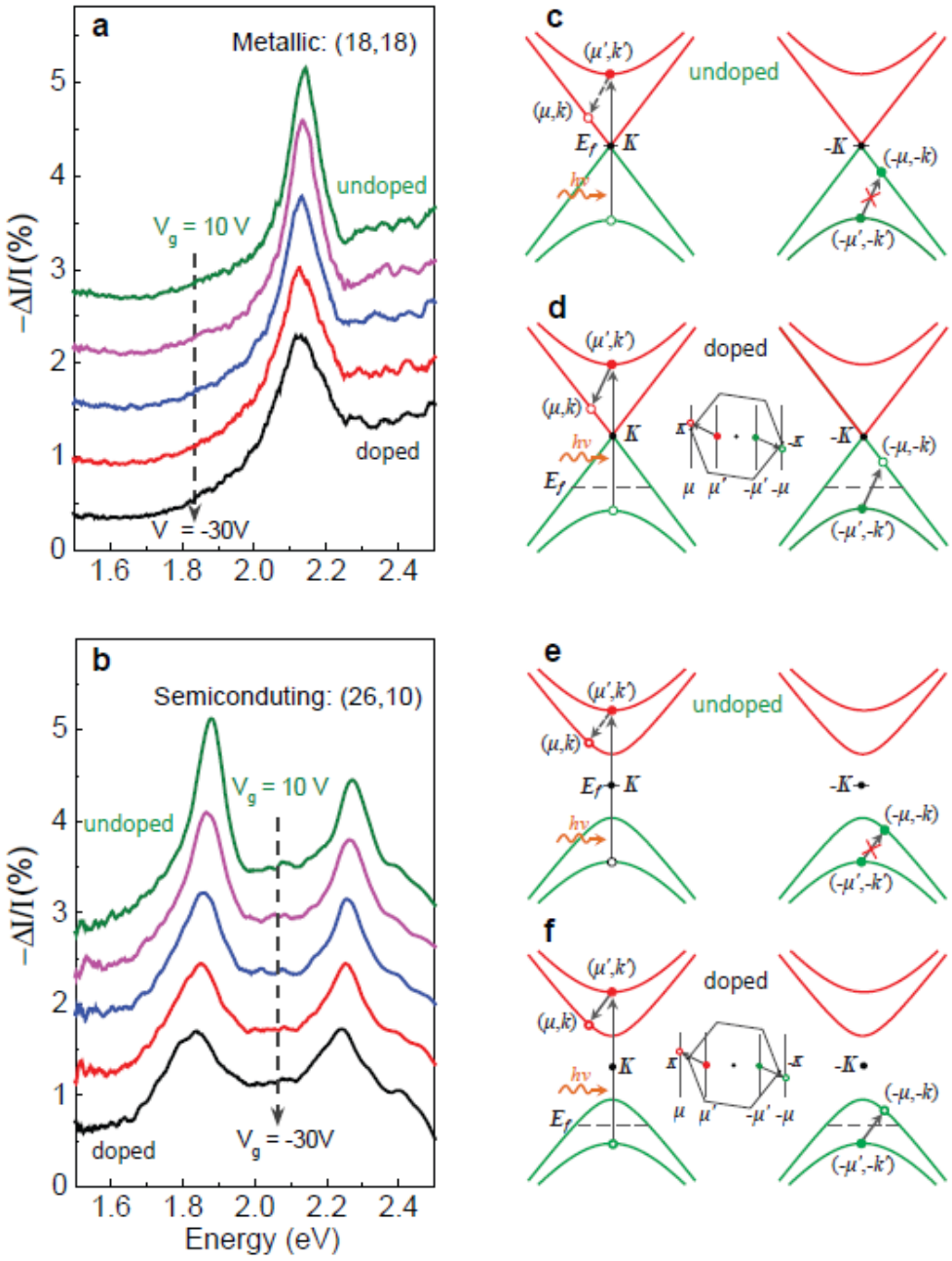

Figure 4-6 Gate-variable nanotube optical transitions in field-effect devices. (a)(b) Optical spectral evolution of a metallic (18, 18) (a) and a semiconducting (26, 10) nanotube (b) under different back-gated voltages. A significant broadening was observed for all transition from Vg= ~ 0V to Vg=-30V, which correspond to changes from undoped state

to hole doping of ~0.45 e/nm. At this doping level, free holes partially fill the linear band of metallic nanotubes or the first subband of semiconducting nanotubes. (c-f) Schematic illustration of one representative ultrafast decay pathway of the optically excited electron due to inter-subband electron-electron scattering in doped metallic (d) and semiconducting (f) nanotubes. The photo-excited electron decays to a state in a lower subband and transfers its energy, momentum and angular momentum to a free hole in the other valley. This process requires a free hole to participate, and it is forbidden for undoped nanotubes (c and e) but allowed for doped ones (d and f). The insets in d and f depict the process in two-dimensional grapheme Brillouin zone, where the vertical lines correspond to nanotube subbands (their distance is exaggerated for better vision). It shows that energy, momentum and angular momentum are conserved in this inter-subband electron-electron scattering.

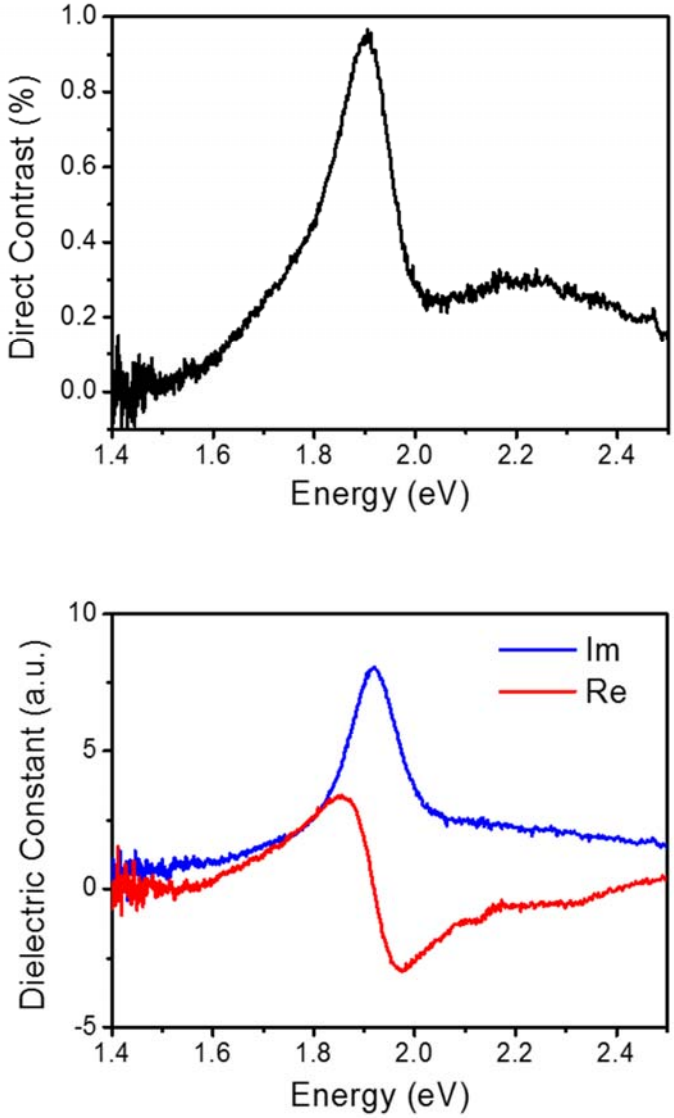

Figure 4-7 Extracting real and imaginary part of dielectric constant from contrast measurements. a. Direct contrast measurements. **b.** extracted real and imaginary part with the help of a quarter wave plate.

As we have shown in Eq. 4-6, the contrast of the nanotube can be written as an interference between nanotube scattered electric field and local oscillator field (from the unperturbed incident field)

$$\boldsymbol{E_{LO} = E_0 r sin(\delta) e^{-i\pi/2}, E_{NT} \sim E_0 (1+r)^2 \cdot \sin^2\left(\frac{\pi}{4}\right) \cdot \chi}$$
$$\frac{\Delta \boldsymbol{I}}{\boldsymbol{I}} = \frac{2\mathrm{Im}(\boldsymbol{E_{NT} E_{LO}^*})}{|\boldsymbol{E_{LO}}|^2} \sim \mathrm{Im}(\boldsymbol{\sigma\chi}) \qquad \text{Eq. 4-8}$$

Here δ is the angle deviation from the cross-polarization and $\frac{\pi}{4}$ is the angle between nanotube orientation and both polarizers. r is the reflection coefficient calculated from Fresnel equations and $(1+r)$ is the local field experienced by the nanotube. This local field factor accounts for both excitation and radiation and hence been squared. σ represents the combined coefficient and is a complex number. Therefore the obtained $\frac{\Delta I}{I}$ would give mixed information of real part and imaginary part of χ. Another equation would be needed to determine the pure imaginary part or real part of χ.

The other equation can be readily available if we set P2 strictly cross with P1 and put a quarter wave plate after P1. The quarter wave plate is set with the fast axis mostly parallel to P1 but with a small deviation from P1 so that P2 will have a small transmission (1%) from the slow axis. Therefore the field after the quarter wave plate will have the majority component still parallel to the P1 (same phase as before), which will excite the nanotube. The nanotube field expression is still the same. However the local oscillator field transmitted through P2 will have phase shifted by $\frac{\pi}{2}$ as required by the physical principles of quarter wave plate. Therefore we can write

$$\boldsymbol{E_{LO} = E_0 r sin(\delta), E_{NT} \sim E_0 (1+r)^2 \cdot \sin^2\left(\frac{\pi}{4}\right) \cdot \chi}$$
$$\frac{\Delta \boldsymbol{I}}{\boldsymbol{I}} = \frac{2\mathrm{Im}(\boldsymbol{E_{NT} E_{LO}^*})}{|\boldsymbol{E_{LO}}|^2} \sim \mathrm{Re}(\boldsymbol{\sigma\chi}) \qquad \text{Eq. 4-9}$$

This two equation combined gives us a way to find out the exact absorption of nanotube even it is on a SiO_2/Si. Figure 4-7a shows the spectrum from direct contrast measurements for nanotube (21, 21) on 90 nm SiO_2/Si. The resonant peak is non-symmetric and there is a slow bump around 2.2 eV due to the mixing of real part of dielectric constant. After we performed the complimentary measurement with quarter wave plate we could obtain the absorption of this nanotube (imaginary part of dielectric constant, Figure 4-7b), and is now much Lorentzian like, an indication of an excitonic absorption. The bump is gone but a small decaying background is present signifying the band to band transition, which is consistent with pure absorption measurements. (See next section)

4.3 Absolute Absorption of Individual Carbon Nanotube Through Transmission Microscope

4.3.1 Absorption Measurement setup

Quantitative information of SWNT absorption cross-section is highly desirable for understanding nanotube electronic structures, for evaluating quantum efficiency of nanotube photoluminescence (*69*, *77*) and photocurrent (*78–80*), and for investigating the unique many-body effects in 1D systems (*55*, *61*, *81–85*). In order to measure accurately the absolute absorption cross-section of known Chiralities, we performed the same polarization measurement with a transmission geometry with nanotube suspended slits (*86*). There are two reasons we choose nanotube on slits. First it does not involve complicated phases and local fields, which simplifies the analysis and increase accuracy. Second, it is readily characterized by electron diffraction, one of the most accurate ways to determine the chirality of nanotubes.

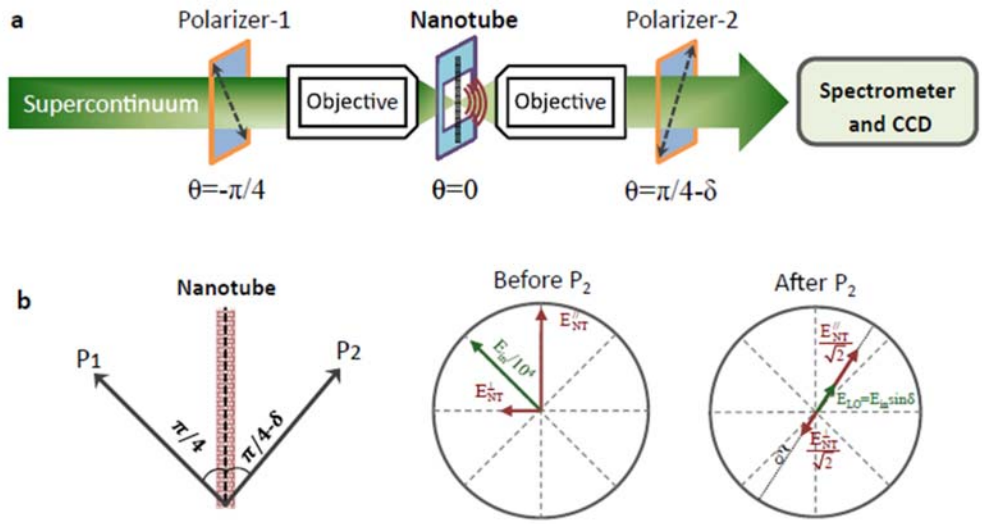

Figure 4-8 Scheme of polarization-optimized homodyne detection for single-nanotube absorption. (a) Two nearly-crossed polarizers (with a small deviation angle δ) were used to control the incident and outgoing light polarization, and two polarization-maintaining objectives were placed confocally between this polarizer pair. Suspended individual nanotubes were positioned at the focus of the objectives and with an angle of π/4 with respect to the first polarizer polarization. We use broadband supercontinuum laser (spectral range 450-850 nm) as the light source and a spectrometer equipped with a silicon linear array for fast wide-spectral detection. (**b)** Interference between E_{in} and E_{NT} after the nanotube gives rise to nanotube extinction, while interference between E_s ($\approx(E_{NT}^{//}-E_{NT}^{\perp})/\sqrt{2}$) and E_{LO} ($=E_{in}\sin\delta$) after polarizer-2 generates the final homodyne signal. Given that $E_{LO}:E_{in}\sim10^{-2}$ and $E_s:E_{NT}\sim1/\sqrt{2}$ with suitable polarizer setting, the enhanced homodyne modulation signal ΔI/I can be two orders of magnitude higher than the transmission change ΔT/T It enables high sensitivity measurements of nanotube absorption . The δ angle is exaggerated for better visualization.

The transmission geometry measurement is depicted in Figure 4-8. Two nearly-crossed polarizers (with a small deviation angle δ) were used to control the incident and outgoing light polarization, and two polarization-maintaining objectives were placed confocally between this polarizer pair. Suspended individual nanotubes were positioned at the focus of the objectives and with an angle of 45 degrees with respect to the first polarizer. With this polarization control, we can obtain the polarization-dependent nanotube absorption through the enhanced homodyne optical contrast directly using

$$-\frac{\Delta I}{I}(\delta) = \frac{\alpha_{//} - \alpha_{\perp}}{2}\mathrm{ctg}(\delta) + \frac{\alpha_{//} + \alpha_{\perp}}{2} \qquad \text{Eq. 4-10}$$

where $\alpha_{//}$ and $\alpha_{\perp}$ are nanotube absorption constants for light polarized parallel and perpendicular to the nanotube axis, respectively. Here $(\alpha_{//} - \alpha_{\perp})/2$ characterizes the strong depolarization effect of nanotubes. It gives rise to a greatly enhanced optical contrast I/I at small which can reach ~ 1% (compared to 10^{-4} in conventional transmission change) and becomes easily detectable.

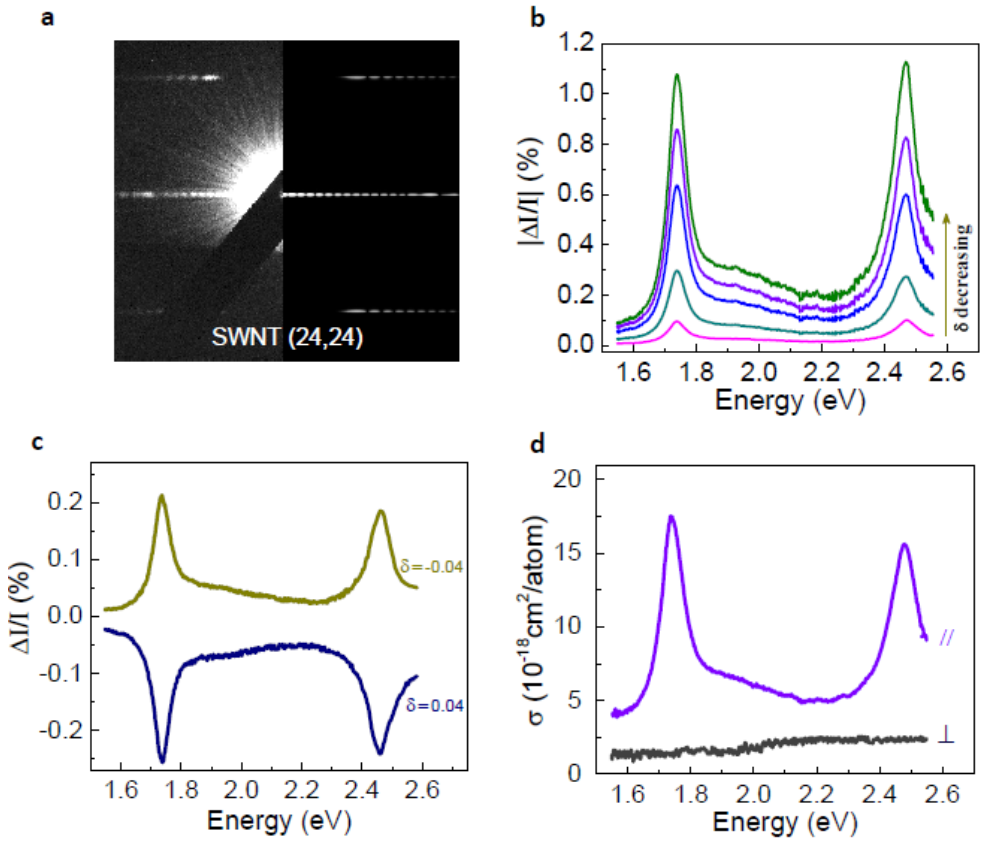

Figure 4-9 Representative data for polarization-optimized homodyne detection of single-nanotube absorption. (a) Electron diffraction patterns (left half: experimental, right half: simulated) uniquely determine the chiral index of this nanotube as (24, 24). The

black diagonal feature in the experimental pattern is from the blocking stick inside the TEM for dark-field imaging. (b) Homodyne modulation signal (|ΔI/I|) at various values of δ as in Fig. 1a. With δ decreasing from 5 to 0.5 degrees, the signal at resonances gradually increases to 1% level. (c) Modulation signal at δ = ±0.04. It shows interference signature that when δ crosses zero, local oscillator ELO changes sign and so does the homodyne interference modulation ΔI/I. (d) The absolute absorption cross-section per carbon atom with both parallel (//) and perpendicular (⊥) light polarization to nanotube axis. The $\sigma_{//}$ spectrum shows clear resonance peaks corresponding to the exciton transitions; while $\sigma_{\perp}$ is mostly featureless. For all studied SWNTs, $\sigma_{\perp}$ has an integrated absorption between 1/5 and 1/3 of that in $\sigma_{//}$ due to depolarization effect in 1D nanotubes.

The power of our technique is demonstrated in Figure 4-9, which displays ΔI/I spectra from a SWNT using different polarization settings. The chiral index of this nanotube was independently determined as (24,24) from its electron diffraction pattern (Figure 4-9a). By gradually decreasing δ (the deviation angle from the crossed polarizer position as labeled in Fig. 1a) from 5º to 0.5º, the resulting modulation signal |ΔI/I| increases steadily to 1% level at peak positions (Fig. 25b). Figure 4-9c further shows that when δ crosses zero, the local oscillator E_{LO} changes sign, and so does the homodyne interference modulation ΔI/I. This new polarization scheme, coupled with supercontinnum illumination and array detections, enables us to obtain single-nanotube ΔI/I spectra across a wide spectral range in a few seconds, orders of magnitude faster than previous approaches (*55–57*).

4.3.2 Determination of Absorption Coefficient in Both Polarizations

The spectra of ΔI/I as a function of δ allow direct determination of both $\alpha_{//}$ and $\alpha_{\perp}$. Nanotube absorption cross-sections are proportional to $\alpha_{//}$ and $\alpha_{\perp}$, and their absolute values can be obtained once the illumination beam size is known. We determine the focused supercontinnum beam profile at high accuracy by systematically measuring the absorption spectra with nanotubes at different positions in the focused beam. With this information, we obtained spectra of optical absorption cross-sections per atom along both parallel (//) and perpendicular (⊥) polarizations for the (24,24) SWNT, which is displayed in Figure 4-9d. We performed such absorption measurements on 57 chirality identified SWNTs, and it allows us to systematically examine polarization dependent absorption cross-section in different nanotube species for the first time. The // spectra show prominent and different exciton transition peaks in different nanotubes. These chirality-dependent exciton transitions provide rich information on chirality-dependent nanotube photophysics, as we will describe later. The ⊥ spectra, on the other hand, show a small and finite perpendicular absorption (~ 1/5 of the average // value) and they are largely featureless.

We first examine briefly the ⊥ spectra, which have never been probed at single nanotube level before. The small magnitude of ⊥ can be attributed to depolarization effects (*87–90*), but its lack of any resonance features is surprising at the first look. It is widely known that perpendicularly polarized light can excite transitions between adjacent cutting lines due to angular momentum selection rule. One naturally expects resonance features associated with these exciton transitions in ⊥ spectra. Indeed prominent absorption peak corresponding to S_{12} and S_{21} transitions have been observed in

semiconducting nanotubes with perpendicular polarization excitation (*77*). However, here we do not observe any resonances in our $_{\perp}$ spectra, where transitions between higher sub-bands are probed. Detailed theoretical analysis shows that although transitions between adjacent cutting lines are symmetry allowed, their matrix elements are always zero close to the bandgap since they fail to conserve pseudospin, except for the S_{12} and S_{21} transitions (*91*). This matrix element effect strongly suppresses exciton transition (as well as van Hove singularity at the bandedge), resulting in no spectral resonances for higher order transitions under perpendicularly polarized light. Away from the bandedge, the transition matrix element becomes finite and results in the finite but largely featureless $_{\perp}$, as we observe experimentally.

4.3.3 Systematic Analysis of Absorption Cross Section in Parallel Polarization

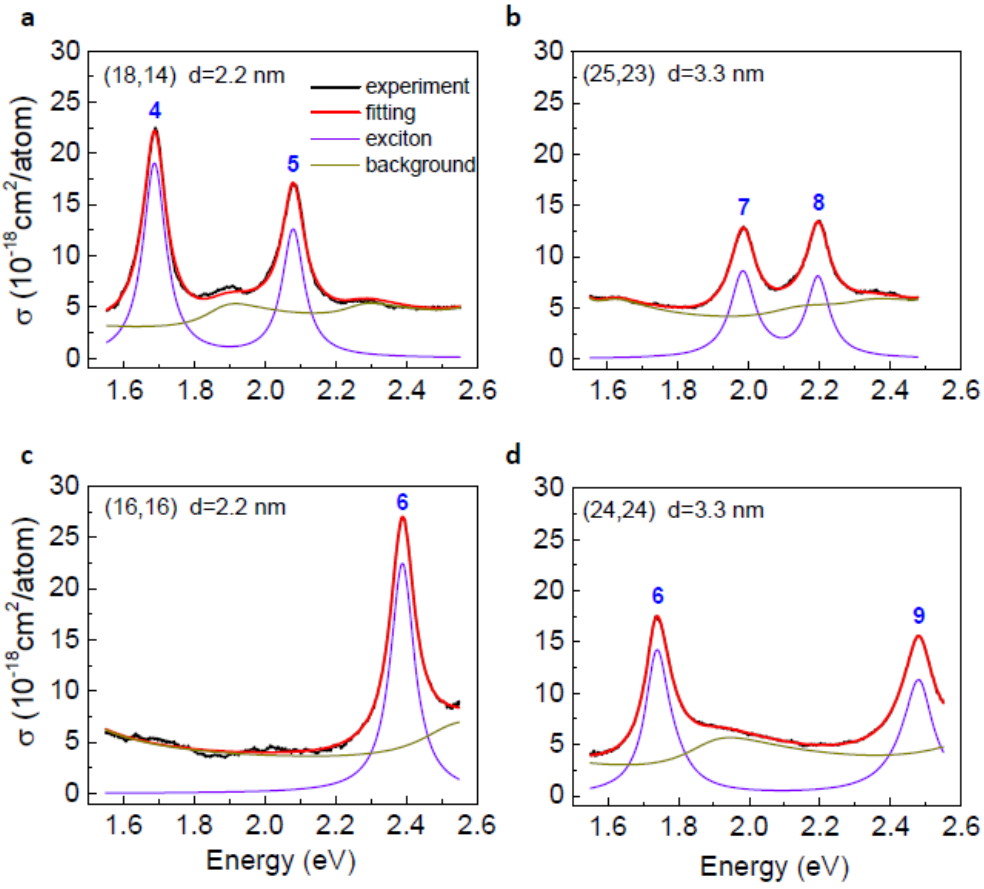

Figure 4-10 Representative absorption cross-section spectra of four nanotubes. (**a**) semiconducting (18,14). (**b**) semiconducting (25,23). (**c**) metallic (16,16). (**d**) metallic (24,24). Black, red, violet and dark yellow lines are experimental data, phenomenological fitted total absorption, exciton component, and continuum component, respectively. The integer number p at each peak indexes the optical transition type as described in the text. The resonant peaks show symmetric shape and reveal the exciton nature of nanotube

optical transitions; while an obvious continuum background exists. The phenomenological model described in the text reproduces the absorption spectra nicely. The exciton transition energy, oscillator strengths, and linewidth vary significantly with the nanotube species and transition index p.

Below we will focus on // spectra in chirality defined SWNTs. Figure 4-10a-d display four representative parallel-polarization spectra (black lines) in semiconducting (18,14), (25,23) and metallic (16,16), (24,24) nanotubes, where the chiral indices were independently determined by the electron diffraction techniques. All // spectra in Figure 4-10 are characterized by sharp optical resonances arising from excitonic transitions and a broad continuum background. They provide a wealth of information on the unique nanotube photophysics.

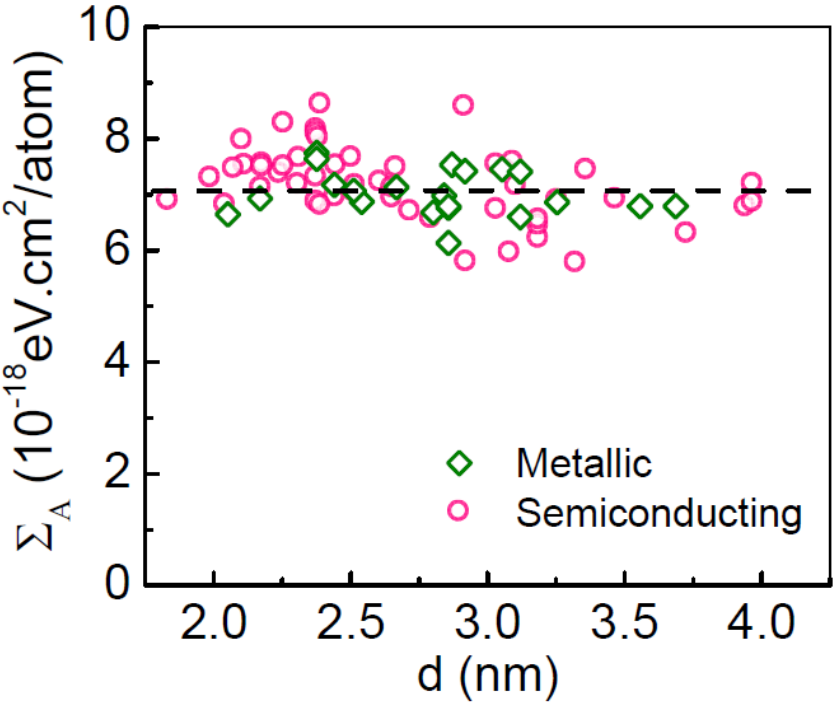

Figure 4-11 Integrated absorption cross-section in the energy range of 1.55 to 2.48 eV. All the data converge to the value of graphene integrated over the same energy region (dashed line). This convergence originates from an approximated f-sum rule.

We first note that for all nanotubes, the average absorption cross-section is ~ 7.6×10^{-18} cm^2/atom. This corresponds to an integrated cross-section (Σ_A) of 7.1×10^{-18} eV·cm^2/atom between the spectral range 1.55 to 2.48 eV, the same as Σ_A of graphene in the same range (*92*, *93*). Figure 4-11 shows in detail the distribution of Σ_A in different nanotubes (dots), which converges on the graphene value (dashed line). The physical origin for this convergence is an approximated f-sum rule, where the integrated oscillator strength per atom over a sufficiently large spectral range should be the same for all graphitic structures. The agreement between nanotubes and graphene values provides an independent confirmation of the accuracy of our nanotube absorption cross-section results. (The slight

variation in nanotube values is presumably due to the different distribution of resonant peaks in different nanotubes and the finite integrated energy range.)

4.3.4 Chirality and Transition Dependent Exciton Oscillator Strength

To quantitatively describe the chirality dependent absorption features in different nanotubes, we introduce a phenomenological model composed of a discrete exciton peak and corresponding continuum absorption for each subband. The exciton transitions are Lorentzian resonances, each characterized by its resonance energy E_p, resonance width Δ_p, and oscillator strength (integrated cross-section) Σ_p. Here p is an integer indexing optical transitions of both semiconducting (S_{ii}) and metallic nanotubes (M_{ii}) starting from 1 in the order of S_{11}, S_{22}, M_{11}, S_{33}, S_{44}, M_{22}, S_{55}, S_{66}, M_{33}, S_{77},… The "continuum" absorption, including the contribution from band-to-band transitions as well as phonon sidebands and higher-order exciton transitions, is approximated empirically by a Lorentzian broadened form of the function $\Theta[E-(E_p+\Delta_p)]\times(1/\sqrt{E-(E_p+\Delta_p)})$. Here Θ is the heavyside step function, Δ_p is the offset of continuum edge relative to the exciton transition, and the second term models the 1D density of states close to the band edge. Red lines in Figure 4-10 show that our phenomenological model nicely reproduces the experimental absorption spectra, with violet and dark yellow lines showing the exciton and continuum contribution, respectively. We note that the continuum absorption constitutes a significant portion of the total nanotube absorption oscillator strength, which has never been appreciated previously. The relative importance of continuum absorption increases with the nanotube diameter and the transition index p.

Exciton resonances, the most prominent features in the absorption spectra, encode rich 1D nanotube physics in their chirality dependent behavior. (1) The exciton absorption oscillator strength provides new information on electron-hole interaction strength in the 1D nanotubes. (2) The exciton transition linewidth, arising from the finite exciton lifetime, reveals the ultrafast relaxation dynamics of excited states. (3) The exciton transition energies and their dependence on nanotube species observed in absorption spectra here provide a valuable confirmation of the recent assignment established using Rayleigh scattering spectroscopy[16] with an accuracy of 10 meV.

The exciton takes its oscillator strength from band-to-band transitions due to the electron-hole correlation(*55*, *83–85*). Its value depends on both the interband optical transition matrix element and the exciton wavefunction at zero electron-hole separation. We observe in the experimental spectra (Figure 4-10) that the exciton oscillator strength decreases significantly in large diameter nanotubes. A systematic examination reveals that the tube-dependent exciton oscillator strength can be described by a universal scaling law, $\Sigma_p \sim \frac{1}{(p+7.5)d}$ as displayed in Figure 4-11a. For semiconducting nanotubes, this scaling law can be understood theoretically using a model description of the excitonic effects, and the magnitude of observed exciton oscillator strengths agrees well with our theoretical predictions (*94*).

Figure 4-11a also shows that the exciton oscillator strengths in metallic (diamonds) and semiconducting (circles) nanotubes have similar magnitude and fall on the same curve. This behavior appears surprising, because the electron-hole interactions are expected to be much weaker in metallic nanotubes due to free electron screening. Naively the resulting exciton transition should have significantly smaller oscillator strength. Previous *ab initio* calculations (*83*, *84*), however, showed that the oscillator strength from excitons in metallic nanotubes are comparable to those in semiconducting tube, although no systematic analysis was carried out. Further effort will be required to understand quantitatively the experimental data here, and it could lead to deeper insight into many-body interactions in 1D nanotubes.

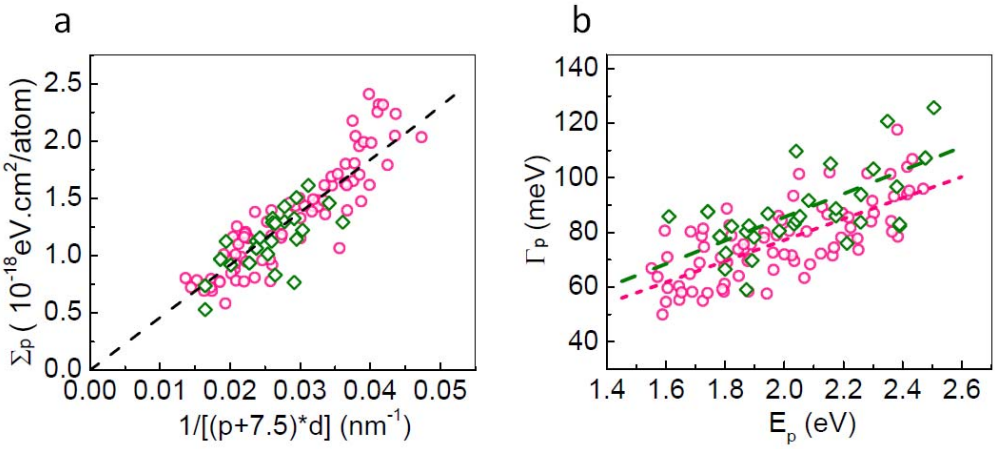

Figure 4-12 Tube-dependent exciton oscillator strength and transition linewidth in 57 SWNTs. The diamonds and the circles represent data from 18 metallic and 39 semiconducting nanotubes, respectively. **a.** Tube-dependent exciton oscillator strength is described by a universal scaling law of $4.6 \times 10^{-24}/[(p+7.5)\cdot d]$ eVcm^3/atom (dashed line), where d is nanotube diameter and p is transition order indexing both semiconducting and metallic nanotube optical transitions. Metallic and semiconducting nanotubes, surprisingly, exhibit similar exciton oscillator strength, although they are characterized by significantly different electron-hole interactions. **b.** Exciton transition linewidth in different nanotubes. In average the linewidth increases linearly with the transition energies. The higher slope for metallic nanotube (long-dashed line) than that for semiconducting nanotube (short-dashed line) reveals (in average) slightly shorter exciton lifetime due to coupling to free electrons in metallic nanotubes. The large scattering present in the exciton linewidth suggests that ultrafast dynamics of the excited states can vary dramatically with the exact nanotube electronic structure.

4.3.5 Transition Energy Dependent Exciton Linewidth

The optical linewidth of exciton transitions (for p>1) originates mainly from exciton lifetime broadening due to electron-electron and electron-phonon interactions. Ultrafast evolution of the exciton states plays a key role in important optoelectronic processes like multiexciton generation (*80*) and impact ionization (*95*). Our data provide a unique opportunity to investigate the chirality dependent ultrafast dynamics in SWNTs. We plot in Figure 4-12b the observed exciton linewidth in semiconducting (circles) and

metallic (diamonds) nanotubes as a function of exciton transition energies. It shows that (a) the exciton linewidth, in average, increases linearly with transition energy and (b) there is a large variation of exciton lifetime in different nanotube species.

The linear increase of average linewidth indicates a shorter exciton lifetime scales inversely with transition energy. This faster relaxation can be approximately attributed to increased phase space for electron-electron and electron-phonon scatterings at higher energy. Similar increase in excited state relaxation rate with energy has been observed in studies of graphite (*96*) and low-order transitions in carbon nanotubes (*97*). The large variation of exciton lifetime, even for transitions at the same energy, indicates that the ultrafast electron relaxation may depend sensitively on the exact electronic structure, an important effect that has never been explored previously. Our new experimental data could provide some guidance to the theoretical study to gain more insight on ultrafast electron dynamics in 1D systems.

4.3.6 Empirical Formula for Carbon Nanotube Absorption

We further developed an empirical description of the absorption cross-section of an (n,m) nanotube based on the experimentally extracted parameters. Each transition will contribute a Lorentzian peak and a tail at higher energy side described by

$$\frac{\Sigma_p}{\pi}\cdot\frac{w_p}{(E-E_p)^2+w_p^{\,2}}+\frac{\Sigma_p}{a\cdot\pi}\cdot \mathrm{conv}\left(\frac{b\cdot w_p}{E^2+(b\cdot w_p)^2},\frac{\Theta[E-(E_p+\Delta)]}{\sqrt{E-(E_{ii}+\Delta)}}\right), \qquad \text{Eq. 4-11}$$

where Θ is the heavyside step function, conv is the convolution operation, E_p, Σ_p, w_p are respectively the excitonic peak energy, oscillator strength and half linewidth for each optical transition. a, b and Δ describe, respectively, the oscillator strength, energy broadening, and energy offset of the higher energy tail relative to the exciton transition. They are set as constants for all transitions in a given carbon nanotube. p is an integer indexing optical transitions of both semiconducting (S_{ii}) and metallic nanotubes (M_{ii}) starting from 1 in the order of S_{11}, S_{22}, M_{11}, S_{33}, S_{44}, M_{22}, S_{55}, S_{66}, M_{33}, S_{77},…. Sum of contributions (value of Eq. S6) from all resonances at a particular energy gives the total absorption cross-section at that energy. Resonance peak positions are known from the nanotube optical transition atlas established by Raleigh scattering spectroscopy in our recent work (*61*). The oscillator strength and linewidth follow empirical scaling laws described in the text. Parameters a, b and Δ are also approximated empirically as linear functions of nanotube diameter. All the parameters are summarized in Table 4-1. This phenomenological description reproduces the absorption spectra within 20% accuracy in our experimental energy region 1.45-2.55 eV. One representative comparison to the experimental data is shown in Figure 4-13.

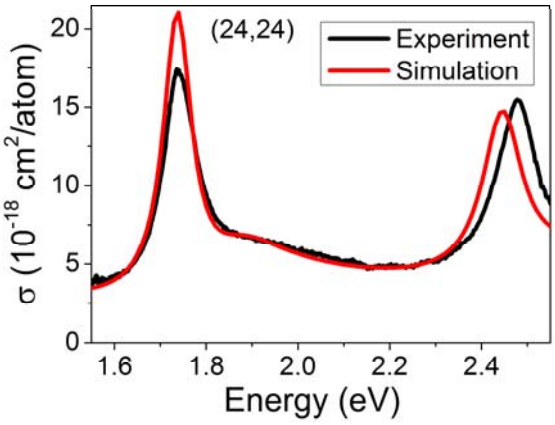

Figure 4-13 Experimental data (black) and empirical prediction of absorption cross-section (red) of (18,14) nanotube

Table 4-1. Parameters for the empirical description of absorption cross-section. Σ_p is in unit of 10^{-18} eV.cm^2/atom; w_p and Δ are in unit of eV; a and b are dimension-less numbers; d is in unit of nm. p is an integer indexing optical transitions of both semiconducting (S_{ii}) and metallic nanotubes (M_{ii}) starting from 1 in the order of S_{11}, S_{22}, M_{11}, S_{33}, S_{44}, M_{22}, S_{55}, S_{66}, M_{33}, S_{77},…

	Semiconducting	Metallic
Σ_p	45.9/[(p+7.5)d]	45.9/[(p+7.5)d]
w_p	0.0194*E_p	0.0214*E_p
a	4.673-0.747*d	0.976+0.186*d
b	0.97+0.256*d	3.065-0.257*d
Δ	0.273-0.041*d	0.175-0.0147*d

4.4 Conclusion

In summary, we have developed a novel way to single nanotube high-throughput imaging and spectroscopy in both reflection geometry and transmission geometry. By manipulating the polarization states of the interfering beams in absorption process, we could greatly enhance the observed contrast level. With this microscopy, many obstacles in carbon nanotube field can be tackled, including fast characterization in growth optimization and in situ performance monitoring and understanding of relaxation pathways when there is additional charges. In addition, this microscopy permits direct absolute measurement of the absorption cross section of individual single-walled nanotubes. It enables us to establish an empirical formula for optical absorption spectra in all nanotubes, which can be crucial for evaluating quantum efficiency of important photoluminescence and photocurrent generation processes. The chirality-dependent exciton absorption resonances further reveal new behavior of electron-hole correlation and ultrafast electron dynamics in nanotubes. This novel absorption spectroscopy can also be applied to investigate other 1D materials, such as graphene nanoribbons, and deepen our understanding of physics at one dimension.

Chapter 5 – Ultrafast Charge Transfer Dynamics in van der Waals coupled Heterostructures of Atomically Thin Transition-metal Dichalcogenides

5.1 Background

5.1.1 The rise of Two Dimensional Materials

Two dimensional atomically thin crystals have recently emerged as a class of materials with many peculiar physical phenomenon and desirable properties of technological applications. Its family includes almost all kinds of building blocks of modern electronics and optoelectronics.

Graphene, atomically thin layer of graphite, attracts intense research interests for exotic physic (ranging from anomalous quantum hall(*98–100*), Klein paradox(*101*), coherent transport (*102*) to atomic collapse(*103*)) and application potentials such as transparent electrodes and electro-optical modulation(*104–106*).

Hexagonal Boron Nitride (hBN) is an insulator with bandgap around 5.8 eV (*107*). Because it is a layered crystal, attempts were made to exfoliate hBN thin film after the successful discovery of graphene. High performance graphene devices was demonstrated using hBN as a substrate due to the absence of dangling bonds and atomically sharp interfaces(*108*). It also stimulated the study of 2D materials heterostructures by demonstrating the coupling to other atomically thin materials, such as the long sought Hofstadter butterfly pattern (*109–111*).

Transition-metal Dichalcogenides (TMDC or MX_2) represents the third category of this classification. The stable monolayer structure is composed of two planes of Chalcogenide atoms and a sandwiched Transition metal layer in a trigonal prismatic structure, as shown in Figure 5-1. They are semiconductors with band gap covering visible and near infrared spectral range. This is ideal for electronic applications with on-off ratio exceeding 10^8 (*112*). Furthermore, because of strong excitonic effect, the light matter interaction at single layer limit is already surprisingly strong(*113–115*). This paves the way for optoelectronics applications with this class of materials. The most common materials are Molybdenum and Tungsten Disulfides and Diselenides. (MoS_2, $MoSe_2$, WS_2 and WSe_2)

Heterostructures can be made of the 2D materials by stacking them in designed order. Since they are coupled mainly by van der Waals (vdW) force, this material is termed vdW heterostructure (*116*).

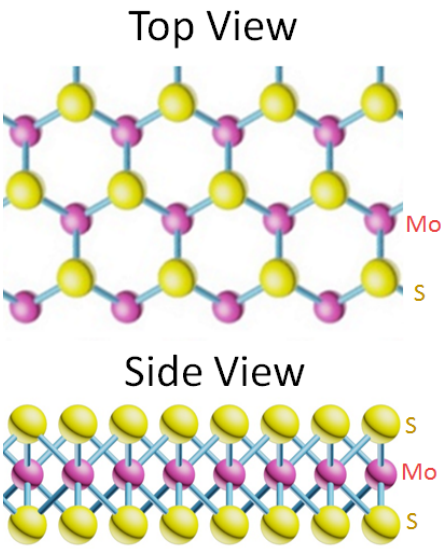

Figure 5-1 Illustration of atomic arrangement for MoS_2

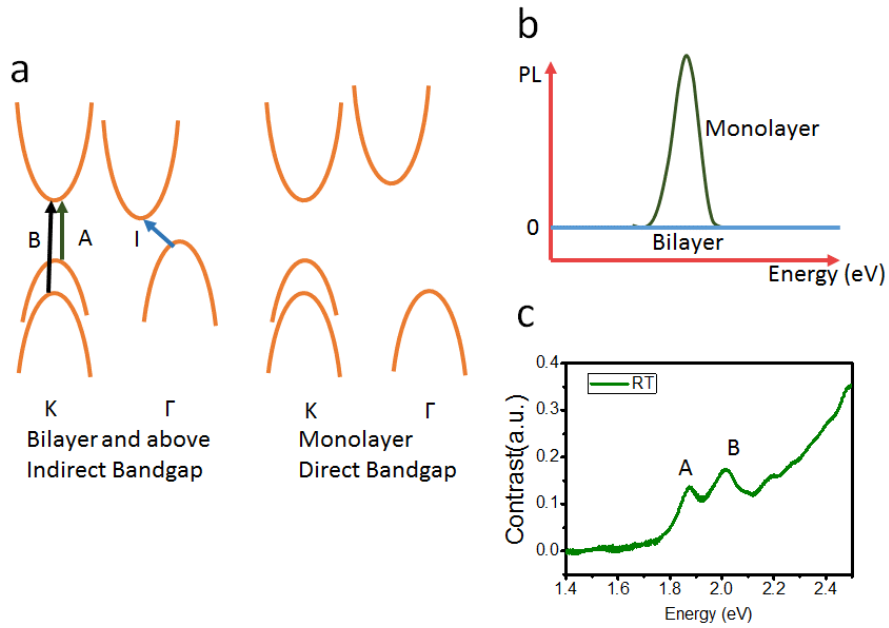

Figure 5-2 Band structure of MoS2 and indirect bandgap to direct bandgap transition. **a.** The indirect bandgap of MoS2 becomes direct bandgap material at monolayer. **b.** Photoluminescence quantum efficiency dramatically increases at monolayer due to the direct bandgap. **c.** absorption spectrum of MoS2, showing two prominent excitonic resonances, corresponding to K point direct bandgap.

5.1.2 Optical properties of Transition-metal Dichalcogenides

The linear optical properties of MX_2 is determined by a combination of band structure and excitonic effects. We will use MoS_2 as an example to study the optical properties, other MX_2 have similar properties.

MoS_2 has a very interesting band structure transition when it is thinned down to monolayer (*114*, *115*). At bulk, MoS2 is an indirect bandgap material, as shown in Figure 5-2a. Conduction band minimum is located between K and Γ point while the valance band maximum is located at Γ point. This band structure does not change qualitatively until it reaches monolayer limit, where both the two mentioned bands shift respectively up and down and are no longer the conduction band minimum and valence band maximum anymore (Figure 5-2). Instead, the direct bandgap becomes the lowest transition and favors a much higher quantum efficiency in photoluminescence, as shown in Figure 5-2b. This indirect band to direct band transition is a unique property of monolayer MX2. Optical resonances can be identified in absorption spectrum where two prominent absorption peaks are labeled as A and B exciton in Figure 5-2c.

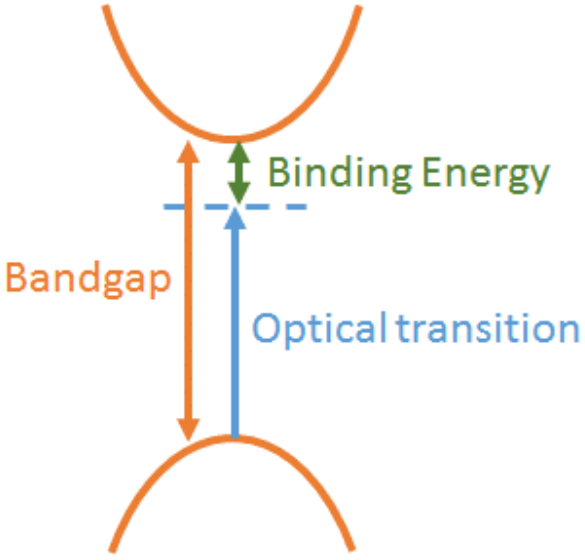

Figure 5-3 Excitons in MoS2. The optical transition is dominated by excitonic transitions, and is smaller than the real bandgap by the binding energy.

Optical transitions in semiconductors is dominated by excitons due to strong Coulomb interactions(*117*). The lowest optical transition is mainly arising from excitonic transitions, with transition energy smaller than the bandgap by exciton binding energy (Figure 5-3). Typically exciton binding energy in traditional semiconductor is on the order of tens of meV(*118*). In low dimensions, this effect could be dramatically enhanced due to size confinement and reduced screening. For example, optical transitions in one dimensional carbon nanotubes are dominated by excitons with binding energy up to ~ 0.5 eV, and this is surprisingly large considering it takes the majority portion of the bandgap of the nanotube (*45*). For monolayer MoS2, a two dimensional crystal, exciton binding

energy is predicted to be around 500 meV to 1 eV (*119*, *120*), and experimentally there are a few groups demonstrating similar binding energies through direct bandgap measurement(*121*), direct absorption measurement (*122*), two photon photoluminescence (*123–125*) and photocurrent measurements(*126*).

Another interesting phenomenon in MX2 systems is the accessible valley degree of freedom. Due to the time reversal symmetry and broken inversion symmetry, K and K' valley features different spins and excitons helicities. Interesting valley dependent physics has been observed with circularly polarized light (*127–130*). Interested readers should go to the references cited here for more details.

5.2 Charge Transfer in Atomically Thin MoS2/WS2 Heterostructures

MX2 heterostructures are particularly exciting for novel optoelectronic and photovoltaic applications, because 2D MX2 monolayers can have an optical bandgap in the near-infrared to visible spectral range and exhibit extremely strong light-matter interactions and photocurrent efficiency (*113*, *131*, *132*). Theory predicts that many stacked MX2 heterostructures also form type-II semiconductor heterojunctions that facilitate efficient electron-hole separation for light detection and harvesting (*133–136*).

5.2.1 Heterostructure Band Alignment

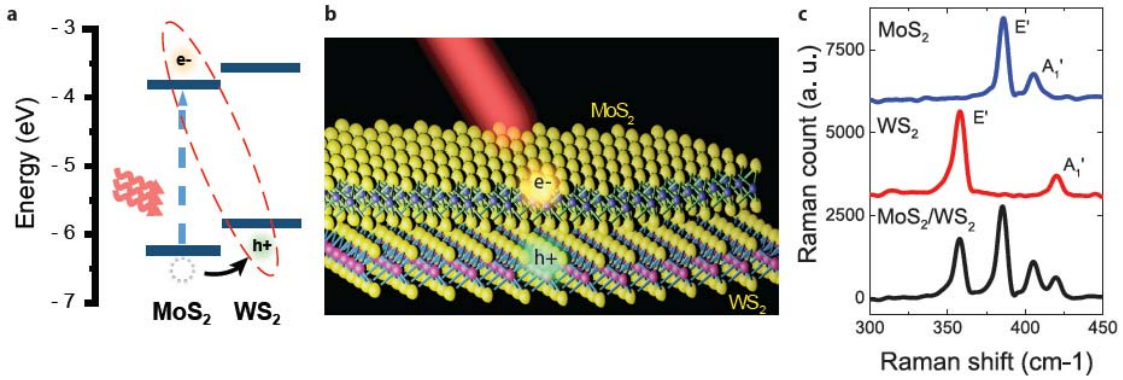

Figure 5-4 Band alignment and structure of MoS2/WS2 heterostructures. a. Schematics of theoretically predicted band alignment of a MoS2/WS2 heterostructure, which forms a type-II heterojunction. Optical excitation of the MoS2 A-exciton will lead to layer separated electron and hole carriers. **b.** Illustration of a MoS2/WS2 heterostructure with a MoS2 monolayer lying on top of a WS2 monolayer. Electrons and holes created by light are shown to separate into different layers. **c.** Raman spectra of an isolated MoS2 monolayer (blue trace), an isolated WS2 monolayer (red trace), and a MoS2/WS2 heterostructure (black trace).

In type-II heterojunctions, the conduction band minimum and valence band maximum reside in two separate materials. Photoexcited electrons and holes therefore prefer to stay at separate locations. Figure 5-4a illustrates the alignment of electronic bands of MoS2 and WS2 monolayers predicted by a recent theory (*133*). It shows that monolayer MoS2 and WS2 has a bandgap of 2.39 eV and 2.31eV, respectively, and the MoS2 valence band maximum is 350 meV lower than that of WS2. Consequently, the MoS2/WS2 heterostructure forms a type-II heterojunction (if we neglect the hybridization of electronic states in MoS2 and WS2 layers), with the conduction band minimum residing in MoS2 and the valence band maximum in WS2, respectively. In the single-particle picture, this heterojunction will lead to efficient charge transfer with separated electron and holes in two layers upon optical excitation (Figure 5-4a), which can have a dominating effect on both light emission and photovoltaic responses in MoS2/WS2 heterostructures.

However, there are two outstanding questions regarding charge transfer processes in the atomically thin and van der Waals-coupled MoS2/WS2 heterostructure. (1) How do strong electron-electron interactions and excitonic effects affect charge transfer processes? (2) How fast can charge transfer take place between van der Waals-coupled layers? Electron-electron interactions are dramatically enhanced in 2D materials due both to size confinement and inefficient screening. Theoretical studies (*119*, *120*) have predicted an exciton binding energy from 500 meV to 1 eV in MX2 monolayers, which is larger than the expected band displacement of 350 meV in MoS2/WS2 heterostructure. Therefore the exciton cannot dissociate into a free electron and a free hole in two separate layers. Will this large exciton binding energy then prevent charge transfer processes and keep the exciton in one layer, or will a new bound state of layer-separated electron and hole pair be generated? In addition, van der Waals coupling is rather weak compared to covalent bonding. Will that lead to a much slower charge transfer process in van der Waals heterostructures compared to their covalent counterparts? Such questions have been extensively studied in molecular donor/acceptor interfaces in the context of organic photovoltaics (*137–139*). However MX2 heterostructure is unique system that helps define these questions in a different context. It possesses large domain crystalline structures and atomically sharp interfaces. As a result, electrons and holes in MX2 layers are largely de-localized and charge transfer between them has to obey rigorous momentum and energy conservation laws. In this letter, we address these questions experimentally. Through combined photoluminescence spectroscopy and optical pump-probe spectroscopy, we demonstrate that ultrafast charge transfer takes place very efficiently in MoS2/WS2 heterostructures. In particular, holes in the MoS2 layer can separate into the WS2 layer within 50 fs upon photo-excitation.

Figure 5-4b schematically shows our sample configuration. In brief, MoS2 monolayers were grown on 285 nm SiO2/Si substrates using the chemical vapour deposition (CVD) method (*140*). They were subsequently transferred on top of as-grown CVD WS2 flakes on sapphire substrates (*141*) to form MoS2/WS2 heterostructures. Raman spectra (Figure 5-4c) from isolated MoS2 and WS2 films confirm that both are monolayers because the energy separation between Raman active modes agrees well with previous reported values for monolayer MoS2 and WS2. (*142–145*) The Raman spectrum of a MoS2/WS2 heterostructure (Figure 5-4c) appears to be an addition of Raman modes from the constituent layers.

5.2.2 Photoluminescence Mapping

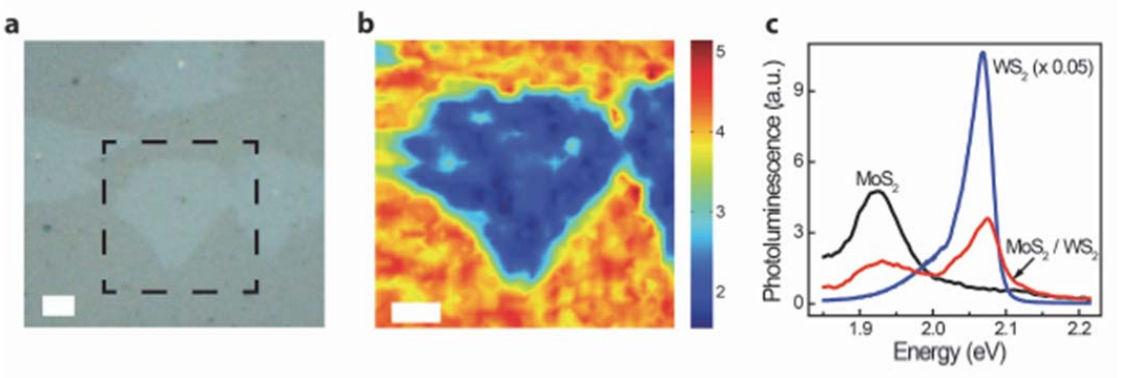

Figure 5-5 Photoluminescence (PL) spectra and mapping of MoS2/WS2 heterostructures at 77 K. a. Optical microscope image of a typical MoS2/WS2 heterostructure sample. The MoS2 layer covers everywhere in the image, and bright areas correspond to MoS2/WS2 heterostructures. **b.** PL mapping data taken in the dashed rectangle area in a. The colour scale represents PL intensity at the MoS2 A-exciton resonance (1.93 eV). It clearly shows that MoS2 PL is strongly quenched in the heterostructure. Scale bar is 5 μm. **c.** Typical PL spectra of an isolated monolayer MoS2, an isolated monolayer WS2 and a MoS2/WS2 heterostructure. The isolated MoS2 and WS2 monolayer show strong PL at 1.93 eV and 2.06 eV, respectively, corresponding to their A-exciton resonances. Both exciton PL signals are strongly quenched in the MoS2/WS2 heterostructure, suggesting an efficient charge transfer process exists in the heterostructure.

One sensitive probe of charge transfer in MX2 heterostructures is photoluminescence (PL) spectroscopy, because an electron and hole pair spatially separated in two MX2 layers cannot emit efficiently. We performed PL spectroscopy and mapping on multiple MoS2/WS2 heterostructure samples. Figure 5-5a displays the optical image of one sample where a large continuous MoS2 piece (covering everywhere in the image) was transferred on top of WS2 flakes (the bright areas). Figure 5-5b shows the PL intensity map at the MoS2 A-exciton resonance (1.93 eV) at 77 K when the sample is excited by 2.33 eV photons. We observed strong PL signals in the MoS2-only region, but the PL is significantly quenched in the MoS2/WS2 heterostructure region. Figure 5-5c further displays typical PL spectra for MoS2/WS2 heterostructures, isolated MoS2, and isolated WS2 layers with 2.33 eV excitation. It is apparent that MoS2 and WS2 monolayers show strong PL at their respective A-exciton resonances (1.93 eV and 2.06 eV), but both PL signals are efficiently quenched in MoS2/WS2 heterostructures. Room temperature PL spectra also exhibit similar behavior as shown in Figure 5-6. In principle, PL signals can be quenched by two mechanisms in a heterostructure: energy transfer and charge transfer. However, energy transfer quenches only the PL from a higher energy transition (i.e. 2.06 eV resonance in WS2), but tends to enhance luminescence from the lower energy transition (i.e. 1.93 eV resonance in MoS_2). On the other hand, charge transfer will quench light emission from all transitions. Therefore the observation of reduced PL from both WS2 and MoS2 exciton resonances in MoS2/WS2 heterostructures demonstrates that efficient charge transfer takes place in this type-II heterojunction.

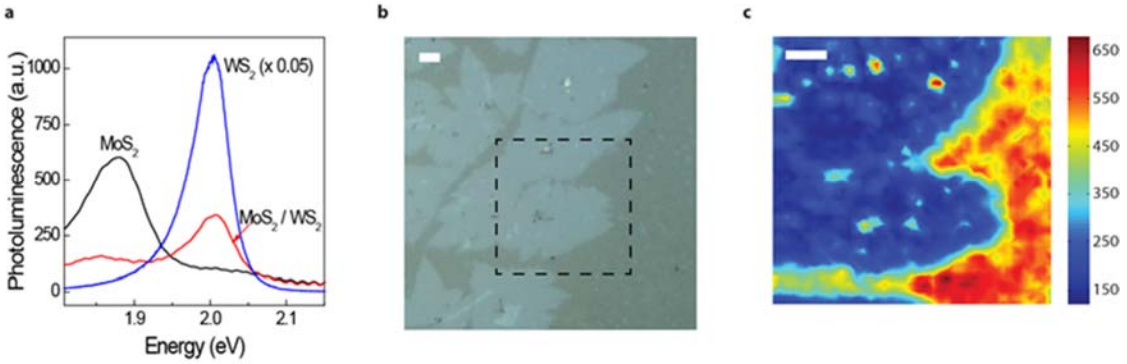

Figure 5-6 Photoluminescence (PL) spectra and mapping of MoS_2/WS_2 heterostructures at Room Temperature a. Typical PL spectra of an isolated monolayer MoS_2, an isolated monolayer WS_2, and a MoS_2/WS_2 heterostructure. The bright exciton PL in isolated monolayer WS_2 and MoS_2 layers are strongly quenched in the heterostructure. **b.** Optical microscope image of a typical MoS_2/WS_2 heterostructure sample. The MoS_2 layer covers everywhere in the image, and bright areas correspond to MoS_2/WS_2 heterostructures. **c.** PL mapping data taken from the dashed rectangle area in a. The color scale represents PL intensity at the MoS_2 A-exciton resonance (1.87 eV). It clearly shows that MoS_2 PL is strongly quenched in the heterostructure. Scale bar is 5 μm.

5.2.3 Pump Probe Measurement

To directly probe the charge transfer process and its ultrafast dynamics, we measured transient absorption spectra of MoS2/WS2 heterostructures using resonant pump-probe spectroscopy. A femtosecond pulse first excites the heterostructure, and the photo-induced changes in the reflection spectrum (ΔR/R) are probed by a laser-generated supercontinuum light after controlled time delays. For atomically thin heterostructures on a transparent sapphire substrate, the reflection change ΔR/R is directly proportional to the change in absorption coefficient (*73*, *146*). MoS2 and WS2 monolayers have distinctly different exciton transitions. Therefore we can selectively excite the MoS2 or WS2 layer using specific resonant optical excitations, and probe the accumulation of electrons and holes in different layers through photo-induced changes in their respective exciton transitions. Specifically, we choose a pump photon energy at 1.86 eV to excite exclusively the A-exciton transition of MoS2. This pump cannot excite WS2 directly because the photon energy is far below the absorption threshold of WS2. Afterwards we examine the photoinduced changes of both WS2 and MoS2 exciton resonances in transient absorption spectra from 2.0-2.5 eV to probe the charge distribution in heterostructures.

Using a pump fluence of 85 μJ/cm^2, A-excitons in MoS2 with a density ~ 5×10^{12}/cm^2 are generated immediately after photo-excitation. Figure 5-7a shows a two-dimensional plot of transient absorption spectra in a MoS2/WS2 heterostructure at 77 K, where the color scale, the horizontal axis, and the vertical axis represent the magnitude of -ΔR/R, the probe photon energy, and pump-probe time delay, respectively. The figure shows prominent resonant features in transient absorption centered on 2.06 eV and 2.46 eV, with the higher

energy feature several times weaker than the lower energy one. Comparing with linear absorption spectra of isolated WS2 and MoS2 monolayers (Figure 5-7e), we can attribute these two resonant features respectively to the A and B-exciton transitions in WS2, although the WS2 layer is not excited by the pump. To better understand the transient absorption spectra in MoS2/WS2 heterostructures, we also performed control experiments for isolated WS2 and MoS2 monolayers. In bare WS2 monolayers no pump-induced signal can be observed above the noise level, consistent with the fact that no direct absorption can take place in WS2. (Figure 5-7f) In isolated MoS2 monolayers, pump-induced absorption changes in our spectral range is centred at 2.11 eV (Figure 3b), corresponding to the B-exciton transition of MoS2. Figure 3c-d show detailed comparisons of transient absorption spectra in a MoS2/WS2 heterostructure and an isolated MoS2 monolayer at the pump-probe time delay of 1 picosecond (ps) (Figure 3c) and 20 ps (Figure 3d). Although the resonant features at 2.06 eV for the heterostructure and at 2.11 eV for monolayer MoS2 are close in energy, they are clearly distinguishable and match well with the A-exciton in WS2 and B-exciton in MoS2 in the absorption spectra (Figure 5-7e), respectively. In addition, the transient absorption signal at the WS2 A-exciton transition in the heterostructure is stronger in magnitude and has a narrower spectral width and a slower decay time constant.

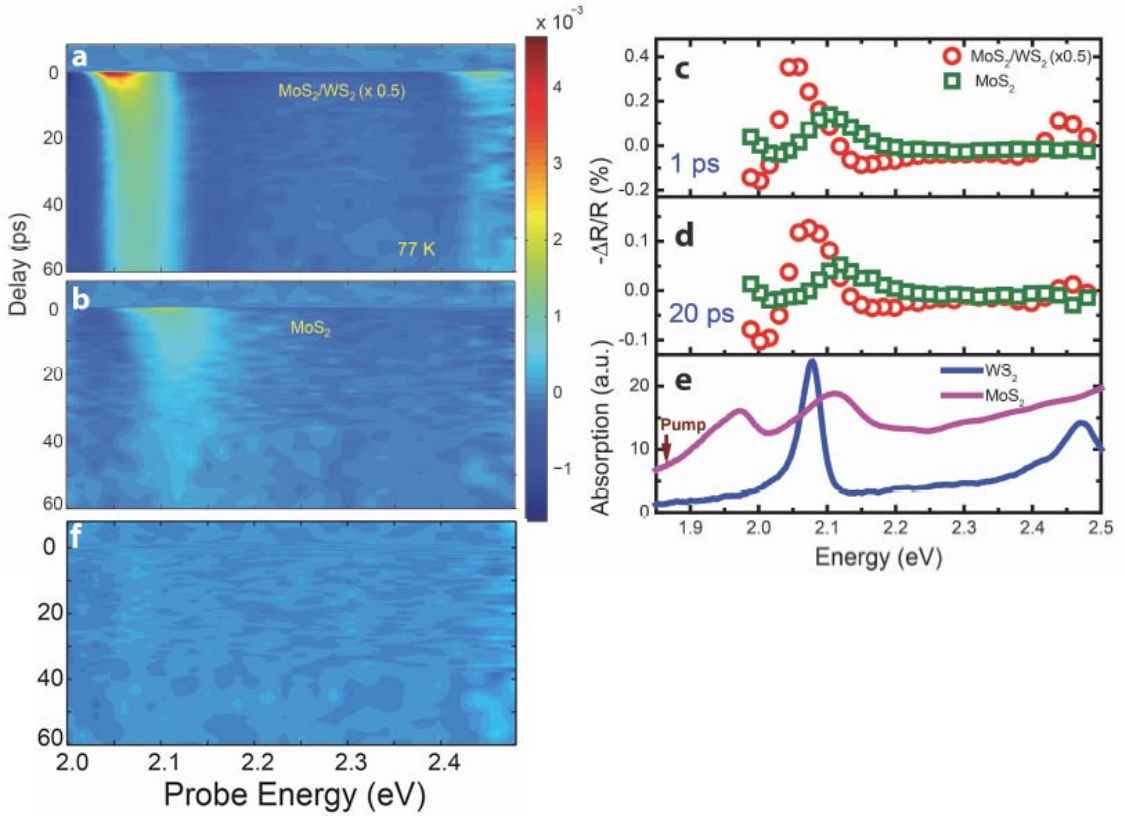

Figure 5-7 Transient absorption spectra of MoS_2/WS_2 heterostructures. a. and **b.** Two-dimensional plots of transient absorption spectra at 77 K from a MoS_2/WS_2 heterostructure (**a**) and an isolated MoS_2 monolayer (**b**) upon excitation of the MoS_2 A-exciton transitions. The horizontal axis, vertical axis, and colour scale represent the probe photon energy,

pump-probe time delay, and the transient absorption signal, respectively. Positive signals indicate a pump-induced decrease in absorption. **c.** and **d.** Transient absorption spectra for MoS_2/WS_2 (red circles) and MoS_2 (green square) at 1 ps and 20 ps pump-probe delay, respectively. **e.** Linear absorption spectra of monolayers of MoS_2 (magenta line) and WS_2 (blue line). Although only MoS_2 A-exciton transitions are optically excited, transient absorption spectra in the MoS_2/WS_2 heterostructure are dominated by a resonance feature (red circles in c and d) corresponding to the WS_2 A-exciton transition (blue line in e), which is clearly distinguishable from the resonance feature corresponding to the MoS_2 B-exciton transition in an isolated MoS_2 monolayer (green squares in c and d and magenta line in e). It demonstrates unambiguously an efficient hole transfer from the photoexcited MoS_2 layer to the WS_2 layer in MoS_2/WS_2 heterostructures. **f.** Same measurement done on isolated WS2. No pump probe signal observed above noise level.

Our transient absorption measurements of MoS2/WS2 heterostructures establish unambiguously that optical excitation in MoS2 leads to strong modification of exciton transitions in WS2, which has a larger optical bandgap. It provides direct evidence of efficient charge separation in photo-excited MoS2/WS2 heterostructures as described in Figure 5-5a: electron hole pairs are initially created in the MoS2 layer, but holes quickly transfer to the WS2 layer due to the type-II band alignment, while electrons stay in the MoS2 layer. The photo-excited electrons in MoS2 and holes in WS2 lead to strong transient absorption signal for exciton transitions in both MoS2 and WS2. Transient absorption signals are the strongest for the A-excitons due to their sharper resonances and efficient photo-bleaching effects from Pauli blocking, but B-exciton transitions are also affected. Consequently, the transient absorption spectra in MoS2/WS2 heterostructures are dominated by the A-exciton transition in WS2. (The A-exciton transition of MoS2 is outside of the probe spectral range because it overlaps with the pump wavelength). Photo-induced changes of B-exciton transitions in the MoS2/WS2 heterostructure (Figure 5-7a) and in the MoS2 monolayer (Figure 5-7b) can also be identified, but they are significantly weaker than that of A-exciton transitions. Room temperature data also show similar trends. (Figure 5-8)

The rise time of the WS2 A-exciton transient absorption signal probes directly the hole transfer dynamics from the MoS2 layer because this signal exists only after the hole transfer, but not right at the excitation of MoS2. Figure 5-9 shows the dynamic evolution of the WS2 A-exciton resonance in the MoS2/WS2 heterostructure (Figure 5-9a), which can be compared to the transient absorption signal for the B-exciton resonance in an isolated MoS2 monolayer (Figure 5-9b). We found that the rise time in both signals are almost identical, and it is limited by the laser pulse duration ~ 250 fs. In Figure 5-9b the MoS2 monolayer is directly pumped, and the photo-induced signal should appear instantaneously. We could reproduce the ultrafast dynamics in the MoS2 monolayer in Figure 5-9b by convoluting the instrument response function (the blue dashed curve in Figure 5-9b) with an instantaneous response in MoS2. Using the same instrument response for time convolution, we can then reproduce the experimentally observed signal in the heterostructure with a rise time shorter than 50 fs (red line in Figure 5-9a). Therefore our results show that holes are transferred from the MoS2 layer to the WS2 layer within 50 fs

after optical excitation of the MoS2/WS2 heterostructure, a remarkably fast rate. Similar ultrafast hole transfer also happens at room temperature, as shown in Figure 5-10. This hole transfer time is much shorter than the exciton lifetime and most other dynamics processes in MX2 monolayers, which are on the order of several to tens of picosecond (*147*). Electrons and holes can therefore be efficiently separated into different layers immediately after their generation. Consequently, PL from MoS2 and WS2 exciton resonances will be strongly quenched, as we observed previously.

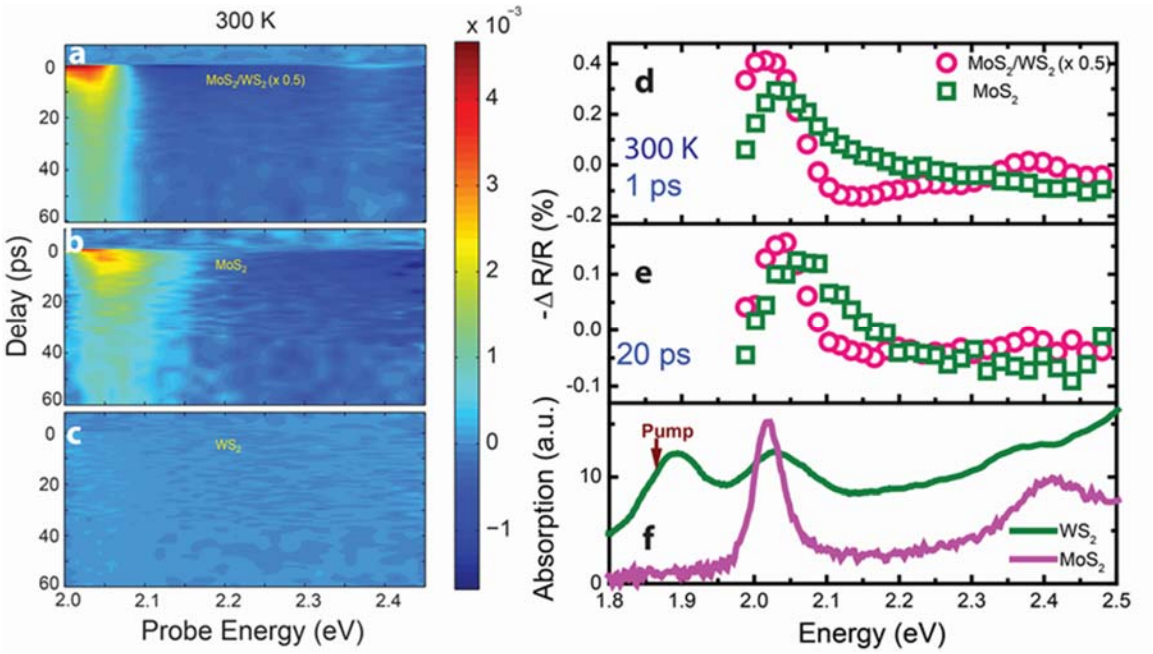

Figure 5-8 Transient absorption spectra of MoS_2/WS_2 heterostructures at room temperature. a. b. and c. Two-dimensional plots of transient absorption spectra at room temperature from a MoS_2/WS_2 heterostructure (**a**) an isolated MoS_2 monolayer (**b**) and an isolated WS_2 monolayer (**c**) upon excitation energy corresponding to the MoS_2 A-exciton transitions (1.86 eV). The horizontal axis, vertical axis, and colour scale represent the probe photon energy, pump-probe time delay, and the transient absorption signal, respectively. Positive signals indicate a pump-induced decrease in absorption. **d. and e.** Transient absorption spectra for MoS_2/WS_2 (magenta circle) and MoS_2 (green square) at 1 ps and 20 ps pump-probe delay, respectively. No pump-induced transient absorption is observed for WS_2 **f.** Linear absorption spectra of monolayers of MoS_2 (green line) and WS_2 (purple line). Although only MoS_2 A-exciton transitions are optically excited, transient absorption spectra in the MoS_2/WS_2 heterostructure are dominated by a resonance feature (magenta circles in c and d) corresponding to the WS_2 A-exciton transition (purple line in f), which is clearly distinguishable from the resonance feature corresponding to the MoS_2 B-exciton transition in an isolated MoS_2 monolayer (green squares in **d** and e and green line in f). It demonstrates unambiguously an efficient hole transfer from the photoexcited MoS_2 layer to the WS_2 layer in MoS_2/WS_2 heterostructures.

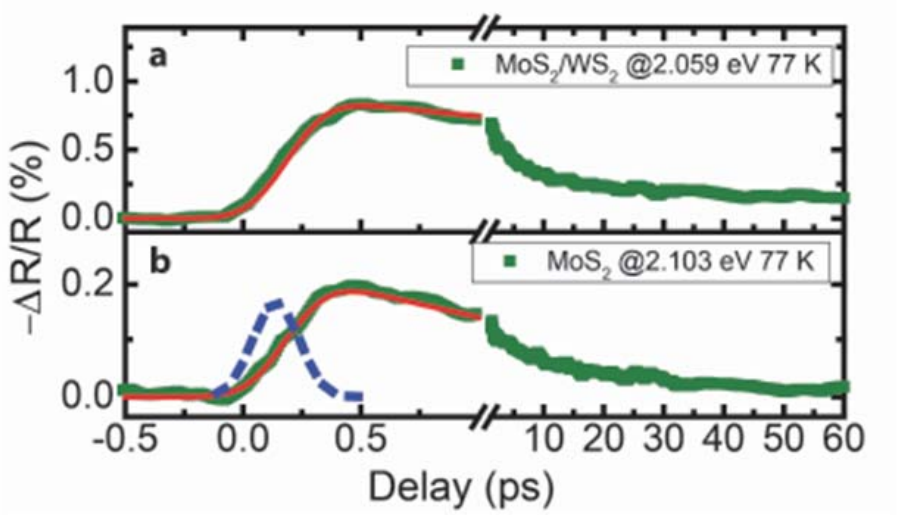

Figure 5-9 Ultrafast hole transfer dynamics from vertical cuts in Figure 5-7a and b. a. The evolution of transient absorption signals at the WS_2 A-exciton resonance in the MoS_2/WS_2 heterostructure. **b.** The dynamic evolution of transient absorption signals at the MoS_2 B-exciton resonance in the isolated MoS_2 monolayer. Both signals show almost identical ultrafast rise time, which is limited by the laser pulse duration ~ 250 fs. By convoluting the instrument response function (blue dashed line in b) and an instantaneous response in MoS_2, we can reproduce the ultrafast dynamics in the MoS_2 monolayer (red trace in b). Similar convolution shows that the rise time in MoS_2/WS_2 monolayer is around 25 fs (red trace in a), and has an upper limit of 50 fs. It demonstrates that holes can transfer from the photoexcited MoS_2 layer to the WS_2 layer within 50 fs in the MoS_2/WS_2 heterostructure.

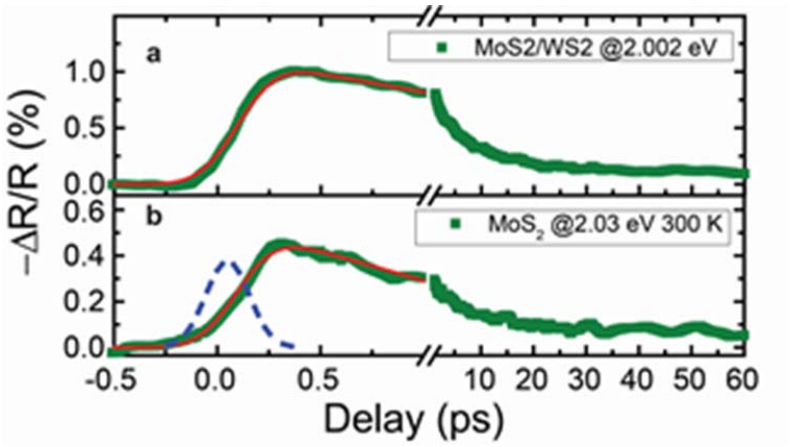

Figure 5-10 Ultrafast hole transfer dynamics from vertical cuts in Figure 5-8. a and b. a. The evolution of transient absorption signals at the WS2 A-exciton resonance in the MoS2/WS2 heterostructure. **b.** The dynamic evolution of transient absorption signals at the MoS2 B-exciton resonance in the isolated MoS2 monolayer. Both signals show almost identical ultrafast rise time, which is limited by the laser pulse duration ~ 250 fs. By convoluting the instrument response function (blue dashed line in b) and an instantaneous response in MoS2, we can reproduce the ultrafast dynamics in the MoS2 monolayer (red trace in b). Similar convolution shows that the rise time in MoS2/WS2 monolayer is around

25 fs (red trace in a), and has an upper limit of 50 fs. It demonstrates that holes can transfer from the photoexcited MoS2 layer to the WS2 layer within 50 fs in the MoS2/WS2 heterostructure at room temperature.

Our experimental data establishes that charge separation in MoS2/WS2 heterostructures is very efficient, although the band offset between MoS2 and WS2 is smaller than the predicted exciton binding energy in monolayer MX2. Energetically uncorrelated free electrons and holes in separated MoS2 and WS2 layers cannot be produced through the excitation of MoS2 A-excitons. However, the MoS2 and WS2 layers are only ~0.62 nm separated from each other (*134*), suggesting that even for layer-separated electrons and holes, strong Coulomb interactions can lead to bound exciton states. These exciton states with electron and hole residing in different layers can be energetically favorable compared to an exciton confined to only MoS2 layer, and are likely to be responsible for the efficient charge separation observed in MoS2/WS2 heterostructures. Such bounded excitons with electron and hole in different materials, known as charge transfer excitons (CTC), have also been investigated in other type-II heterojunctions, such as molecular donor/acceptor interfaces in the context of organic photovoltaics (*137–139*)

5.2.4 Comparison with Organic Photovoltaic

The observed sub-50 fs hole transfer time is remarkably short considering that the MoS2 and WS2 layers are randomly stacked and are coupled by relatively weak van der Waals interactions while still need to satisfy the stringent energy and momentum conservations. One factor contributing to the ultrafast charge transfer rate in atomically thin heterostructures is the close proximity of the two heterolayers, because electrons or holes only need to move less than 1 nm vertically for the charge transfer process to happen. Still, the 50 fs hole transfer time for van der Waals heterostructures is surprisingly fast. Microscopic understanding of this ultrafast hole transfer in MX2 heterostructures requires detailed theoretical studies to examine the hybridization of electronic states in twisted heterolayers and the dynamic evolution of photo-excited states due to electron-phonon and electron-electron interactions. It is known that for MoS2 bilayers, electronic coupling at the K point in the Brillouin zone is rather weak. Electron wavefunction hybridization at the Γ point, however, is much stronger, which leads to a rise in Γ point valence band and an indirect bandgap in bilayer MoS2.(*114*, *115*) This indirect bandgap could open up a new way of hole relaxation. If the Γ point rises beyond the K point in the valence band in MoS2, the holes could quickly relaxes to the Γ point, and from Γ point of MoS2 transfer to Γ point of WS2. Because Γ point coupling could be reasonably strong in the twisted heterolayers, ultrafast charge transfer within 50 fs is made plausible. Electronic coupling between incommensurate MoS2 and WS2 will play an important role in the charge transfer dynamics of twisted MoS2/WS2 heterostructures, the behavior of which has been little studied so far. However this requires deeper theoretical support and is not available to date. In addition, further experimental work will be needed to understand the role of interlayer electric field.

In comparison, the charge transfer time in molecular donor/acceptor interfaces from organic photovoltaic has been experimentally observed and theoretically studied. The charge transfer can be as fast as 50 fs depending on specific electronic couplings and band alignments (*137–139*). The vdW-coupled 2D heterostructures, however, represent a completely new class of materials. Our observation of efficient charge transfer at 50 fs time scale in these heterostructures are of both fundamental and technological importance, as we explain below. Scientifically, the MX2 heterolayers are very different from molecular donor/acceptors because the 2D heterostructures are composed of two-dimensional crystalline sheets that exhibit translational symmetry and extended electron wavefunctions. In molecular donor/acceptor systems, the charge transfer rate is purely determined by the overlap of density of states because only energy conservation needs to be satisfied. In contrast, resonant charge transfer between 2D layers has to satisfy both energy and momentum conservation. Therefore the charge transfer process in MX2 heterostructures can sensitively depend on the momentum-dependent electronic structure. For example, previous studies have shown that exciton transitions take place at the K point of Brillouin zone in MX2 monolayers, but the interlayer electronic coupling at the K point are extremely weak13. In addition, the Brillouin zone of MoS2 and WS2 layers are twisted relative to each other. Therefore whether efficient charge transfer like that in OPV systems can take place in MX2 heterostructures is far from certain. Our study provide the first experimental evidence show that charge transfer in such layered 2D heterostructures can indeed be as fast as that between molecular donor/acceptors. We expect it to stimulate further theoretical investigations to understand the microscopic processes governing the charge transfer dynamics. Technologically, MX2 heterostructures provide a promising alternative route for light harvesting applications. It has been shown that MX2 layers have very strong optical absorption (*113–115*). In addition, charge transport in such extended crystalline 2D layers can be much more efficient than organic molecules(*113*, *131*). Experimental knowledge of charge transfer dynamics in such 2D MX2 heterostructures will be important to evaluate and optimize their potential applications.

5.3 Conclusion

In summary, we have demonstrated for the first time efficient charge transfer in MoS2/WS2 heterostructures through combined PL mapping and transient absorption measurement. We quantitatively determine the ultrafast hole transfer time to be less than 50 fs Our study suggests that MX2 heterostructures, with their remarkable electrical and optical properties and rapid development of large area synthesis, hold great promise for future optoelectronic and photovoltaic applications.

References

1. W. Demtröder, *Laser Spectroscopy: Basic Concepts and Instrumentation* (Springer, 2003).
2. G. P. Agrawal, N. K. Dutta, *Semiconductor Lasers* (Springer US, Boston, MA, 1995).
3. J. Faist *et al.*, Quantum cascade laser, *Science* **264**, 553–6 (1994).
4. K. Nakamoto, *Infrared and Raman spectra of inorganic and coordination compounds* J. M. Chalmers, P. R. Griffiths, Eds. (John Wiley & Sons, Ltd, Chichester, UK, 1978).
5. E. Hecht, *Optics* (Addison-Wesley, 2002), p. 698.
6. Y. R. Shen, *The principles of nonlinear optics* (Wiley-Interscience, 2003), p. 563.
7. M. M. Fejer, G. A. Magel, D. H. Jundt, R. L. Byer, Quasi-phase-matched second harmonic generation: tuning and tolerances, *IEEE J. Quantum Electron.* **28**, 2631–2654 (1992).
8. L. E. Myers *et al.*, Quasi-phase-matched optical parametric oscillators in bulk periodically poled LiNbO_3, *J. Opt. Soc. Am. B* **12**, 2102 (1995).
9. M. Nakamura *et al.*, Optical Damage Resistance and Refractive Indices in Near-Stoichiometric MgO-Doped LiNbO3, *Jpn. J. Appl. Phys.* **41**, L49–L51 (2002).
10. A. Smith, SNLO (available at http://www.as-photonics.com/snlo).
11. L. Myers, W. Bosenberg, Periodically poled lithium niobate and quasi-phase-matched optical parametric oscillators, *Quantum Electron. IEEE J. …* , 1663–1672 (1997).
12. O. Gayer, Z. Sacks, E. Galun, A. Arie, Temperature and wavelength dependent refractive index equations for MgO-doped congruent and stoichiometric LiNbO3, *Appl. Phys. B* **91**, 343–348 (2008).
13. K. Liu, M. G. Littman, Novel geometry for single-mode scanning of tunable lasers, *Opt. Lett.* **6**, 117 (1981).
14. E. Andrieux, T. Zanon, M. Cadoret, A. Rihan, J.-J. Zondy, 500 GHz mode-hop-free idler tuning range with a frequency-stabilized singly resonant optical parametric oscillator., *Opt. Lett.* **36**, 1212–4 (2011).
15. X. Hong, X. Shen, M. Gong, F. Wang, Broadly tunable mode-hop-free mid-infrared light source with MgO:PPLN continuous-wave optical parametric oscillator., *Opt. Lett.* **37**, 4982–4 (2012).
16. G. Binnig, H. Rohrer, C. Gerber, E. Weibel, Surface Studies by Scanning Tunneling Microscopy, *Phys. Rev. Lett.* **49**, 57–61 (1982).
17. M. F. Crommie, C. P. Lutz, D. M. Eigler, Confinement of electrons to quantum corrals on a metal surface., *Science* **262**, 218–20 (1993).
18. N. Lang, Spectroscopy of single atoms in the scanning tunneling microscope, *Phys. Rev. B* **34**, 5947–5950 (1986).
19. B. C. Stipe, Single-Molecule Vibrational Spectroscopy and Microscopy, *Science (80-.).* **280**, 1732–1735 (1998).
20. I. V. Pechenezhskiy *et al.*, Infrared Spectroscopy of Molecular Submonolayers on Surfaces by Infrared Scanning Tunneling Microscopy: Tetramantane on Au(111), *Phys. Rev. Lett.* **111**, 126101 (2013).

21. Y. Wang *et al.*, Spatially resolved electronic and vibronic properties of single diamondoid molecules., *Nature Mater.* **7**, 38–42 (2008).
22. J. E. Dahl, S. G. Liu, R. M. K. Carlson, Isolation and structure of higher diamondoids, nanometer-sized diamond molecules., *Science* **299**, 96–9 (2003).
23. M. Völcker, Laser-assisted scanning tunneling microscopy, *J. Vac. Sci. Technol. B Microelectron. Nanom. Struct.* **9**, 541 (1991).
24. T. Holstein, Optical and Infrared Reflectivity of Metals at Low Temperatures, *Phys. Rev.* **88**, 1427–1428 (1952).
25. M. M. Fulk, M. M. Reynolds, Emissivities of Metallic Surfaces at 76°K, *J. Appl. Phys.* **28**, 1464 (1957).
26. L. J. Lauhon, W. Ho, Effects of temperature and other experimental variables on single molecule vibrational spectroscopy with the scanning tunneling microscope, *Rev. Sci. Instrum.* **72**, 216 (2001).
27. J. B. Maddox *et al.*, Simulation of single molecule inelastic electron tunneling signals in paraphenylene-vinylene oligomers and distyrylbenzene[2.2]paracyclophanes., *J. Phys. Chem. A* **110**, 6329–38 (2006).
28. A. Troisi, M. A. Ratner, Propensity rules for inelastic electron tunneling spectroscopy of single-molecule transport junctions., *J. Chem. Phys.* **125**, 214709 (2006).
29. J. Oomens *et al.*, Infrared spectroscopic investigation of higher diamondoids, *J. Mol. Spectrosc.* **238**, 158–167 (2006).
30. F. Hoffmann, Infrared reflection-absorption spectroscopy of adsorbed molecules, *Surf. Sci. Rep.* **3**, 107 (1983).
31. Y. Sakai *et al.*, Intermolecular interactions and substrate effects for an adamantane monolayer on a Au(111) surface, *Phys. Rev. B* **88**, 235407 (2013).
32. A. A. Fokin *et al.*, Stable alkanes containing very long carbon-carbon bonds., *J. Am. Chem. Soc.* **134**, 13641–50 (2012).
33. P. R. Schreiner *et al.*, Overcoming lability of extremely long alkane carbon-carbon bonds through dispersion forces., *Nature* **477**, 308–11 (2011).
34. M. M. J. Treacy, T. W. Ebbesen, J. M. Gibson, Exceptionally high Young's modulus observed for individual carbon nanotubes, *Nature* **381**, 678–680 (1996).
35. M. S. Strano *et al.*, Electronic structure control of single-walled carbon nanotube functionalization., *Science* **301**, 1519–22 (2003).
36. W. Liang *et al.*, Fabry - Perot interference in a nanotube electron waveguide., *Nature* **411**, 665–9 (2001).
37. A. Bachtold *et al.*, Scanned Probe Microscopy of Electronic Transport in Carbon Nanotubes, *Phys. Rev. Lett.* **84**, 6082–6085 (2000).
38. R. H. Baughman, A. A. Zakhidov, W. A. de Heer, Carbon nanotubes--the route toward applications., *Science* **297**, 787–92 (2002).
39. A. Javey, J. Guo, Q. Wang, M. Lundstrom, H. Dai, Ballistic carbon nanotube field-effect transistors., *Nature* **424**, 654–7 (2003).
40. R. Martel, T. Schmidt, H. R. Shea, T. Hertel, P. Avouris, Single- and multi-wall carbon nanotube field-effect transistors, *Appl. Phys. Lett.* **73**, 2447 (1998).
41. P. Collins, M. Hersam, M. Arnold, R. Martel, P. Avouris, Current Saturation and Electrical Breakdown in Multiwalled Carbon Nanotubes, *Phys. Rev. Lett.* **86**, 3128–3131 (2001).

42. B. Q. Wei, R. Vajtai, P. M. Ajayan, Reliability and current carrying capacity of carbon nanotubes, *Appl. Phys. Lett.* **79**, 1172 (2001).
43. P. Wallace, The Band Theory of Graphite, *Phys. Rev.* **71**, 622–634 (1947).
44. R. Saito, G. Dresselhaus, M. S. Dresselhaus, *Physical Properties of Carbon Nanotube* (Imperial College Press, 1998), p. 259.
45. F. Wang, G. Dukovic, L. E. Brus, T. F. Heinz, The optical resonances in carbon nanotubes arise from excitons., *Science* **308**, 838–41 (2005).
46. T. Pedersen, Variational approach to excitons in carbon nanotubes, *Phys. Rev. B* **67**, 073401 (2003).
47. A. Jorio *et al.*, Joint density of electronic states for one isolated single-wall carbon nanotube studied by resonant Raman scattering, *Phys. Rev. B* **63**, 245416 (2001).
48. A. Jorio *et al.*, Structural (n, m) determination of isolated single-wall carbon nanotubes by resonant Raman scattering., *Phys. Rev. Lett.* **86**, 1118–21 (2001).
49. Z. Yu, L. Brus, Rayleigh and Raman Scattering from Individual Carbon Nanotube Bundles, *J. Phys. Chem. B* **105**, 1123–1134 (2001).
50. G. S. Duesberg, I. Loa, M. Burghard, K. Syassen, S. Roth, Polarized raman spectroscopy on isolated single-wall carbon nanotubes., *Phys. Rev. Lett.* **85**, 5436–9 (2000).
51. K. Liu *et al.*, Quantum-coupled radial-breathing oscillations in double-walled carbon nanotubes., *Nat. Commun.* **4**, 1375 (2013).
52. M. J. O'Connell *et al.*, Band gap fluorescence from individual single-walled carbon nanotubes., *Science* **297**, 593–6 (2002).
53. A. Hartschuh, H. N. Pedrosa, L. Novotny, T. D. Krauss, Simultaneous fluorescence and Raman scattering from single carbon nanotubes., *Science* **301**, 1354–6 (2003).
54. J. Lefebvre, Y. Homma, P. Finnie, Bright band gap photoluminescence from unprocessed single-walled carbon nanotubes., *Phys. Rev. Lett.* **90**, 217401 (2003).
55. F. Wang *et al.*, Observation of excitons in one-dimensional metallic single-walled carbon nanotubes., *Phys. Rev. Lett.* **99**, 227401 (2007).
56. J.-C. Blancon *et al.*, Direct measurement of the absolute absorption spectrum of individual semiconducting single-wall carbon nanotubes., *Nat. Commun.* **4**, 2542 (2013).
57. S. Berciaud, L. Cognet, P. Poulin, R. B. Weisman, B. Lounis, Absorption spectroscopy of individual single-walled carbon nanotubes., *Nano Lett.* **7**, 1203–7 (2007).
58. F. Wang *et al.*, Interactions between Individual Carbon Nanotubes Studied by Rayleigh Scattering Spectroscopy, *Phys. Rev. Lett.* **96**, 167401 (2006).
59. M. Y. Sfeir *et al.*, Probing electronic transitions in individual carbon nanotubes by Rayleigh scattering., *Science* **306**, 1540–3 (2004).
60. M. Y. Sfeir *et al.*, Optical spectroscopy of individual single-walled carbon nanotubes of defined chiral structure., *Science* **312**, 554–6 (2006).
61. K. Liu *et al.*, An atlas of carbon nanotube optical transitions., *Nature Nanotech* **7**, 325–9 (2012).
62. D. Y. Joh *et al.*, On-chip Rayleigh imaging and spectroscopy of carbon nanotubes., *Nano Lett.* **11**, 1–7 (2011).
63. D. Y. Joh *et al.*, Single-walled carbon nanotubes as excitonic optical wires., *Nature Nanotech* **6**, 51–6 (2011).

64. K. Liu *et al.*, High-throughput optical imaging and spectroscopy of individual carbon nanotubes in devices., *Nature Nanotech* **8**, 917–22 (2013).
65. P. C. Robinson, S. Bradbury, *Qualitative polarized-light microscopy* (Oxford University Press, 1992; http://books.google.com/books/about/Qualitative_polarized_light_microscopy.html?id=JS3wAAAAMAAJ&pgis=1), p. 121.
66. J. Lefebvre, P. Finnie, Polarized light microscopy and spectroscopy of individual single-walled carbon nanotubes, *Nano Res.* **4**, 788–794 (2011).
67. J. Lekner, Polarization of tightly focused laser beams, *J. Opt. A Pure Appl. Opt.* **5**, 6–14 (2003).
68. K. Liu *et al.*, Intrinsic radial breathing oscillation in suspended single-walled carbon nanotubes, *Phys. Rev. B* **83**, 113404 (2011).
69. S. M. Bachilo *et al.*, Structure-assigned optical spectra of single-walled carbon nanotubes., *Science* **298**, 2361–6 (2002).
70. W. Zhou, S. Zhan, L. Ding, J. Liu, General rules for selective growth of enriched semiconducting single walled carbon nanotubes with water vapor as in situ etchant., *J. Am. Chem. Soc.* **134**, 14019–26 (2012).
71. J. C. Tsang, M. Freitag, V. Perebeinos, J. Liu, P. Avouris, Doping and phonon renormalization in carbon nanotubes., *Nature Nanotech* **2**, 725–30 (2007).
72. M. J. O' Connell, E. E. Eibergen, S. K. Doorn, Chiral selectivity in the charge-transfer bleaching of single-walled carbon-nanotube spectra., *Nature Mater.* **4**, 412–8 (2005).
73. F. Wang *et al.*, Gate-variable optical transitions in graphene., *Science* **320**, 206–9 (2008).
74. M. Steiner *et al.*, Gate-variable light absorption and emission in a semiconducting carbon nanotube., *Nano Lett.* **9**, 3477–81 (2009).
75. S. M. Santos *et al.*, All-Optical Trion Generation in Single-Walled Carbon Nanotubes, *Phys. Rev. Lett.* **107**, 187401 (2011).
76. X. Xu, N. M. Gabor, J. S. Alden, A. M. van der Zande, P. L. McEuen, Photo-thermoelectric effect at a graphene interface junction., *Nano Lett.* **10**, 562–6 (2010).
77. J. Lefebvre, P. Finnie, Polarized Photoluminescence Excitation Spectroscopy of Single-Walled Carbon Nanotubes, *Phys. Rev. Lett.* **98**, 167406 (2007).
78. M. Freitag, Y. Martin, J. A. Misewich, R. Martel, P. Avouris, Photoconductivity of Single Carbon Nanotubes, *Nano Lett.* **3**, 1067–1071 (2003).
79. C. M. Aguirre *et al.*, Carbon nanotube sheets as electrodes in organic light-emitting diodes, *Appl. Phys. Lett.* **88**, 183104 (2006).
80. N. M. Gabor, Z. Zhong, K. Bosnick, J. Park, P. L. McEuen, Extremely efficient multiple electron-hole pair generation in carbon nanotube photodiodes., *Science* **325**, 1367–71 (2009).
81. AndoTsuneya, Excitons in Carbon Nanotubes, (2013) (available at http://journals.jps.jp/doi/abs/10.1143/JPSJ.66.1066).
82. C. Kane, E. Mele, Electron Interactions and Scaling Relations for Optical Excitations in Carbon Nanotubes, *Phys. Rev. Lett.* **93**, 197402 (2004).
83. C. Spataru, S. Ismail-Beigi, L. Benedict, S. Louie, Excitonic Effects and Optical Spectra of Single-Walled Carbon Nanotubes, *Phys. Rev. Lett.* **92**, 077402 (2004).

84. E. Malic, J. Maultzsch, S. Reich, A. Knorr, Excitonic absorption spectra of metallic single-walled carbon nanotubes, *Phys. Rev. B* **82**, 035433 (2010).
85. V. Perebeinos, J. Tersoff, P. Avouris, Scaling of Excitons in Carbon Nanotubes, *Phys. Rev. Lett.* **92**, 257402 (2004).
86. K. Liu *et al.*, Systematic Determination of Absolute Absorption Cross-section of Individual Carbon Nanotubes, (2013) (available at http://arxiv.org/abs/1311.3328).
87. M. F. Islam, D. E. Milkie, C. L. Kane, A. G. Yodh, J. M. Kikkawa, Direct measurement of the polarized optical absorption cross section of single-wall carbon nanotubes., *Phys. Rev. Lett.* **93**, 037404 (2004).
88. Y. Murakami, E. Einarsson, T. Edamura, S. Maruyama, Polarization Dependence of the Optical Absorption of Single-Walled Carbon Nanotubes, *Phys. Rev. Lett.* **94**, 087402 (2005).
89. S. Nanot *et al.*, Broadband, polarization-sensitive photodetector based on optically-thick films of macroscopically long, dense, and aligned carbon nanotubes., *Sci. Rep.* **3**, 1335 (2013).
90. Y. Miyauchi, M. Oba, S. Maruyama, Cross-polarized optical absorption of single-walled nanotubes by polarized photoluminescence excitation spectroscopy, *Phys. Rev. B* **74**, 205440 (2006).
91. S. Uryu, T. Ando, Exciton absorption of perpendicularly polarized light in carbon nanotubes, *Phys. Rev. B* **74**, 155411 (2006).
92. K. F. Mak, J. Shan, T. F. Heinz, Seeing Many-Body Effects in Single- and Few-Layer Graphene: Observation of Two-Dimensional Saddle-Point Excitons, *Phys. Rev. Lett.* **106**, 046401 (2011).
93. R. R. Nair *et al.*, Fine structure constant defines visual transparency of graphene., *Science* **320**, 1308 (2008).
94. S. Choi, J. Deslippe, R. B. Capaz, S. G. Louie, An explicit formula for optical oscillator strength of excitons in semiconducting single-walled carbon nanotubes: family behavior., *Nano Lett.* **13**, 54–8 (2013).
95. J. Chen *et al.*, Bright infrared emission from electrically induced excitons in carbon nanotubes., *Science* **310**, 1171–4 (2005).
96. M. Steiner *et al.*, How does the substrate affect the Raman and excited state spectra of a carbon nanotube?, *Appl. Phys. A* **96**, 271–282 (2009).
97. T. Hertel *et al.*, Intersubband decay of 1-D exciton resonances in carbon nanotubes., *Nano Lett.* **8**, 87–91 (2008).
98. K. S. Novoselov *et al.*, Two-dimensional gas of massless Dirac fermions in graphene., *Nature* **438**, 197–200 (2005).
99. K. S. Novoselov *et al.*, Unconventional quantum Hall effect and Berry's phase of 2π in bilayer graphene, *Nat. Phys.* **2**, 177–180 (2006).
100. Y. Zhang, Y.-W. Tan, H. L. Stormer, P. Kim, Experimental observation of the quantum Hall effect and Berry's phase in graphene., *Nature* **438**, 201–4 (2005).
101. M. I. Katsnelson, K. S. Novoselov, A. K. Geim, Chiral tunnelling and the Klein paradox in graphene, *Nat. Phys.* **2**, 620–625 (2006).
102. F. Miao *et al.*, Phase-coherent transport in graphene quantum billiards., *Science* **317**, 1530–3 (2007).
103. Y. Wang *et al.*, Observing atomic collapse resonances in artificial nuclei on graphene., *Science* **340**, 734–7 (2013).

104. A. Majumdar, J. Kim, J. Vuckovic, F. Wang, Electrical control of silicon photonic crystal cavity by graphene., *Nano Lett.* **13**, 515–8 (2013).
105. J. Kim *et al.*, Electrical control of optical plasmon resonance with graphene., *Nano Lett.* **12**, 5598–602 (2012).
106. M. Liu *et al.*, A graphene-based broadband optical modulator., *Nature* **474**, 64–7 (2011).
107. K. Watanabe, T. Taniguchi, H. Kanda, Direct-bandgap properties and evidence for ultraviolet lasing of hexagonal boron nitride single crystal., *Nature Mater.* **3**, 404–9 (2004).
108. C. R. Dean *et al.*, Boron nitride substrates for high-quality graphene electronics., *Nature Nanotech* **5**, 722–6 (2010).
109. L. a Ponomarenko *et al.*, Cloning of Dirac fermions in graphene superlattices., *Nature* **497**, 594–7 (2013).
110. B. Hunt *et al.*, Massive Dirac fermions and Hofstadter butterfly in a van der Waals heterostructure., *Science* **340**, 1427–30 (2013).
111. C. R. Dean *et al.*, Hofstadter's butterfly and the fractal quantum Hall effect in moiré superlattices., *Nature* **497**, 598–602 (2013).
112. B. Radisavljevic, A. Radenovic, J. Brivio, V. Giacometti, A. Kis, Single-layer MoS2 transistors., *Nature Nanotech* **6**, 147–50 (2011).
113. L. Britnell *et al.*, Strong light-matter interactions in heterostructures of atomically thin films., *Science* **340**, 1311–4 (2013).
114. K. F. Mak, C. Lee, J. Hone, J. Shan, T. F. Heinz, Atomically Thin MoS2: A New Direct-Gap Semiconductor, *Phys. Rev. Lett.* **105**, 136805 (2010).
115. A. Splendiani *et al.*, Emerging photoluminescence in monolayer MoS2., *Nano Lett.* **10**, 1271–5 (2010).
116. A. K. Geim, I. V Grigorieva, Van der Waals heterostructures., *Nature* **499**, 419–25 (2013).
117. N. W. Ashcroft, N. D. Mermin, *Solid state physics* (Saunders College, 1976), p. 826.
118. R. Kaindl, D. Hägele, M. Carnahan, D. Chemla, Transient terahertz spectroscopy of excitons and unbound carriers in quasi-two-dimensional electron-hole gases, *Phys. Rev. B* **79**, 045320 (2009).
119. T. C. Berkelbach, M. S. Hybertsen, D. R. Reichman, Theory of neutral and charged excitons in monolayer transition metal dichalcogenides, *Phys. Rev. B* **88**, 045318 (2013).
120. D. Y. Qiu, F. H. da Jornada, S. G. Louie, Optical Spectrum of MoS2: Many-Body Effects and Diversity of Exciton States, *Phys. Rev. Lett.* **111**, 216805 (2013).
121. M. M. Ugeda *et al.*, Observation of giant bandgap renormalization and excitonic effects in a monolayer transition metal dichalcogenide semiconductor, (2014) (available at http://arxiv.org/abs/1404.2331).
122. A. Chernikov *et al.*, Non-Hydrogenic Exciton Rydberg Series in Monolayer WS2, *arXiv* , 6 (2014).
123. G. Wang *et al.*, Non-linear Optical Spectroscopy of Excited Exciton States for Efficient Valley Coherence Generation in WSe2 Monolayers, (2014) (available at http://arxiv.org/abs/1404.0056).
124. Z. Ye *et al.*, Probing Excitonic Dark States in Single-layer Tungsten Disulfide, (2014) (available at http://arxiv.org/abs/1403.5568).

125. B. Zhu, H. Zeng, J. Dai, Z. Gong, X. Cui, Anomalously Robust Valley Polarization and Valley Coherence in Bilayer WS2, (2014) (available at http://arxiv-web3.library.cornell.edu/abs/1403.6224?context=cond-mat).
126. A. R. Klots *et al.*, Probing excitonic states in ultraclean suspended two-dimensional semiconductors by photocurrent spectroscopy, , 12 (2014).
127. K. F. Mak, K. He, J. Shan, T. F. Heinz, Control of valley polarization in monolayer MoS2 by optical helicity., *Nature Nanotech* **7**, 494–8 (2012).
128. H. Zeng, J. Dai, W. Yao, D. Xiao, X. Cui, Valley polarization in MoS2 monolayers by optical pumping., *Nature Nanotech* **7**, 490–3 (2012).
129. T. Cao *et al.*, Valley-selective circular dichroism of monolayer molybdenum disulphide., *Nat. Commun.* **3**, 887 (2012).
130. A. M. Jones *et al.*, Optical generation of excitonic valley coherence in monolayer WSe2., *Nature Nanotech* **8**, 634–8 (2013).
131. W. J. Yu *et al.*, Highly efficient gate-tunable photocurrent generation in vertical heterostructures of layered materials., *Nature Nanotech* **8**, 952–8 (2013).
132. O. Lopez-Sanchez, D. Lembke, M. Kayci, A. Radenovic, A. Kis, Ultrasensitive photodetectors based on monolayer MoS2., *Nature Nanotech* **8**, 497–501 (2013).
133. C. Gong *et al.*, Band alignment of two-dimensional transition metal dichalcogenides: Application in tunnel field effect transistors, *Appl. Phys. Lett.* **103**, 053513 (2013).
134. H. Komsa, A. Krasheninnikov, Electronic structures and optical properties of realistic transition metal dichalcogenide heterostructures from first principles, *Phys. Rev. B* **33**, 1–7 (2013).
135. J. Kang, S. Tongay, J. Zhou, J. Li, J. Wu, Band offsets and heterostructures of two-dimensional semiconductors, *Appl. Phys. Lett.* **012111**, 22–25 (2013).
136. H. Terrones, F. López-Urías, M. Terrones, Novel hetero-layered materials with tunable direct band gaps by sandwiching different metal disulfides and diselenides., *Sci. Rep.* **3**, 1549 (2013).
137. N. Anderson, T. Lian, Ultrafast electron transfer at the molecule-semiconductor nanoparticle interface., *Annu. Rev. Phys. Chem.* **56**, 491–519 (2005).
138. J.-L. Brédas, J. E. Norton, J. Cornil, V. Coropceanu, Molecular understanding of organic solar cells: the challenges., *Acc. Chem. Res.* **42**, 1691–9 (2009).
139. A. W. Hains, Z. Liang, M. A. Woodhouse, B. A. Gregg, Molecular semiconductors in organic photovoltaic cells., *Chem. Rev.* **110**, 6689–735 (2010).
140. A. M. van der Zande *et al.*, Grains and grain boundaries in highly crystalline monolayer molybdenum disulphide., *Nature Mater.* **12**, 554–61 (2013).
141. Y. Zhang *et al.*, Controlled growth of high-quality monolayer WS2 layers on sapphire and imaging its grain boundary., *ACS Nano* **7**, 8963–71 (2013).
142. C. Lee *et al.*, Anomalous lattice vibrations of single-and few-layer MoS2, *ACS Nano* **4**, 2695–700 (2010).
143. A. Berkdemir *et al.*, Identification of individual and few layers of WS2 using Raman spectroscopy., *Sci. Rep.* **3**, 1755 (2013).
144. X. Luo *et al.*, Effects of lower symmetry and dimensionality on Raman spectra in two-dimensional WSe_{2}, *Phys. Rev. B* **88**, 195313 (2013).
145. H. Terrones *et al.*, New First Order Raman-active Modes in Few Layered Transition Metal Dichalcogenides., *Sci. Rep.* **4**, 4215 (2014).

146. K. F. Mak *et al.*, Measurement of the Optical Conductivity of Graphene, *Phys. Rev. Lett.* **101**, 196405 (2008).
147. H. Shi *et al.*, Exciton dynamics in suspended monolayer and few-layer MoS_2 2D crystals., *ACS Nano* **7**, 1072–80 (2013).